MICROCOPY RESOLUTION TEST CHART

The Pennsylvania State University

The Graduate School

Department of Physics

Computational Methods in
Nearfield Acoustic Holography (NAH)

A Thesis in

Physics

by

William Aldo Veronesi

Submitted in Partial Fulfillment
of the Requirements
for the Degree of

Doctor of Philosophy

May 1986

MAY 2 9 1986

A

© 1986 by William Aldo Veronesi

_____

William Aldo Veronesi

ABSTRACT

The continuous integrals and integral equations which
form the theory of Nearfield Acoustic Holography for planar
and odd-shaped source boundary surfaces are reviewed, and
the approximations and assumptions necessary to reduce these
equations to a set of finite and discrete operations
suitable for computation are developed. These equations
represent the solution of the Helmholtz equation with
specified boundary conditions by Green's function methods.

In analyzing the reduction, to discrete form, of the
propagation of planar holograms (a record of the radiated
field over a plane above the boundary plane), four new
methods for representing the Green's functions numerically
are developed. The relationship of two earlier Green's
function representation methods to these new forms is
established. The results of numerical testing of these six
representations are presented. These results demonstrate
the effectiveness of the new representations.

Two computational methods for reconstructing planar
source boundary fields from planar holograms are developed.
The first method is an approximation of the continuous
solution method which the convolution theorem of Fourier

Transforms provides. In its simplest form, this method has a high sensitivity to noise; it is shown how this problem is partially alleviated by the use of a high spatial frequency filter. Numerical test results indicate the effectiveness of this method for very short distances between hologram and source boundary, a condition often satisfied in experiment. The new methods for representing the Green's function, developed for propagating planar holograms, are shown to be inappropriate with this reconstruction technique.

As an alternative to this reconstuction method, a conjugate gradient descent method is developed based on the finite and discrete propagation method discussed. This technique does benefit from the new Green's function representations. Although, this reconstruction method requires more time than the first method presented, it is relatively insensitve to noise, and it extends the feasible reconstruction range, or distance between hologram and boundary.

The reduction to finite and discrete form, by a Finite Element technique, of the relationship between the Dirichlet and Neumann boundary conditions for an odd shaped surface is reviewed. To develop a unique relationship, assuming radiation conditions apply, a knowledge of the boundary surface's characteristic frequencies is essential, and a method for detecting these frequencies for an odd-shaped

boundary is presented. A comparison of the characteristic frequencies predicted by this method and those given by theory is presented for a spherical surface.

A technique for reconstructing the odd-shaped surface boundary conditions from a hologram of general two-dimensional shape is proposed. Results from a numerical study which support this technique are presented. Two cases are considered in this study: reconstruction of a spherical boundary from a planar hologram, and reconstruction of a spherical boundary from a concentric, spherical boundary.
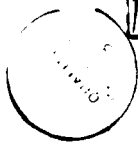
TABLE OF CONTENTS

LIST OF FIGURES

Chapter I.

INTRODUCTION TO NEARFIELD ACOUSTIC HOLOGRAPHY (NAH)

The works presented in this thesis are refinements and extensions to the comptational theory and practice of an exciting new imaging technique, conceived and developed at Penn State, called Nearfield Acoustic Holography.[1] The computational techniques of Nearfield Acoustic Holography are of particular interest to Physists, as they represent the development and application of classical field theory to large scale and geometrically complex problems. The solution of such problems has become feasible only recently as a result of the explosive development in computer facilities in the last two decades. Quite naturally, it is this author's hope that the methods explored and developed here will continue to find application in other areas of Physics, but for now this exposition must be limited to the specific problems encountered in Nearfield Acoustic Holography.

In the first section of this chapter, the basic concepts of holography, acoustic holography, and Nearfield Acoustic Holography are presented in turn. The major impetus for developing NAH was its potential as an experimental technique,[2] and defining the experimental

requirements of NAH serve to define the technique; they are presented in section B. The last section of this chapter describes some areas of application for Nearfield Acoustic Holography.

A. Definition of Nearfield Acoustic Holography

In general usage, holography refers to the recording and reproduction of three dimensional optical images,[3] and it was Gabor's work in optics which led to the concept of holography.[4] However, the basic idea of holography has since been applied to many other fields and regimes, such as seismic, ultrasonic, acoustic, and microwave fields[5]; hence, the term deserves more general definition.

A.1. Holography

For the purposes of this thesis, holography may be defined as a two step process which involves:

1) the recording, over a surface, of sufficient information about a three-dimensional linear wave field that, for practical purposes, the field can be uniquely specified;

2) the subsequent display of any region of the original

three-dimensional field based on the single

two-dimensional record of the field obtained in part 1.

The record of this surface field information is refered to

as the hologram.

The ideal surface, over which the information is

recorded, the hologram surface, divides space into a region

with sources and a region without sources. The ideal

hologram contains all information about the field over this

entire surface. Of course, in practice, these ideals are

neither possible nor necessary, and, hence, the requirement

to specify the field uniquely is relaxed to a practical

level. It is the particular application which imposes the

minimum information requirements. For example, when viewing

an optical hologram of a set of chess pieces, one would not

expect to resolve micron size chips in the surface of a

pawn, even though such information is, in theory, carried by

the original field. More specific requirements as they,

apply to NAH, are discussed in later chapters.

A.2. Acoustic Holography

In its most complete form, acoustic holography is

concerned with recording sufficient information about an

acoustic field that the acoustic pressure, three components

of particle velocity, and the three components of acoustic intensity can be determined at any point in the source-free region of the acoustic medium. NAH essentially meets this goal, although acoustic holography techniques of the past fell quite short of this goal in experimental theory and practice.

Previous forms of acoustic holography were largely based on the experimental methods of optical holography, and many required the use of lasers to redisplay the acoustic field.[6-7] These methods recorded either a component of particle velocity or the acoustic pressure over the hologram surface. Since these methods depended on optical inter- ference phenomena to redisplay the holographically recorded field component, subsequent observation of the reproduced field had to be accomplished by a phase- insensitive optical device. The resulting lack of phase information precluded the accurate determination of the remaining acoustic field variables, including the acoustic intensity vector field.

Another problem with previous acoustic holography techniques was resolution. This problem resulted from developing acoustic holography from experimental optical holography whose theory and success is, for the most part, based on the assumed existence of a purely propagating wave field. To insure the validity of this assumption, a hologram must be located in the farfield of any source.

Since they were based on experimental optical methods, earlier forms of acoustic holography were similarly restricted. This restriction is of little consequence in optical holography, although it imposes a wavelength resolution limit on the restored fields. However, if this resolution limit was physically inherent in all holography theory, acoustic holography would be useless for many problems in the audio range, where wavelengths are typically larger than their source. Fortunately this limitation is only a practical limitation occurring in most forms of optical holography,[8] and it may be viewed as artificial in acoustic holography.

A.3. Nearfield Acoustic Holography

Nearfield Acoustic Holography is an acoustic holography technique which comes much closer to the ideal holography described above. As its name declares, this method is carried out in the nearfield of radiating sources, and much of its merit comes from the ability of this technique to accurately process the non-propagating wave field information present in the nearfield. The resolution of this technique is not limited by the wavelength.

To understand how this increase in resolution is obtained, and why former techniques could not achieve this resolution, it is expedient to separate the possible finite linear acoustic wave solutions, in a semi-infinite space, into two catagories: propagating waves which transport energy out to infinity, and evanescent waves which are characterized by their rapid decay.[8] As discussed in chapter II and the original NAH paper[1] for planar boundaries, this separation is performed explicitly by the Fourier transform, and the resulting evanescent waves manifestly decay exponentially. Information about details of a source smaller than the characteristic acoustic wavelength can only be obtained by measuring the strength of these evanescent waves, restoring them to their original strength at the source, and finally superimposing these waves with the readily restored propagating waves.[1] It is not possible to restore these decayed waves, a process which requires selective enhancement, in the older forms of acoustic holography which rely on optical wave propagation to achieve a representative optical restoration of the acoustic field.

NAH does not require such a restoration technique due to its unique process for forming the hologram; the hologram is an electronically recorded sample, in digital form, of the field at a large number of points over the hologram

surface. With this type of hologram, numerical restoration of evanescent waves is relatively easy, and phase information is also readily obtained and manipulated numerically. The numerically restored fields are displayed with computer graphics.

At this point, an examination of the experimental hardware requirements of NAH will define the particulars of the overall technique.

B. Experimental requirements

The experimental implementation of NAH, such as the prototype system at Penn State,[9] consists of the successful integration of an extensive system of electronic equipment. An appreciation of the capabilities and limitations of such a system, gained by examining its experimental requirements, will help clarify the restrictions and approximations introduced in the remaining chapters, where computational NAH methods are developed largely with experimental systems in mind.

The experimental equipment may be divided into two subsystems: the transducers and the computer facilities. The requirements and tasks for each subsystem are outlined below.

B.1. Transducers

Inorder to avoid aliasing, the transducer subsystem in a typical NAH set-up must supply the computer subsystem, at a rate at least twice the maximum acoustic frequency,[10] with a digital representation of the acoustic pressure at a each of the points which define the hologram surface. This subsystem must also supply the exact location of the measurement points. Two methods have been employed to locate the hologram measurement points, and these two methods also have different equipment requirements and data conversion limitations.

A 16x16 square array of microphones forms the heart of the prototype transducer system at Penn State. Each microphone is fixed in position in the array, and the entire array is positioned by synchronous motors under computer control.[11] With this system it is easy to determine the relative and absolute positions of each microphone. Each microphone is equipped with a preamplifier, noise filter, and an analog switch.[12] As part of a relatively complex high speed switching system, the analog switch selectively connects the microphone to a shared signal line, and this signal is then routed to a high speed analog to digital converter.[13] The advantages of such a system are the

speed with which single frequency sources can be analyzed and, due to the nearly simultaneous sampling of the microphones achieved with the switching system, the possibility of analyzing relatively wideband sources.[13]

Some of the complexity and speed of a microphone array system can be traded off in the study of single frequency sources, or highly reproducible wideband sources, by using an articulated boom mounted microphone. Besides the loss in speed, the use of this type of system requires a more complex system for specifying the microphone location. On the positive side, with a single microphone, phase sensitive detection methods can be employed to reduce the single to noise ratio in single frequency studies.[14] Also, an articulated boom mounted microphone allows the specification hologram surfaces which are not flat, and this may be of great advantage in the study of odd-shaped sources as discussed in chapters V and VI. Boom mounted systems have been employed by a number of investigators.[15,16] In this type of system, the final output is either a near real-time digital representation of the microphone signal, which is collected and processed by the computer system or, for single frequency work with phase-sensitve detection, a digital representation of the phase (e.g.,relative to the source drive signal) and amplitude of the microphone signal.

B.2. Computer and Graphic output devices

The computer system in a NAH experiment serves to store, process, and display all collected and generated data, and it is easiest to review the system requirements by describing the Penn State system and the role its components play. The Penn State system is composed of a minicomputer with the following attached components: a peripheral port connection with the analog to digital system, hard disk and floppy disk storage devices, an array processor, a vector graphics display monitor, and a pen plotter. The role of each of these devices is seen by following the typical sequence of steps in a NAH experiment.

A digital sample of the signal at each microphone location, as a function of time, is collected by the computer from the analog to digital conversion system. Each of these time sequences is passed to the array processor where they are transformed into a frequency domain representation. An important step in this part of the process is calibration. In a multiple microphone system, calibration information is stored for each microphone providing its relative phase and amplitude response. The measured response of each microphone is normalized with this calibration data.[17] Taken at a single frequency, the set of complex numbers, representing the acoustic pressure

amplitude and phase at each microphone, defines an acoustic hologram. Any number of these single frequency acoustic holograms are stored on magnetic disks. From one of these holograms, a digital representation of the original acoustic field at any number of spatial locations is generated by numerical methods (these methods being the point of this thesis). Since an enormous amount of data is normally generated, it is usually displayed on one of the graphic output devices. This graphic output typically takes the form of a hidden-line plot of an acoustic variable versus two spatial dimensions as in the example of figure 1.1, or it may take the form of a vector intensity map as in the example of figure 1.2. The time dependence of the acoustic parameters be displayed with motion pictures on the display monitor.[18] This type of display is particularly instructive in the study of source boundaries, as the source structure's complicated dynamic response may be veiwed in slow-motion.

C. Applications

The direct applications of NAH are numerous due to the wealth of information about an acoustic field it can provide from a relatively small amount of input data. There is much interest in acoustic intensity measurement today, and the holographic method can quickly provide a detailed mapping of
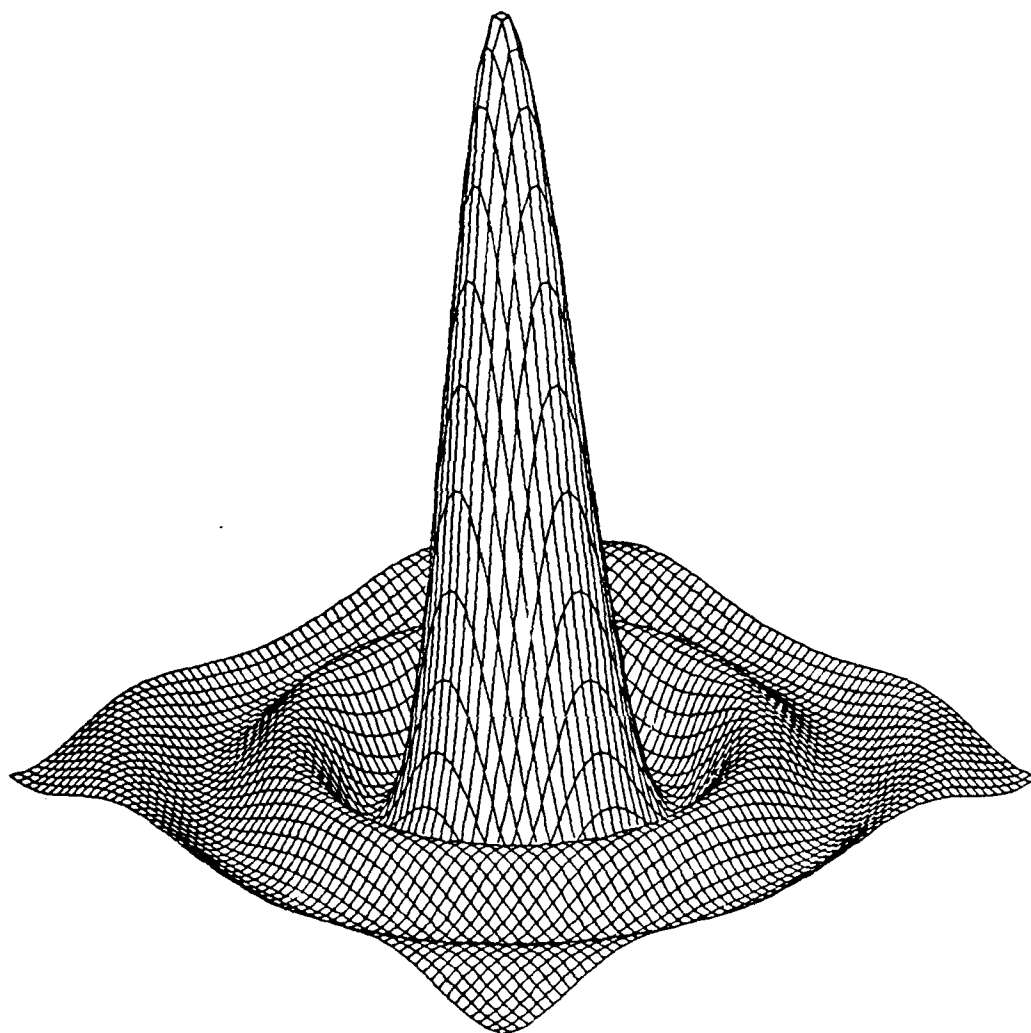
Figure 1.1   In NAH, the acoustic field is viewed with
computer graphics.   As an example, this hidden-line plot
displays the pressure amplitude at the boundary plane as
produced by a piston set in an otherwise rigid boundary.
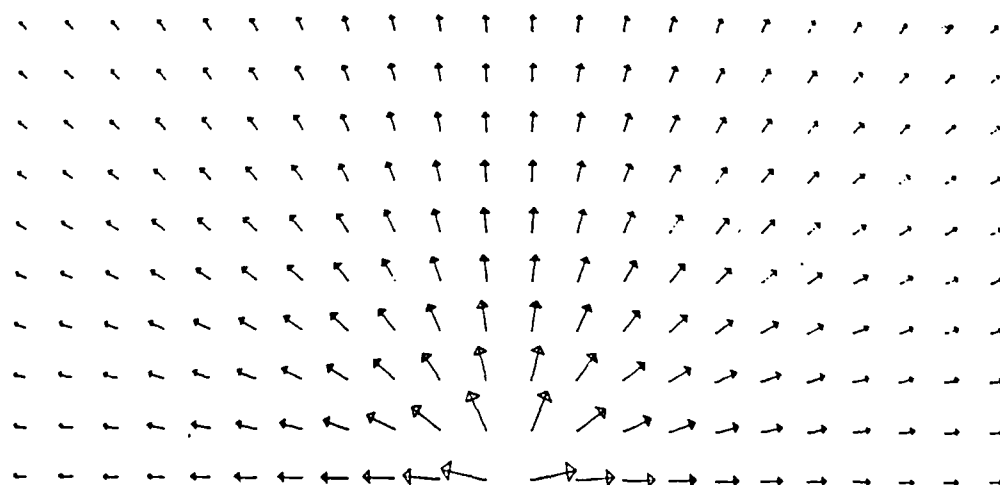
Figure 1.2 NAH techniques were used to generate this theoretical vector intensity map for a point source.

this energy flow as can no other technique, such as the "two microphone technique",[19] provide in a reasonable time. An advantage which NAH has over dual or multiple[20] microphone texhniques is that, the intensity determined at a specific point by the holographic process is dependent on a large number of microphone measurements (typically 4096 with the prototype system at Penn State), whereas the intensity determined with other techniques is dependent only a few measurements. This integration of a large number of measurements can be expected to improve the signal to noise ratio, relative to other field mapping techniques.
Its speed and accuracy make NAH ideally suited for the study of sound production equipment, and prototype systems for studying musical instruments and loudspeakers are already in use.[15,21]

NAH also provides a fast non-contact method for determining the normal component of surface velocity of a vibrating source. A particularlly interesting application of this capability is in the proposed experimental observation of an acoustic analogue of 2-D Anderson Localization,[22] where the technique will be used to observe

the vibrational modes of a randomly nonuniform elastic sheet.[23] From the holographically determined normal component of velocity, the flow of energy within a plate may also be studied.[24]

Any area where quick and accurate determination of the acoustic field above a plane or other level surface in a separable coordinate system will benefit from the application of NAH in its present state of development.[9] With the experimental implementation of the extensions of NAH to odd-shaped sources, and the refinement of the computational methods of NAH presented in this thesis, the list of practical applications should grow.

Chapter II.

FUNDAMENTAL EQUATIONS OF NEARFIELD ACOUSTIC HOLOGRAPHY

The numerical methods of Nearfield Acoustic Holography presented in the following chapters are approximations to a set of continuous integrals and integral equations relating the acoustic field to appropriate boundary conditions. It is the purpose of this chapter to introduce these equations and to clarify the objectives of this work in terms of these equations.

The first section of this chapter very briefly reviews: the formulation of Newton's Law for continuous media, Euler's equation, which provides a direct link between the acoustic pressure and particle velocity fields; and the linear approximation of the general equations of non-viscous hydrodynamics, which yields the Wave Equation and, for single frequencies, the Helmholtz equation.

The continuous solution of the Helmholtz Equation with boundary conditions is accomplished by a Green's function technique. The basic ideas behind these techniques are presented in section B. The Helmholtz Integrals and Rayleigh's Integrals are reviewed in this section, as they follow from the solution of the Helmholtz Equation by Green's function methods.

The last section of this chapter introduces the terminology used to define the specific problems in Nearfield Acoustic Holography considered in this work.

A. The Acoustic Equations

The acoustic field variables of pressure and three components of particle velocity are of 'ief interest in Nearfield Acoustic Holography, and techniques are developed for determining these fields as generated from single frequency sources. Note that the term "source" refers to a boundary condition in this thesis, since very few problems in Acoustics involve any true volume sources, and no volume sources are considered here. Also, considering only single frequency sources is not restrictive as the extension of these techniques to multiple frequencies is readily accomplished by superposition of a number of single frequency solution fields.

A.1 Euler's Equation

Newton's Second Law in a form suitable for use in problems of continuous media provides the direct link between the Acoustic pressure field and the three components of the particle velocity field. By applying Newton's Second

Law to an infinitesimal volume of inviscid fluid with
density ρ acted upon only by the pressure field p in which
it is immersed, it is straightforward to show that the
acceleration of this volume is given as

$$\vec{a}(\vec{r},t) = \frac{d\vec{v}}{dt}(\vec{r},t) = -\frac{1}{\rho}\nabla p(\vec{r},t) \qquad (2.1).$$

This is Euler's Equation.[25]

All solutions to problems in this work are formulated
in terms of single temporal frequency components. A general
explicit function of time, f(t), is transformed to one
explicitly of frequency, $F(\omega)$, by the Fourier transform
defined by

$$F(w) = \int_{-\infty}^{+\infty} f(t)e^{i\omega t}dt \qquad (2.2),$$

and its inverse

$$f(t) = \frac{1}{2\pi}\int_{-\infty}^{+\infty} F(\omega)e^{-i\omega t}d\omega \qquad (2.3).$$

By expressing the velocity and pressure in equation (2.1) in
terms of their frequency domain representations, $\vec{v}(\vec{r},\omega)$ and
$p(\vec{r},\omega)$, with integrals of the form of equation (2.3),
Euler's Equation, equation (2.1), can be written as

$$\vec{v}(\vec{r},\omega) = -\frac{i}{\omega\rho}\nabla p(\vec{r},\omega) \qquad (2.4).$$

This equation allows one to calculate the particle velocity
field once the acustic pressure field $p(\vec{r},\omega)$ has been found.

A.2 The Wave and the Helmholtz Equations

The solution of the general equations of inviscid hydrodynamics reduces to the solution of the Wave Equation

$$\nabla^2 \Psi(\vec{r}, t) = \frac{1}{c^2} \frac{\partial^2}{\partial t^2} \Psi(\vec{r}, t) \qquad (2.5)$$

in a linear approximation with isentropic conditions.[25] The constant c is the propagation speed and is defined as the partial derivative of the pressure with respect to density at constant entropy. Both the pressure and velocity fields must satisfy this equation.

By expressing the field $\Psi(\vec{r}, t)$ with its temporal Fourier Transform

$$\Psi(\vec{r}, t) = \frac{1}{2\pi} \int_{-\infty}^{+\infty} \psi(\vec{r}, \omega) e^{-i\omega t} d\omega \qquad (2.6),$$

the wave equation reduces to the Helmholtz Equation,

$$\nabla^2 \psi(\vec{r}, \omega) + \left[\frac{\omega}{c}\right]^2 \psi(\vec{r}, \omega) = 0 \qquad (2.7).$$

For the remainder of this work, only solutions at a single frequency ω will be considered; therefore, for convenience, the dependence of ψ on ω is suppressed, and the character-istic wavenumber k replaces the equivalent constant ω/c. This simplifies the appearance of equation (2.7) to

$$\nabla^2 \psi(\vec{r}) + k^2 \psi(\vec{r}) = 0 \qquad (2.8).$$

The problems of acoustic holography either involve finding solutions to the Helmholtz Equation, equation (2.8), which satisfy a particular set of boundary conditions, or they involve finding a set of boundary conditions which produce a field ψ which satisfies equation (2.8) and is equivalent, over a surface above the boundary surface, to a measured field.

B. Green's Functions

The solution techniques presented in chapters III-VI are numerical approximations to Green's function techniques for solving differential equations.[26] The application of these methods to the solution of the Helmholtz Equation with boundary conditions is reviewed in this section.

B.1 Green's Theorem and the Green's Function

The Green's function method for solving the Helmholtz Equation with boundary conditions involves finding a solution to the inhomogeneous form of equation (2.8),

$$\nabla^2 G(\vec{r}_0 - \vec{r}) + k^2 G(\vec{r}_0 - \vec{r}) = -\delta(\vec{r}_0 - \vec{r}) \qquad (2.9),$$

where the right-hand side term is the delta function, and

the solution G is the Green's function for a specified boundary condition. The utility of a solution to equation (2.9) for solving equation (2.8) is clear if Green's theorem is applied to the functions G and ψ. Green's theorem guarauntees that[27]

$$\int [G(\vec{r}_0 - \vec{r}) \nabla^2 \psi(\vec{r}) - \psi(\vec{r}) \nabla^2 G(\vec{r}_0 - \vec{r})] dV =$$
$$- \oint_S [G(\vec{r}_0 - \vec{r}) \nabla \psi(\vec{r}) - \psi(\vec{r}) \nabla G(\vec{r}_0 - \vec{r})] \cdot \vec{n} da \qquad (2.10),$$

where the right-hand side integration surface S encloses the left-hand side integration volume, and the surface normal $\vec{n}$ points *into* the volume. For the moment, it will be useful to consider ψ to be a solution of the inhomogeneous Helmholtz equation given by

$$\nabla^2 \psi(\vec{r}) + k^2 \psi(\vec{r}) = -f(\vec{r}) \qquad (2.11).$$

With equation (2.11) and (2.9), the left-hand side of equation (2.10) reduces to

$$\int -[k^2 G(\vec{r}_0 - \vec{r}) + \nabla^2 G(\vec{r}_0 - \vec{r})] \psi(\vec{r}) dV - \int G(\vec{r}_0 - \vec{r}) f(\vec{r}) dV =$$
$$\int \delta(\vec{r}_0 - \vec{r}) \psi(\vec{r}) dV - \int G(\vec{r}_0 - \vec{r}) f(\vec{r}) dV = \psi(\vec{r}_0) - \int G(\vec{r}_0 - \vec{r}) f(\vec{r}) dV$$
$$(2.12),$$

so that the entire equation simplifies to

$$\psi(\vec{r}_0) = \int G(\vec{r}_0 - \vec{r}) f(\vec{r}) dV + \oint_S [\psi(\vec{r}) \nabla G(\vec{r}_0 - \vec{r}) - \nabla \psi(\vec{r}) G(\vec{r}_0 - \vec{r})] \cdot \vec{n} da$$
$$(2.13).$$

Equation (2.13) gives an explicit solution to equation

(2.11) inside the volume bounded by the integration surface S provided ψ and $\nabla\psi \circ \vec{n}$ are known on this boundary, and the forcing function $-f(\vec{r})$ is known throughout the volume.

Only numerical solutions to the homogeneous Helmholtz Equation are considered in this work; however, the inhomogeneous term has been introduced to motivate the existence of a solution to equation (2.9) which, along with its normal derivative, vanishes over the integration surface of equation (2.13) when this surface is very far from any volume source region. It can be shown that there are two such solutions possible, and they are[28]

$$G(\vec{r}_0 - \vec{r}) = \frac{e^{+ikR}}{4\pi R} \text{ or } \frac{e^{-ikR}}{4\pi R} \tag{2.14},$$

where $R = |\vec{r}_0 - \vec{r}|$. By requiring the Green's function to adhere to the principle of causality with the specified time dependence of all solutions given in equation (2.6), the second possibility for the right-hand side of equation (2.14) is ruled out. The correct form for the Green's function for an unbounded region, the free-space Green's function, is [25]

$$G_f(\vec{r}_0 - \vec{r}) = \frac{e^{+ikR}}{4\pi R} \tag{2.15},$$

and ψ, with the restriction to a radiating form at large distances, has the solution

$$\psi(\vec{r}_0) = \int G_f(\vec{r}_0 - \vec{r}) f(\vec{r}) dV \qquad (2.16).$$

It is shown in the next section how the free-space Green's function is of great utility in bounded acoustic problems without volume sources.

B.2. The Helmholtz Integrals

The relationship stated in equation (2.13) holds for any function G which satisfies equation (2.9), although it is most useful when the function G also satisfies either homogeneous Dirichlet or Neumann boundary conditions. In practice, it is impossible to obtain a simple closed form function satisfying both equation (2.9) and a homogeneous boundary condition for anything more than the most simple boundary shape. However, boundary value problems for arbitrarily shaped surfaces can be solved with a system of integral equations formed from equation (2.13) and the free-space Green's function.

In the absence of volume sources, equation (2.13) with the free-space Green's function becomes

$$\psi(\vec{r}_0) = \oint_S [\psi(\vec{r}) \nabla G_f(\vec{r}_0 - \vec{r}) - \nabla \psi(\vec{r}) G_f(\vec{r}_0 - \vec{r})] \cdot \vec{n} da$$

$$= \oint_S [\psi_D(\vec{r}) \frac{\partial G}{\partial n}_f(\vec{r}_0 - \vec{r}) - i\psi_N(\vec{r}) G_f(\vec{r}_0 - \vec{r})] da \quad (2.17),$$

where ψ_D represents the Dirichlet boundary condition, where

$\frac{\partial}{\partial n} = \vec{n} \circ \nabla$, and where the Neumann boundary condition Ψ_N has

been defined as $-i\frac{\partial \Psi}{\partial n}$ in anticipation of the identification

of the pressure field p and the related velocity field

[equation (2.4)] as useful boundary conditions in

experimental acoustics problems. Equation (2.17) is known

as the Helmholtz Integral.[29]

This equation alone is inadequate for solving boundary

value problems, as it requires the specification of both the

Dirichlet and Neumann boundary conditions. This problem is

readily resolved with the help of two more integral

equations which relate the two boundary conditions, and

which can be derived from Green's Theorem with the

Free-space Green's function. However, before reviewing

these equations, it is best to introduce the terminology

used throughout the remainder of this work to distinguish

the region of the integration volume in equation (2.12) from

the rest of space.

Implicit in equation (2.17) is the fact that the point

$\vec{r}_0$ is within the integration volume of equation (2.12).

Only radiating problems are considered here, and for all the

boundary geometries considered, a portion of the boundary

surface is off at infinity. The portion of at infinity is

an abstraction, of course, and so the main boundary surface

of interest divides space into a generally *finite* bounded

interior region and an *infinite exterior* region. The
integration volume in equation (2.12) is taken as this
exterior region for *radiation* problems. To distinguish
between points located in the two regions or on the
separating surface, points in the interior are subscripted
with I's, points on the surface are subcripted with s's, and
points in the exterior field are subscripted with f's.

With this terminology established, it is possible to
introduce the Interior Helmholtz Integral Equation. If the
point $\vec{r}_0$ is an interior point $\vec{r}_I$, and hence, not included in
the integration volume of equation (2.12), the left-hand
side of equation (2.10) is zero in the absence of volume
sources. Instead of arriving at equation (2.17) with the
introduction of the free-space Green's function in the
remaining right-hand side of equation (2.10), the Interior
Helmholtz Integral Equation is obtained:

$$0 = \oint_S [\Psi_D(\vec{r}_s)\frac{\partial G}{\partial n}f(\vec{r}_I-\vec{r}_s) - i\Psi_N(\vec{r}_s)G_f(\vec{r}_I-\vec{r}_s)]da$$

$$(2.18).$$

This equation relates the Dirichlet and Neumann boundary
conditions.

By allowing an exterior field point $\vec{r}_f$ or an interior
point $\vec{r}_I$ to approach the boundary surface it is possible to
obtain another integral relationship between the two
boundary conditions from the resulting limit form of

equation (2.17) or (2.18) respectively. Provided the normal direction is defined at a surface point $\vec{r}_s$, and ψ is reasonably well behaved, it is readily shown that, in the limit, these equations both reduce to

$$\psi_D(\vec{r}'_s) = 2\oint\limits_{S-\epsilon^2} \psi_D(\vec{r}_s)\frac{\partial G}{\partial n}f(\vec{r}'_s-\vec{r}_s)da - 2i\oint\limits_{S} \psi_N(\vec{r}_s)G_f(\vec{r}'_s-\vec{r}_s)da$$

$$(2.19),$$

where the first integral excludes an infinitesimal area ϵ^2 around the surface point $\vec{r}'_s$. This integral equation, relating the boundary conditions, is known as the Surface Helmholtz Integral Equation. The use of equation (2.18) and (2.19) together to uniquely relate the Dirichlet and Neumann boundary conditions for a general surface is discussed in Schenck's paper[30] and in chapter V.

B.3 Rayleigh's Integrals and Fourier Transforms

For the special case of an infinite half-space enclosed by a plane boundary topped with a hemisphere of infinite radius, the solution of the Helmholtz Equation is much easier to calculate. The symmetry of an infinite plane makes it possible to construct Green's functions which satisfy equation (2.9) in the half-space above the plane, and which also satisfy either the homogeneous Neumann or

Dirichlet boundary conditions on the plane. These Green's functions can be used to generate radiating solutions to the Helmholtz equation when all sources are below the plane, since such solutions must diminish to the point where integration over the hemisphere can be neglected. On a plane boundary in a Cartesian coordinate system where $\Psi_D(x,y)$ or $\Psi_N(x,y)$ on the plane $z = 0$ is the boundary condition, and where there are no volume sources, the solution to the Helmholz Equation, as given by equation (2.13), reduces to a two-dimensional convolution integral:

$$\Psi(x,y,z) = \int_{-\infty}^{+\infty}\int_{-\infty}^{+\infty} \Psi_{D,N}(x',y') G_{D,N}(x-x',y-y',z)dx'dy'$$

$$(2.20).$$

The Green functions, G_D and G_N, are known:[1]

$$G_D(x,y,z) = \frac{z(1-ikR)e^{ikR}}{2\pi R^3} \qquad (2.21)$$

and

$$G_N(x,y,z) = \frac{-ie^{ikR}}{2\pi R} \qquad (2.22)$$

where $R^2 = x^2+y^2+z^2$. Historically, equation (2.20) for the two boundary conditions (D or N) are referred to as the first and second Rayleigh integrals.[31]

For numerical processing, it is well known that a convolution is more readily evaluated by using Fourier Transforms.[32] $\mathcal{F}$ will denote the continuous, infinite

two-dimensional Fourier transform of a function $f(x,y)$ as defined by:

$$\hat{F}(k_x,k_y) = \mathcal{F}[f(x,y)]$$

$$= \int_{-\infty}^{+\infty}\int_{-\infty}^{+\infty} f(x',y')e^{-i(k_x x'+k_y y')}\,dx'dy' \quad (2.23),$$

and the inverse operation will be indicated as $\mathcal{F}^{-1}$. The domain of (k_x,k_y) will be referred to as k-space, while that of (x,y) will be referred to as real-space.

Applying the convolution theorem[33] to equation (2.20) yields:

$$\Psi(x,y,z) = \mathcal{F}^{-1}[\hat{\Psi}_{D,N}(k_x,k_y)\hat{G}_{D,N}(k_x,k_y,z)] \quad (2.24).$$

The Fourier transforms of the Green's functions G_D and G_N in equations (2.21) and (2.22) may be found analytically:[34]

$$\hat{G}_D(k_x,k_y,z) = \begin{cases} \exp\left[iz\sqrt{k^2-k_x^2-k_y^2}\right] & \text{when } k_x^2+k_y^2 \leq k^2 \\ \exp\left[-z\sqrt{k_x^2+k_y^2-k^2}\right] & \text{when } k_x^2+k_y^2 > k^2 \end{cases} \quad (2.25)$$

$$\hat{G}_N(k_x,k_y,z) = \begin{cases} \dfrac{\exp\left[iz\sqrt{k^2-k_x^2-k_y^2}\right]}{\sqrt{k^2-k_x^2-k_y^2}} & \text{when } k_x^2+k_y^2 \leq k^2 \\ \dfrac{-i\exp\left[-z\sqrt{k_x^2+k_y^2-k^2}\right]}{\sqrt{k_x^2+k_y^2-k^2}} & \text{when } k_x^2+k_y^2 > k^2 \end{cases} \quad (2.26).$$

The circle $k_x^2+k_y^2=k^2$ is referred to as the radiation circle.

For points (k_x,k_y) inside the radiation circle, $\hat{G}_{D,N}$

represents the z-direction phase change of propagating plane waves, while for points (k_x, k_y) outside the radiation circle $\hat{G}_{D,N}$ represents the rapid exponential decay of evanescent waves. By defining a complex function, $k_z(k_x, k_y) = \sqrt{k^2 - k_x^2 - k_y^2}$, the transformed Green functions may be written in the condensed forms $\hat{G}_D = \exp(ik_z z)$ and $\hat{G}_N = \exp(ik_z z)/k_z$.

For holography or inverse scattering problems, the use of equation (2.24) is essential, because in this way the convolution integral (2.20) may be quickly inverted; that is, the field $\Psi(x, y, z_H)$ may be deconvolved to yield the source field $\Psi_{D,N}(x, y)$. Assuming that $\Psi(x, y, z_H)$ is known, we have, from equation (2.24),

$$\Psi_{D,N}(x,y) = \mathcal{F}^{-1}[\hat{\Psi}(k_X, k_Y, z_H)\hat{G}_{D,N}^{-1}(k_X, k_Y, z)] \quad (2.27),$$

where $\hat{G}_{D,N}^{-1}(k_X, k_Y, z_H)$, the reciprocal of the formula in equations (2.25) or (2.26), provides the reconstruction of both propagating and evanescent waves. Once the source field $\Psi_{D,N}$ has been determined, all other properties of the field may be calculated.[9] It should be noted that as far as the processing theory is concerned, $\Psi_{D,N}(x,y)$ need not correspond to a physical source surface. In fact equation (2.20) may be generalized to apply to the field and its derivative between any two planes, one at z and the other at

z_0 lying between zero (the actual source) and z. The more general equations are:

$$\Psi(x,y,z) = \int_{-\infty}^{+\infty}\int_{-\infty}^{+\infty} \Psi(x',y',z_0)G_D(x-x',y-y',z-z_0)dx'dy'$$

(2.28),

and

$$\Psi(x,y,z) = \int_{-\infty}^{+\infty}\int_{-\infty}^{+\infty} -i\frac{\partial\Psi}{\partial z}(x',y',z_0)G_N(x-x',y-y',z-z_0)dx'dy'$$

(2.29).

Equations (2.28) and (2.29) are the basis of planar acoustic holography.

C. Definition of the problems

The first two sections of this chapter review the fundamental equations of Nearfield Acoustic Holography. This section defines the problems of Nearfield Acoustic Holography treated in the remaining chapters.

C.1. Planar Holography

The evaluation or inversion of two equations (2.28) and (2.29) represent four operations referred to as:

    a) propagation of a wavefront, where $\Psi(x,y,z)$ is determined from Ψ at z_0

b) transformation and propagation, where $\Psi(x,y,z)$ is
   determined from $\partial\Psi/\partial z$ at z_0

c) reconstruction, where $\Psi(x,y,z_0)$ is determined
   from $\Psi(x,y,z)$

d) reconstruction and inverse transformation, where
   $\frac{\partial\Psi}{\partial z}(x,y,z_0)$ is determined from $\Psi(x,y,z)$.

Since by definition $z>z_0>0$ and zero is the actual source

plane, the reconstruction processes may be referred to

as the inverse propagation of a wavefront back toward the

source. When $z = z_0$ in processes b and d, the process will

be referred to as a transformation.

In chapter III, the approximations and assumptions

necessary to reduce the infinite and continuous convolution

integrals encountered in problems a and b to a finite and

discrete form, suitable for high speed numerical processing,

are illuminated theoretically and tested numerically. To

evaluate the convolution integrals two assumptions are made:

first, the boundary field may be replaced with a patch-wise

constant field for reasonably small patches; and second, the

field is negligible outside of a finite region. With these

two assumptions, the problem reduces to one of representing

the Green's functions G_D and G_N. Six methods of sampling or representing the Green's functions are developed, and the effectiveness of these methods are compared theoretically and numerically.

In chapter IV, a numerical inversion method, based on equation (2.27), to solve problems c and d is examined theoretically. The suitability of the reciprocals of the six Green's function sampling forms developed in chapter III for use as inverse propagators with this method is examined numerically. An iterative deconvolution method is also presented in chapter IV.

C.2 Non-planar Holography

In the most general holographic experiment, neither the source boundary nor the surface over which field data is gathered is flat in cartesian coordinates or any other separable coordinate system. Representing these surfaces themselves is an important problem which is not encountered in planar holography. Chapter V presents suitable methods for modelling odd-shaped surfaces numerically and for relating the Dirichlet and Neumann boundary conditions. Numerical approximation of the three Helmholtz Integrals form the basis of chapter V and VI.

Chapter VI presents a computational method for determing the boundary surface conditions of an odd-shaped radiator from field measurements above the surface. The results of simulated holograpy experiments which test this method are also presented. The exact nature of these simulations is fully explained in chapter VI.

Chapter III.

THE PROPAGATION OF PLANAR HOLOGRAMS

In Nearfield Acoustic Holography, a set of values,
either experimentally measured or theoretically generated,
of a field ψ or its normal derivative, at a number of points
evenly distributed over a planar, rectangular grid is
referred to as a planar hologram. As representations of
infinite plane boundary conditions, these holograms, with
the aid of Rayleigh's Integrals, equations (2.28) and
(2.29), can be used to calculate a representation of the
entire three-dimensional field above the hologram plane. In
this chapter, a computational method for determining this
3-D field is developed, and test results of this method are
reported.

A. Reduction to finite and discrete operations

The infinite, continuous integral operations reviewed
in the last chapter must be reduced to finite and discrete
approximations to allow processing with current digital
computing equipment. The validity of a solution obtained
with such an approximation depends directly on the validity
of the assumptions and method used to reduce the infinite,

continuous relationships. It is the purpose of this section to clearly delineate the methods and assumptions used to reduce the propagation of planar holograms to finite and discrete operations.

A.1 Rayleigh's Integrals

The limits required to numerically evaluate the formulas in equation (2.28) or (2.29) with finite, discrete operations may be imposed by restrictions on experimental data acquisition or restrictions on computation time and capacity. In either case several basic assumptions must be made. The first is that the sources of the wavefield ψ are such that the boundary data $\psi_D(x,y)$ or $\psi_N(x,y)$ is negligible outside of some finite domain in real space. Denoting this domain by $-L/2 < x < L/2$ and $-L/2 < y < L/2$, equation (2.20) [likewise (2.28) and (2.29)] becomes:

$$\psi(x,y,z) \approx \int_{-\frac{L}{2}}^{+\frac{L}{2}} \int_{-\frac{L}{2}}^{+\frac{L}{2}} \psi_{D,N}(x',y') G_{D,N}(x-x',y-y',z) \, dx' dy' \quad (3.1).$$

The second assumption is that the wavefield ψ can be represented sufficiently well with a discrete, as well as finite, set of numbers. This set of numbers may be a data set from experimental measurements at lattice points in real-space or coefficients for a superposition of basis

functions. For this model, the simplest case is chosen in which it is assumed that the wavefield Ψ is not significantly altered if the boundary field $\Psi_{D,N}$ is replaced with a piecewise constant field. That is, the L x L real space domain is divided into N^2 patches of size (L/N) x (L/N), labeled with integers $l,m = 0,1,\ldots,N-1$, and the discrete set of data $\Psi_{D,N}(l,m)$ is assumed to be the average of the actual boundary field over the patch. The field radiated from the piecewise constant boundary field can be assumed to represent Ψ if N is sufficiently large.

For the piecewise constant boundary field, equation (3.1) becomes:

$$\Psi(x,y,z)=\sum_{l=0}^{N-1}\ \sum_{m=0}^{N-1}\Psi_{D,N}(l,m)\int_{x_l-\Delta/2}^{x_l+\Delta/2}\int_{y_m-\Delta/2}^{y_m+\Delta/2}G_{D,N}(x-x',y-y',z)dx'dy'$$

$$(3.2),$$

with

$$x_l= (l+1/2-N/2)\Delta \tag{3.3}$$

$$y_m= (m+1/2-N/2)\Delta \tag{3.4}$$

where $\Delta = L/N$.

Finally it is assumed that it is sufficient to examine the field Ψ in any plane z at discrete points (x_p,y_q) defined as in equations (3.3) and (3.4) for integers p, q = $0,\ldots N - 1$. By defining variables $u = x_p-x'$, $v = y_q-y'$, equation (3.2) becomes:

$$\int_{x_l-\Delta/2}^{x_l+\Delta/2}\int_{Y_m-\Delta/2}^{Y_m+\Delta/2} G_{D,N}(x_p-x',Y_q-y',z)dx'dy'$$

$$= \int_{(p-l-1/2)\Delta}^{(p-l+1/2)\Delta}\int_{(q-m-1/2)\Delta}^{(q-m+1/2)\Delta} G_{D,N}(u,v,z)dudv$$

$$= \tilde{G}_{D,N}(p-l,q-m,z) \tag{3.5},$$

with integers l, m, p, q = 0,...N-1. Letting $\Psi(p,q,z)$ $\Psi(x_p,Y_q,z)$, the expression for the radiated field becomes:

$$\Psi(p,q,z) = \sum_{l=0}^{N-1}\sum_{m=0}^{N-1}\Psi_{D,N}(l,m)\tilde{G}_{D,N}(p-l,q-m,z) \tag{3.6},$$

which is the discrete, finite version of the Rayleigh integral (2.20).

A.2 Discrete convolution

As with the infinite, continuous convolution, the finite, discrete convolution in equation (3.6) is most readily evaluated using the convolution theorem and Fourier transforms (in particular, the Fast Fourier Transform algorithm, FFT). Although discussions of the discrete, finite convolution theorem may be found in textbooks on signal processing, most treatments assume that both arrays to be convolved are either periodic or zero for indices outside the range 0,...N-1. However, in the discrete convolution in equation (3.6) one of the arrays, $G_{D,N}(p-l,q-m,z)$ [defined in equation (3.5)] may be evaluated

for all integers l, m, p, q, because the Green's function $G_{D,N}(u,v,z)$ is known analytically over an infinite domain. Because of this exceptional feature, the discrete convolution theorem must be rederived; the details of this procedure are presented in Appendix A. Briefly, the results are as follows:

The sequence $\Psi_{D,N}(l,m)$ which is defined only for integers (l,m) in $(0,N-1)$ must be extended over a $(2N)$ x $(2N)$ domain by adding zeroes This new sequence is defined with:

$$\Psi'_{D,N}(l,m) = \begin{cases} \Psi_{D,N}(l,m) & \text{if } 0 \leq l < N \text{ and } 0 \leq m < N \\ 0 & \text{otherwise} \end{cases} \qquad (3.7).$$

The discrete Fourier transform DFT(f) of an array $f(l,m)$ with (l,m) in $(0,2N-1)$ is defined (for $\mu,\nu=0,1,\ldots 2N-1$) as:

$$DFT(f)_{\mu\nu} = \sum_{l=0}^{2N-1} \sum_{m=0}^{2N-1} f(l,m) \, e^{-\frac{i\pi}{N}(l\mu+m\nu)} \qquad (3.8),$$

and the inverse is indicated as

$$IDFT(F)_{lm} = \frac{1}{4N^2} \sum_{\mu=0}^{2N-1} \sum_{\nu=0}^{2N-1} F(\mu,\nu) \, e^{+\frac{i\pi}{N}(l\mu+m\nu)} \qquad (3.9).$$

As shown in Appendix A the finite discrete convolution (3.6) can be calculated with:

$$\Psi(p,q,z) = IDFT\{DFT[\Psi'_{D,N}] \, g_{D,N}(z)\} \qquad (3.10)$$

where

$$g_{D,N}(z)_{\mu\nu} = DFT[\bar{G}'_{D,N}(z)]_{\mu\nu} \qquad (3.11)$$

with

$$
\bar{G}'_{D,N}(l,m,z) = \begin{cases} \bar{G}_{D,N}(l,m,z) & \text{if } 0 \leq l < N \text{ and } 0 \leq m < N \\ \bar{G}_{D,N}(l-2N,m,z) & \text{if } N \leq l < 2N \text{ and } 0 \leq m < N \\ \bar{G}_{D,N}(l,m-2N,z) & \text{if } 0 \leq l < N \text{ and } N \leq m < 2N \\ \bar{G}_{D,N}(l-2N,m-2N,z) & \text{if } N \leq l < 2N \text{ and } N \leq m < 2N \end{cases} \quad (3.12).
$$

A.3. The Green's Functions

Equations (3.10) and (3.11) form the computational basis for wavefront propagation in which $\Psi(p,q,z)$ is determined in any plane $z>0$ given the data $\Psi_{D,N}(l,m)$, (l,m) = 0,...N-1. The data manipulation simply involves adding zeroes to the data sets to form an extended (2N) x (2N) domain, performing a two-dimensional DFT on the extended data set, multiplying by a "propagator" $g_{D,N}(z)$, and then performing an IDFT. The computational difficulty lies in evaluating the propagator array $g_{D,N}(z)_{\mu\nu}$ which must be accomplished for each value of z and k (if the radiation involves different wavelengths λ). If equation (3.10) is used, then it is necessary to evaluate the integral in equation (3.5) which defines $\bar{G}_{D,N}$. Since the integration cannot be performed analytically, it must be-evaluated with some approximation. Two easy ways of doing this are:

1) Replace $G_{D,N}(u,v,z)$ in the integral in equation (3.5)

    by its value at the center of the integration patch;

    i.e., $G_{D,N}(u,v,z) \approx G_{D,N}[(p-1)\Delta,(q-m)\Delta]$. The resulting

    propagator $g_{D,N}^{(1)}(5)_{\mu\nu}$ is as defined by equations (3.11)

    and (3.12) with $\bar{G}_{D,N}$ replaced with:

    $$\bar{G}_{D,N}^{(1)}(r,s,z) = (L/N)^2 G_{D,N}(r\Delta,s\Delta,z) \qquad (3.13),$$

    where $r,s = -(N-1),\ldots 0,\ldots N.$ is the discrete

    transform of the analytic Green's function sampled at

    discrete points in real-space. The Green's function

    $G_{D,N}(r\Delta,s\Delta,z)$ is singular where $r = s = z = 0$, so when

    $r = s = 0$ and z is less than one tenth of a wavelength,

    an analytic integrated average of the Green's function

    is used. This integration is over a circular area

    equal in size to the sample lattice square area, Δ^2;

    the details are in Appendix B. This form is refered

    to as the "sampled real-space Green's function."

2) Replace $G_{D,N}(u,v,z)$ in the integral of equation (3.5)

    with a polynomial expansion about the center of the

    patch. A procedure for accomplishing this is presented

    in Appendix B. The resulting approximation for $\bar{G}_{D,N}$ is

    given the symbol $\bar{G}_{D,N}^{(2)}(r,s,z)$ with $r,s=-(N-1),\ldots,0,\ldots,N.$

$g_{D,N}^{(2)}(z)$ is as defined by equations (3.11) and (3.12)

with $\bar{G}_{D,N}$ replaced by $\bar{G}_{D,N}^{(2)}$; this form is referred to as

the "integrated real-space Green's function."

In the derivation of equations (3.10) and (3.11) the

definitions of the real-space sampling points given by

equations (3.3) and (3.4) were used. Because the DFT

requires an even number of sampling points, the definitions

(3.3) and (3.4) result in an asymmetric distribution of

points in the sampling of the Green's function [as in

equation (3.5)]; that is, there is an odd point at the

origin, N negative values, and N-1 positive values. By

redefining the real-space sampling, a symmetric distribution

of points may be obtained; the Green's function will then be

sampled over patches centered at $(r\Delta + \Delta/2, s\Delta + \Delta/2)$. This

shifted form of equation (3.5) is:

$$\tilde{G}_{D,N}(r,s,z) = \int_{r\Delta}^{(r+1)\Delta} \int_{s\Delta}^{(s+1)\Delta} G_{D,N}(u,v,z)\,du\,dv \quad (3.14),$$

with $r,s = -N,\ldots,0,\ldots(N-1)$. If a sampled approximation to

$\tilde{G}_{D,N}$ is used in equation (3.12), then one obtains the

"shifted sampled real-space Green's function," $g_{D,N}^{(3)}(z)_{\mu\nu}$.

When an integrated approximation to $\tilde{G}_{D,N}$ is used in equation

(3.12), one obtains the "shifted integrated real-space

Green's function," $g_{D,N}^{(4)}(z)_{\mu\nu}$. Use of the unshifted Green's functions is equivalent to replacing the field $\psi(x,y,z)$ with a patchwise constant field where each sampling point is centered in a patch; use of the shifted form corresponds to having the sampling point at one corner of its patch. If the same set of field values $\psi_{D,N}(l,m)$ are used for the sample points in both cases, the net result is a shift in the apparent location of the represented fields. This shift should be considered when theoretical fields are used, but it is of little consequence with experimentally measured fields, because with an experimentally measured field, there is always an ambiguity of half a sample spacing in the x and y directions when deciding how to represent the field with a patchwise constant field. Throughout this study, wavefronts propagated by the shifted Green's functions are compared to theoretical fields shifted $-\Delta/2$ in the x and y directions.

In order to determine $g_{D,N}(z)_{\mu\nu}$ from equation (3.11), it is necessary to perform the DFT operation. However, in the infinite and continuous formulation in equations (2.24-2.26) the Fourier transformed Green's function $\hat{G}_{D,N}(k_x,k_y,z)$ has a known (fairly simple) closed form. If an approximation for $g_{D,N}(z)_{\mu\nu}$ can be found in terms of $\hat{G}_{D,N}(k_x,k_y,z)$ in equations (2.25) and (2.26), then $g_{D,N}(z)_{\mu\nu}$ could be calculated without having to perform a DFT.

In order to derive such an approximation, equation (3.11) giving $g_{D,N}(z)_{\mu\nu}$ is expanded using equations (3.5), (3.8), (3.9), and (3.12), and the periodicity of the Fourier coeifficients, $\exp(-i\pi\mu l/N] = \exp(-i\pi\mu(l-2N)/N]$ is used. Equation (3.11) can then be written as:

$$g_{D,N}(z)_{\mu\nu} = \sum_{r=-N}^{N-1} \sum_{s=-N}^{N-1} e^{\frac{-i\pi}{N}(r\mu+s\nu)} \int_{(r-1/2)\Delta}^{(r+1/2)\Delta} \int_{(s-1/2)\Delta}^{(s+1/2)\Delta} G_{D,N}(x,y,z)\,dx\,dy$$

$$(3.15).$$

The Fourier transform of $G_{D,N}$ is expressed explicilty as:

$$\hat{G}_{D,N}(k_x,k_y,z) = \int_{-\infty}^{+\infty}\int_{-\infty}^{+\infty} e^{-i(k_x x+k_y y)} G_{D,N}(x,y,z)\,dx\,dy \quad (3.16).$$

In the following steps, the right-hand side of equation (3.16) will be approximated and compared with equation (3.15), providing a relationship between the $\hat{G}_{D,N}$ and $g_{D,N}$.

The integral of equation (3.16) is broken into a sum of patch integrals where $\exp[-i(k_x x+k_y y)]$ is approximated as constant over each patch. The result is $\hat{G}_{D,N} \approx \hat{G}'_{D,N}$ where:

$$\hat{G}'_{D,N}(k_x,k_y,z) =$$

$$\sum_{r=-\infty}^{\infty} \sum_{s=-\infty}^{\infty} e^{\frac{-i\pi}{N}(r\mu+s\nu)} \int_{(r-1/2)\Delta}^{(r+1/2)\Delta} \int_{(s-1/2)\Delta}^{(s+1/2)\Delta} G_{D,N}(x,y,z)\,dx\,dy$$

$$(3.17).$$

An estimate of the error from approximating $\exp[-i(k_x x+k_y y)]$ as constant over each patch is shown in Appendix C to be:

$$\left| \begin{array}{c} \hat{G}'_{D,N}(k_x,k_y,z) \\ \hline \hat{G}_{D,N}(k_x,k_y,z) \end{array} \right| = \left| \frac{k_x\Delta \quad k_y\Delta}{4\,\sin(k_x\Delta/2)\,\sin(k_y\Delta/2)} \right| \quad (3.18).$$

This error is limited if the 2N values of k_x and k_y are chosen so as to minimize the distance from the origin in k-space. This restriction along with consideration of the Fourier coefficients in equation (3.15) motivates the definitions:

$$k_{x\mu} = \begin{cases} \dfrac{\pi\mu}{N\Delta} & \text{if } 0 \leq \mu < N \\[2mm] \dfrac{\pi(\mu-2N)}{N\Delta} & \text{if } N \leq \mu < 2N \end{cases} \quad (3.19)$$

and similarly $k_{y\nu}$ in terms of ν. Evaluating (k_x,k_y) at $(k_{x\mu},k_{y\nu})$ and using equation (3.5) defining $\bar{G}_{D,N}$, equation (3.17) can be written:

$$\hat{G}_{D,N}(k_{x\mu},k_{y\nu},z) \approx$$
$$\sum_{r=-N}^{N-1}\sum_{s=-N}^{N-1} e^{-\frac{i\pi}{N}(r\mu+s\nu)} \sum_{m=-\infty}^{\infty}\sum_{n=-\infty}^{\infty} \bar{G}_{D,N}(r+2mN,s+2nN,z)$$
$$(3.20).$$

The m=n=0 term is simply $g_{D,N}(z)_{\mu\nu}$, so that equation (3.20) can be written as:

$$\hat{G}_{D,N}(\hat{k}_{x\mu},k_{y\nu},z) \approx$$
$$g_{D,N}(z)_{\mu\nu} + \sum_{r=-N}^{N-1}\sum_{s=-N}^{N-1} e^{-\frac{i\pi}{N}(r\mu+s\nu)} \sum_{\substack{m=-\infty \\ (m=n)\neq0}}^{\infty}\sum_{n=-\infty}^{\infty} \bar{G}_{D,N}(r+2mN,s+2nN,z)$$
$$(3.21).$$

One should note that if $\hat{G}_{D,N}(k_{x\mu},k_{y\nu},z)$ replaced $g_{D,N}(z)$ in equation (3.10), only the m=n=0 term of equation

(3.20) [the $g_{D,N}(z)_{\mu\nu}$ term in equation (3.21)] will yield

the result desired as in the discrete convolution of

equation (3.6). The summmation remaining in equation (3.21)

effectively extends the range of the summation in equation

(3.6) to include the infinite periodic extension of the

finite input data field. This extension may be viewed as

representing an infinite set of fictitious image sources; an

apparent copy of each field point is located at all of the

points (x+2mL,y+2nL) for all pairs of integers (m,n). These

fictitious image sources can produce large errors in

numerical calculations of propagation.

If $G_{D,N}(x,y,z)$ falls off rapidly with x and y, then

$\bar{G}_{D,N}(x,y,z)$ also falls off rapidly, and the effects of image

sources will be small. In this case the summation in

equation (3.21) may be ignored, and equation (3.21) then

shows that $\hat{G}_{D,N}(k_{x\mu},k_{y\nu},z)$ approximates $g_{D,N}(z)_{\mu\nu}$ directly.

This approximation is called the "sampled k-space Green's

function", is labeled $g_{D,N}^{(5)}(z)_{\mu\nu}$, and is defined by:

$$g_{D,N}^{(5)}(z)_{\mu\nu} = \hat{G}_{D,N}(k_{x\mu},k_{y\nu},z) \qquad (3.22).$$

On the other hand if $G_{D,N}(x,y,z)$ does not fall off

rapidly, then the sum in equation (3.21) may be significant

and $\hat{G}_{D,N}$ may be an unacceptable approximation of $g_{D,N}$.

Inspection of equations (3.16-3.21) shows that this sum

could be reduced if $G_{D,N}(x,y,z)$ in equation (3.16) were replaced by $G_{D,N}(x,y,z)$ multiplied by a suitable window function $W(x,y)$. This window function should have a value near unity for x and y in the range $[-L,L]$ and should fall off rapidly outside this range. Such a window would reduce any fictious image sources without introducing any new error.[3.1] A simple closed form function $\hat{G}'_{D,N}$ is sought such that:

$$\hat{G}''_{D,N}(k_x,k_y,z) = \int_{-\infty}^{+\infty}\int_{-\infty}^{+\infty} e^{-i(k_x x + k_y y)} W(x,y) G_{D,N}(x,y,z)\,dxdy$$

(3.23),

and the same process outlined in equations (3.16-3.21) yield an expression analogous to equation (3.21):

$$\hat{G}''_{D,N}(k_{x\mu},k_{y\nu},z) \approx g_{D,N}(z)_{\mu\nu} +$$
$$\sum_{r=-N}^{N-1}\sum_{s=-N}^{N-1} e^{-\frac{i\pi}{N}(r\mu+s\nu)} \sum_{\substack{m=-\infty \\ (m=n)\neq 0}}^{\infty}\sum_{n=-\infty}^{\infty} W(r+2mN,s+2nN)\bar{G}_{D,N}(r+2mN,s+2nN,z)$$

(3.24).

Because of the window function, this summation is not as significant as that of equation (3.21) regardless of how fast $G_{D,N}(x,y,z)$ decreases with increasing x and y.

Ideally the value of the window function would be unity within the limited range (corresponding to $m=n=0$) and zero outside, but neither equation (3.23) nor its equivalent convolution integral in k-space yield a simple closed-form expression for such a window. The goal here is to reduce the computation time of $g_{D,N}(z)_{\mu\nu}$ in equation (2.11);

therefore a window for which equation (3.23) can be evaluated analytically is necessary.

The "radial sinc function," $2J_1(k_0 r)/k_0 r$ [$J_1(z)$ is the first order Bessel function, $k_0 = \pi/L$, and $r^2 = x^2 + y^2$)] is a suitable window function. It does provide a simple and closed form expression for $\hat{G}''_{D,N}$. This window function reduces the sum in equation (3.23) so that $\hat{G}''_{D,N}(k_{x\mu}, k_{y\nu}, z)$ more accurately approximates $g_{D,N}(z)_{\mu\nu}$ than $\hat{G}_{D,N}(k_{x\mu}, k_{y\nu}, z)$. Using the convolution theorem, it can be shown that $\hat{G}''_{D,N}$ for this window is approximately an integrated average of $\hat{G}_{D,N}$ over an annular region around points (k_x, k_y). This function $\hat{G}''_{D,N}$ is the integrated k-space Green's function, labeled $g^{(6)}_{D,N}(z)_{\mu\nu}$; which is defined as[35]

$$g^{(6)}_{D,N}(z)_{\mu\nu} = \begin{cases} \dfrac{1}{2 k_r k_0} \displaystyle\int_{k_r - k_0}^{k_r + k_0} \hat{G}_{D,N}(k'_r, z) k'_r \, dk'_r & k_r \geq k_0 \\[3ex] \dfrac{2}{k_0^2} \displaystyle\int_0^{k_0} \hat{G}_{D,N}(k'_r, z) k'_r \, dk'_r & k_r = 0 \end{cases}$$

(3.25)

where $k_r^2 = k_{x\mu}^2 + k_{y\nu}^2$. Closed form evaluations are presented in Appendix C.

B. Qualitative examination of the Green's functions

and their dependence on propagation distance

In the preceding sections it was shown that although
analytic expressions exist for holographic processing with
uniquely specified Green's functions, the use of finite and
discrete expressions, as requircd by data acquisition of
digitial processing, introduces errors. To reduce these
errors, the exact analytic Green's functions or their
Fourier transforms may be sampled or represented in various
ways producing improved finite and discrete expressions.
Covering a wide range of possibilities, six different
discrete forms, $g_{D,N}^{(1)}(z)_{\mu\nu}$ through $g_{D,N}^{(6)}(z)_{\mu\nu}$, have been
introduced. In the next section a realistic computer model
will be used to find the best discrete form for a given
situation. Before doing a quantitative comparison, it will
be worthwhile to examine the exact Green's functions to gain
a qualitative understanding of the sources and corrections
for the errors encountered in going from the continuous
analytic expressions to discrete and finite forms.

An important parameter affecting the nature of the
Green's functions is the propagation distance z; the Green's
functions, equations (2.21) and (2.22), and their Fourier
transforms, equations (2.25) and (2.26), change

significantly as z varies from a fraction of a wavelength to several wavelengths. This particular range of propagation distance is of great interest in NAH applications. In this subsection, plots of the Dirichlet and Neumann Green's functions and their Fourier Transforms are presented for propagation distances of a fraction of a wavelength and several wavelengths.

B.1. Dirichlet boundary conditions

The analytic Fourier transform of the Dirichlet Green's function, equation (2.25), is plotted in Figure 3.1a for the small distance $z/\lambda = 0.13$ and extending over a typical range of k_x with $k_y = 0$. The slowly-varying nature of the function allows for easy sampling with a uniform spacing of points (k_x, k_y).

The real-space function, equation (2.21), for the same distance z/λ is plotted in Figure 3.1b. Since the source fields considered in this paper are assumed to be negligible outside a region of length L, the Green's functions in real-space need only be considered in the range $(-L, L)$. However, in contrast to the k-space form, the spiked shape of the real-space function makes it difficult to sample with
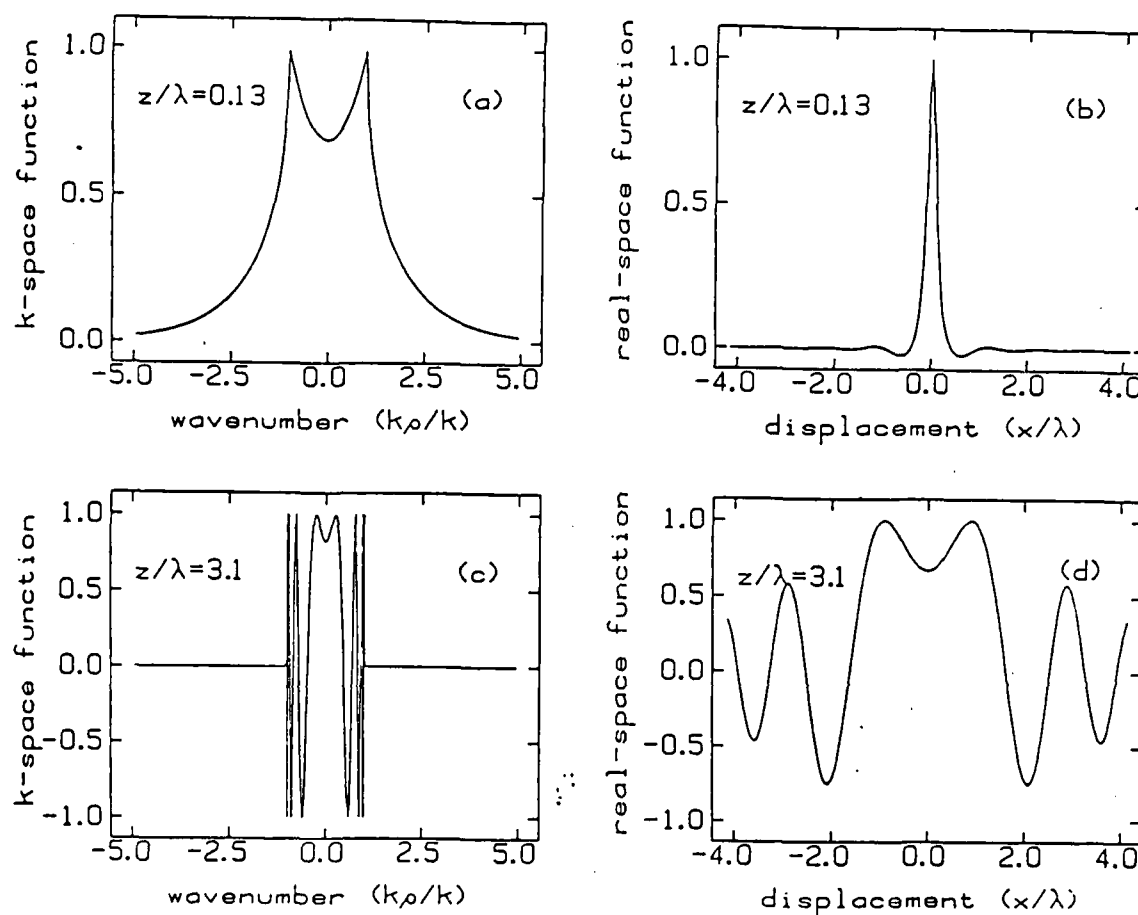
Fig. 3.1   The real part of the Dirichlet pressure Green's function plotted over typical ranges (a) in k-space and (b) in real-space for small propagation distance and (c) plotted in k-space and (d) in real-space for more than three wavelengths propagation distance.

a finite number of points with regular spacing; it becomes impossible as z goes to zero and the function becomes singular.

Figures 3.1a and 3.1b suggest that for small distances ($z/\lambda < 0.5$) a direct sample of the k-space Green's function will yield good results. This expectation is also consistent with the relationship of $g_{D,N}^{(5)}(z)$ to $g_{D,N}(z)$ developed in section A.3. and summarized by equations (3.21) and (3.22). Since most of the area under the curve of Figure 3.1b is contained in a relatively small area around x=y=0, the sum in equation (3.21), which quantifies the fictitious image source error, will be very small, and hence $g_{D,N}(z)$ will be represented well by $g_{D,N}^{(5)}$. For small distances z/λ, conditions are not favorable for the direct sampling of the real-space function due to the singularity at x = y = z = 0. Instead of a direct sampling of the real-space function, a more sophisticated approximation of the integration in equation (3.5) is needed, such as $g_D^{(2)}(z)$ or $g_D^{(4)}(z)$.

Figures 3.1c and 3.1d are plots of the analytic transform and real-space form of the Dirichlet Green's function for z greater than three wavelengths ($z/\lambda = 3.1$). The analytic transform represents the real-space Green's function of infinite extent. This function does not fall off

rapdily in real space, and this shows up in k-space as the
rapid oscillations of Figure 3.1c which are very difficult
to sample directly as in $g_D^{(5)}(z)$. The Green's function for
this distance might be represented by the integrated average
k-space form $g_D^{(6)}(z)$; however, the slow variation evident in
Figure 3.1d suggests that a direct sampling of the
real-space function will be an adequate representation of
the propagator. Using one of the real-space Green's
function forms, $g_D^{(1)}(z)$ through $g_D^{(4)}(z)$, along with
augmenting the data field with zeros as in equation (3.6),
will eliminate the fictitious image source error.

B.2. Neumann boundary conditions

The analytic transform of the Neumann Green's function,
equation (2.26), is plotted for small z/λ in Figure 3.2a
while the real space function, equation (2.22), is plotted
in Figure 3.2b. Unlike the well-behaved function plotted in
Figure 3.1a the singularity of the k-space Neumann Green's
function makes it unsuitable for direct sampling as $g_N^{(5)}(z)$.
The integrated average, $g_N^{(6)}(z)$, is necessary to sample the
Green's function from k-space. While the k-space function
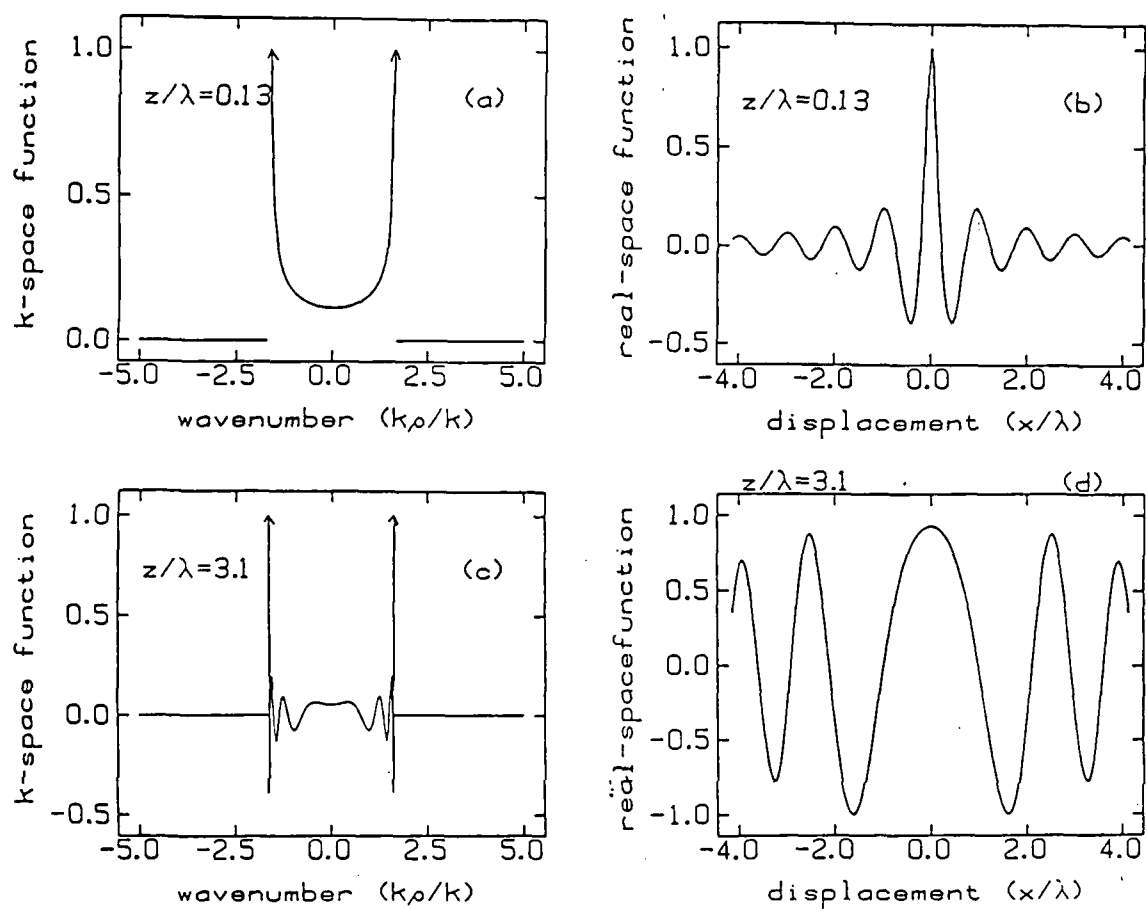
Fig. 3.2   The real part of the Neumann Green's function normalized to the largest value plotted and displayed over typical ranges (a) in k-space and (b) in real-space for short propagation distance, and (c) in k-space and (d) in real space for a few wavelengths propagation distance.

is singular on the radiation circle $k_x^2 + k_y^2 = k^2$ for all

distances z/λ, the real space function is singular only at

the point $x=y=z=0$. This singularity presents no computa-

tional problem if either $g_N^{(2)}(z)$ or $g_N^{(4)}(z)$ is used to

represent $g_N(z)$.

The k-space form of the Green's function for Neumann

boundary conditions at the larger distance $z = 3\lambda$, depicted

in Figure 3.2c, shows the same rapid oscillations as the

Dirichlet version, and it is also singular on the radiation

circle. The integrated form $g_N^{(6)}(z)$ must be used if a

k-space Green's function is used, but again, the slow

variation of the real space form, Figure 3.2d, suggests

using one of the real space forms $g_N^{(1)}(z)$ through $g_N^{(4)}(z)$.

The eight plots of the Green functions presented are

representative of all the cases studied. They are intended

to serve as a basis for understanding the results of the

computational experiments presented below.

C. Quantitative comparison of the sampled Green's functions

The purpose of this section is to present a

quantitative comparison of the effectiveness of the six

sampled Green's function forms, $g_{D,N}^{(1)}(z)$ through $g_{D,N}^{(6)}(z)$ when

they are used in each of the four processes: propagation, transformation, reconstruction, and inverse transformation. The comparisons span a suitable range of separation distance between the input and output fields for each case. To compare the six forms, readily calculated fields $\psi^0(x,y,z)$ and $\frac{\partial\psi}{\partial z}(x,y,z)$ of a tractable, theoretical boundary condition $\psi_N(x,y)$ are used. These fields are used as simulated input fields, or holograms, and as absolute reference fields in comparisons of the six output fields. An output field $\psi^{(i)}(x,y,z)$ or $\frac{\partial\psi^{(i)}}{\partial z}(x,y,z)$ is associated with each sampled Green's function $g_{D,N}^{(i)}(z)$, $i = 1,\ldots,6$, used in the numerical processing of the input data.

Since the processing problems which have been discussed have direct relevance to Nearfield Acoustic Holography it is natural to test and compare the different Green's function froms $g_{D,N}^{(i)}(z)$ in simulated experiments with an acoustic pressure field, $\psi(x,y,z) = p(x,y,z)$. The Neumann boundary condition, and $-i\frac{\partial\psi}{\partial z}(x,y,z)$ for any z, are specified in terms of the z-component of the particle velocity defined by

$$v_z(x,y,z) = \frac{-i}{\rho c k} \frac{\partial}{\partial z} p(x,y,z) \qquad (3.26),$$

where ρc is the characteristic acoustic impedance.

C.1. A theoretically tractable boundary condition: the baffled piston

The computationally tractable and relatively nonsingular acoustic pressure field of an oscillating piston in an infinite baffle is used for the NAH simulations. In particular, the chosen source is a baffled piston of radius $a = 3.44/k$ and surface velocity amplitude u_0. This source radiates into a medium with a characteristic impedance ρc.

Calculating the theoretical field for each field point requires the evaluation of a one-dimensional integral with fixed limits. From equations (2.20-2.22 and 3.26) the fields produced by the piston are given by

$$p^0(x,y,z) = \frac{i\rho c k u_0}{2\pi} \int_0^{2\pi} \int_0^{ka} \frac{e^{ikR}}{R} \, r \, dr \, d\theta \qquad (3.27)$$

and

$$v_z^0(x,y,z) = \frac{u_0}{2\pi} \int_0^{2\pi} \int_0^{ka} z(1-ikR) \, \frac{e^{ikR}}{R^3} \, r \, dr \, d\theta \qquad (3.28),$$

where $R^2 = (x^2 + y^2) + r^2 - 2(x^2 + y^2)^{1/2} \cos(\theta) + z^2$.

Equations (3.27) and (3.28) can be reduced to the following one dimensional integrals:[36]

$$p^0(x,y,z) = \frac{\rho c u_0}{2\pi} \left\{ \int_0^\pi e^{ikR} \left[\frac{b \cos(\theta) - 1}{1 + b^2 - 2b \cos(\theta)} \right] d\theta + \alpha(b) e^{ikz} \right\}$$

$$(3.29)$$

and

$$v_z^0(x,y,z) = \frac{u_0}{2\pi}\left\{ \int_0^\pi \frac{z}{R}\, e^{ikR}\left[\frac{b\cos(\theta) - 1}{1 + b^2 - 2b\cos(\theta)}\right]d\theta + \alpha(b)e^{ikz}\right\}$$

(3.30),

where $b^2 = (x^2 + y^2)/a^2$ and

$$\alpha(b) = \begin{cases} 0 , & b > 1 \\ \pi , & b = 1 \\ 2\pi , & b < 1 \end{cases}.$$

C.2. Sampling the theoretical field

By numerical integrations of equations (3.29) or (3.30) with a fixed value of z, the fields $p^0(x,y,z)$ or $v_z^0(x,y,z)$ are evaluated at each of the coordinate locations (x_l, y_m), defined in equations (3.3) and (3.4), yielding a 64 x 64 array. Each element of the array is a complex number specifying the field amplitude and phase at the point (x_l, y_m, z). Elements of these arrays are written as p_{lm}^0 or v_{lm}^0 with the value of z taken from context if not explicitly indicated.

C.3. Quantifying the error in the output fields

In order to evaluate the relative accuracy of the different Green's functions the output fields $\psi_{lm}^{(i)}$ processed with $g_{D,N}^{(i)}$ are compared with the reference fields p_{lm}^0 or v_{lm}^0, and an average difference and standard deviation are determined. All quantities are normalized by the largest magnitude of the reference field in the array.

The difference in the real (Re) and imaginary (Im) parts at each point are defined as

$$\Delta_{lm}^{R(i)} = \left\{ \mathrm{Re}\left[\psi_{lm}^{(i)}\right] - \mathrm{Re}\left[\psi_{lm}^0\right] \right\} / \max\left[\left|\psi_{lm}^0\right|\right] \quad (3.31)$$

and

$$\Delta_{lm}^{I(i)} = \left\{ \mathrm{Im}\left[\psi_{lm}^{(i)}\right] - \mathrm{Im}\left[\psi_{lm}^0\right] \right\} / \max\left[\left|\psi_{lm}^0\right|\right] \quad (3.32).$$

The average difference is defined as

$$\bar{\Delta}^{(i)} = \left\{ \sum_{l=0}^{63} \sum_{m=0}^{63} \left[\Delta_{lm}^{R(i)} + \Delta_{lm}^{I(i)}\right] \right\} / 8192 \quad (3.33)$$

and the standard derivation is

$$\sigma^{(i)} = \left\{ \sum_{l=0}^{63} \sum_{m=0}^{63} \left\{ \left[\Delta_{lm}^{R(i)} - \bar{\Delta}^{(i)}\right] + \left[\Delta_{lm}^{I(i)} - \bar{\Delta}^{(i)}\right] \right\} / 8192 \right\}^{1/2}$$
$$(3.34).$$

The results of each case are summarized in a chart such as that of Figure 3.3a. A bar is drawn for each function

$g_{D,N}^{(i)}(z)$, $i = 1$ to 6, with the center drawn a distance $\bar{\Delta}$ from the zero axis while the top and bottom are drawn a distance $+\sigma$ and $-\sigma$ from the center.

To further illustrate the effectiveness of each method, several plots are presented which display a central cross section of either the real or imaginary part of the output field $\psi_{lm}^{(i)}$ represented by crosses, against the corresponding reference field p_{lm}^0 or v_{lm}^0 represented by a solid line.

C.4. Test results for wavefront propagation

In this section, charts and plots are presented which quantify and illustrate the effectiveness of the sampled Green's function forms when used to propagate a pressure wavefront and to transform and propagate a z-component of the particle velocity wavefront. As defined in chapter II, these processes are the numerical evaluations of equations (2.28) and (2.29) for fixed $z-z_0 > 0$. Data for four different values of $(z-z_0)/\lambda$ are presented (to simplify notation in the figures $(z-z_0)/\lambda$ is written z/λ).

The chart in figure (3.3a) graphically displays the average differences $\bar{\Delta}^{(i)}$ and standard deviations $\sigma^{(i)}$ of the output fields $p_{lm}^{(i)}(z=0.006\lambda)$ from the field $p_{lm}^0(z=0.006\lambda)$

Fig. 3.3   The normalized error (defined in equations 47 and 48) produced by each of the six Green's function sampling methods when used to propagate the pressure field progressively larger z-distances, (a), (b), (c), and (d) from an input theoretical baffled piston pressure field.

when the input field is the pressure at the theoretical

piston source boundary, $p^0_{lm}(z_0=0)$. The k-space Green's

function, equation (2.25), is well behaved for small $(z-z_0)$

and so requires only a simple representation; figure (3.3a)

shows that $g_D^{(5)}(z-z_0)$ and $g_D^{(6)}(z-z_0)$ do yield good results

for very small propagation distance. The real-space Green's

function, equation (2.21), is nearly singular for small

$(z-z_0)$ and so requires a sophisticated represenation; figure

(3.3a) shows that, of the real-space forms, $g_D^{(4)}(z-z_0)$

yields the best results for very small propagation

distances.

The input field for the chart of figure 3.3b is again

$p^0_{lm}(z_0=0)$ while the six output fields are $p^{(i)}_{lm}(z=0.13\lambda)$.

At this distance, all six functions yield good results.

For the chart in figure 3.3c, the input field is

$p^0_{lm}(z_0=0.13\lambda)$ and the output fields are $p^{(i)}_{lm}(z=1.1\lambda)$. At

this distance the error from any of the real-space forms is

about one third that of either k-space form. There is little

difference between the errors from the four real-space

forms. In general at yistances $(z-z_0) \geq \lambda/2$, the real space

forms, $g_D^{(1)}(z)$ through $g_D^{(4)}(z)$, provide better results than

the k-space forms.

For a propagation distance of several wavelengths, the chart in figure 3.3d indicates that all of the real-space Green's function sampling forms $g_D^{(1)}(z)$ through $g_D^{(4)}(z)$ yield similar, good results. The relative error of the the k-space forms grows quickly with an increase in propagation distance with $g_0^{(5)}$ giving the largest error. This large error is due to unattenuated fictitious image sources.

The charts of figure 3.3 suggest that the shifted, integrated real-space Green's function $g_D^{(4)}(z)$ is the best choice for a single function which will yield good results over the range of $(z-z_0)$ considered here. The plots of figures 3.4 and 3.5 further illustrate the deficiencies of the other functions in comparison with the merits inherent in $g_0^{(4)}(z)$. In figure 3.4a a central cross section of the imaginary part of the output field $p_{lm}^{(3)}(z=0.006\lambda)$ is plotted with the imaginary part of $p_{lm}^0(z=0.006\lambda)$ while the same is done for $p_{lm}^{(4)}(z=0.006\lambda)$ in figure 3.4b. In both cases the propagation distance $(z-z_0)$ was 0.006λ. Figure 3.4a shows that $p_{lm}^{(3)}$ underestimates the imaginary part of the field while figure 3.4b shows that $p_{lm}^{(4)}$ is a much better approximation. As a first order approximation of $\tilde{G}_D(z)$,
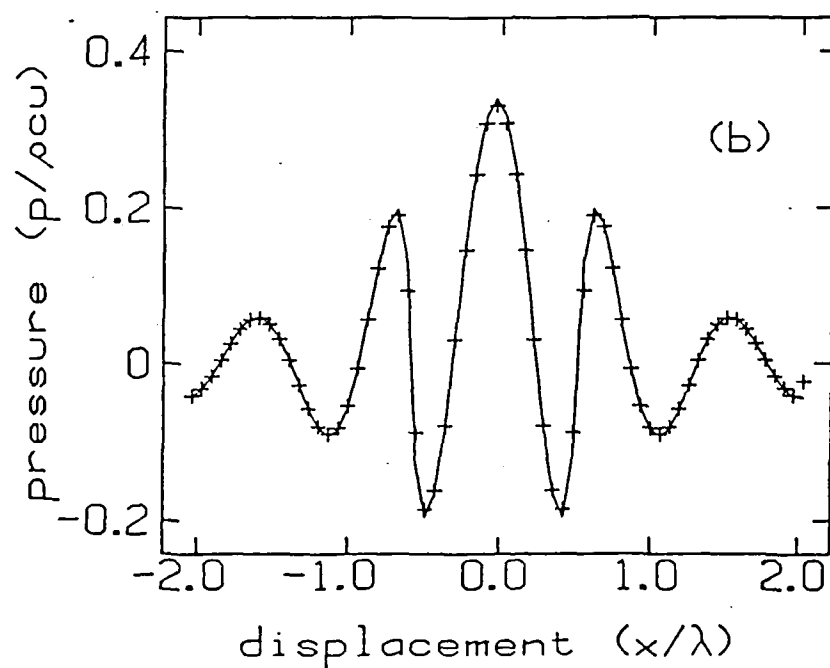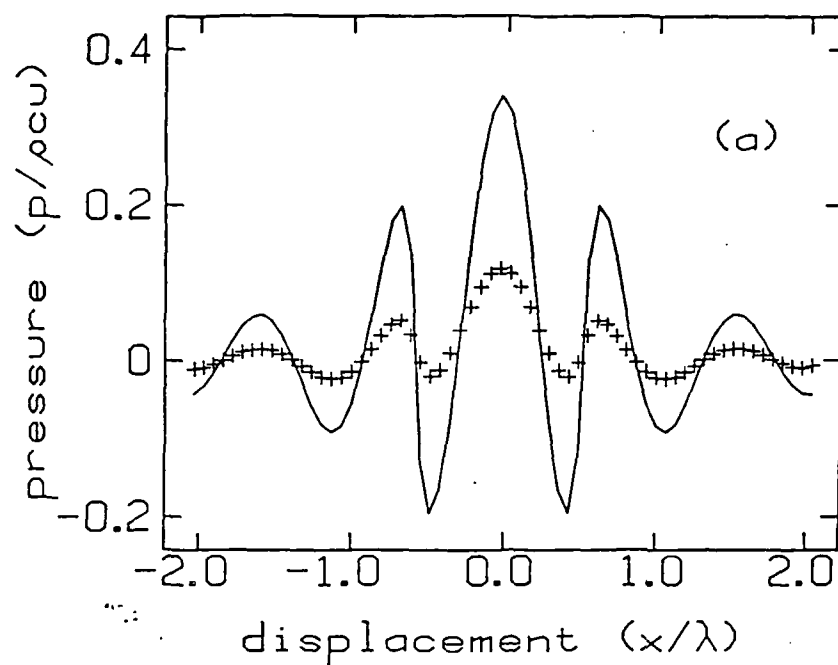
Fig. 3.4 The imaginary part of the pressure 0.006 wavelengths from the plane of a theoretical baffled piston source generated from an input pressure field sample taken at the source using (a), plus signs, $g_D^{(3)}(z)$ and (b), plus signs, $g_D^{(4)}(z)$ against the theoretical field, solid line.
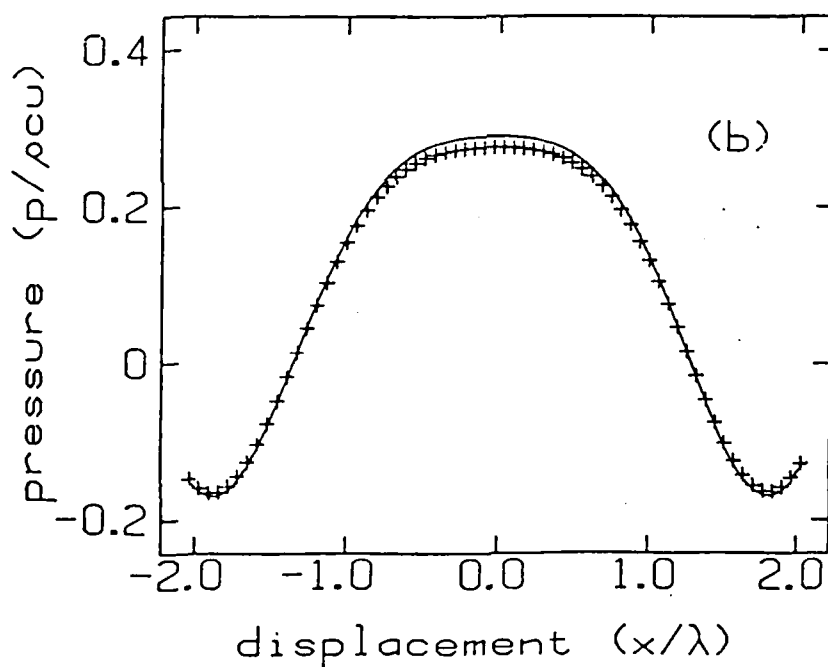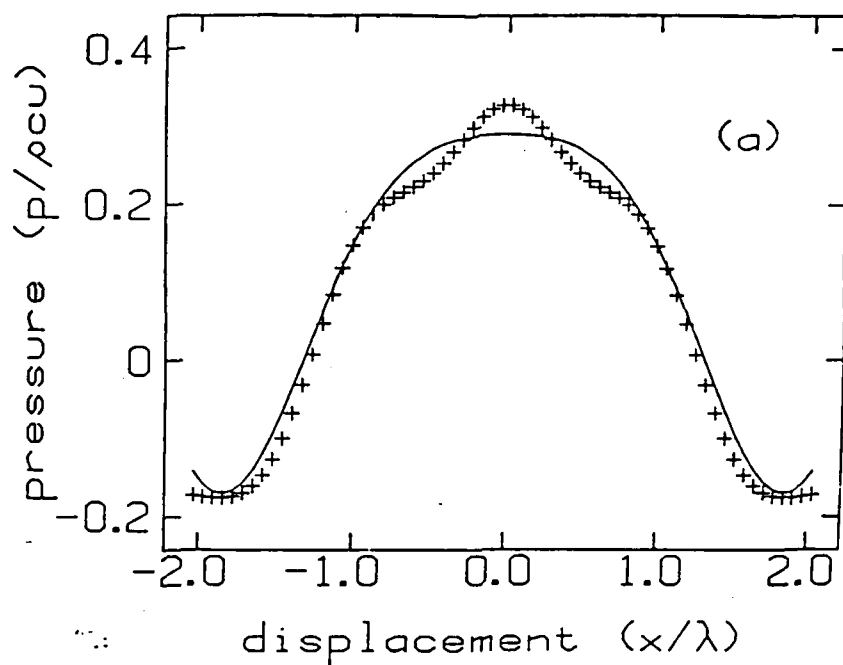
Fig. 3.5   The real part of the pressure 3.1λ from the plane
of a theoretical baffled piston source generated from an
input pressure field sample taken 0.13 $L from the source
using (a), plus signs, $g_0^{(5)}(z)$ and (b) plus signs $g_0^{(4)}(z)$.
Theory is the solid line.

equation (23), $g_D^{(3)}(z)$ apparently cannot represent the behavior of the nearly-singular real-space Green's function at very small distances. The higher order approximation $g_D^{(4)}(z)$ does appear to represent the effect of this behavior well.

For propagating over distances of a wavelength or more, the effects of image sources should degrade the performance of the k-space forms $g_D^{(5)}(z)$ and $g_D^{(6)}(z)$. Figure 3.5a clearly shows an interference effect from these image sources in the plot of $p_{lm}^{(5)}(z=3.2\lambda)$ against $p_{lm}^0(z=3.2\lambda)$ where $(z-z_0)$ was 3.1λ. The integrated real-space form does not suffer from any fictitious image source error as can be seen in figure 3.5b where $p_{lm}^{(4)}(z=3.2\lambda)$ is compared with $p_{lm}^0(z=3.2\lambda)$, the same conditions as in figure 3.5a.

The charts and plots of figures 3.3, 3.4 and 3.5 compare the utility of the six Green's function sampling methods when used in the numerical evaluation of equation (2.28). The charts and plots of figures 3.6, 3.7, and 3.8 do the same type of comparison for numerical evaluations of equation (2.29). The chart in figure 3.6a displays the average differences $\bar{\Delta}^{(i)}$ and standard deviations $\sigma^{(i)}$ of the output fields $p_{lm}^{(i)}(z=0)$ compared to the reference field
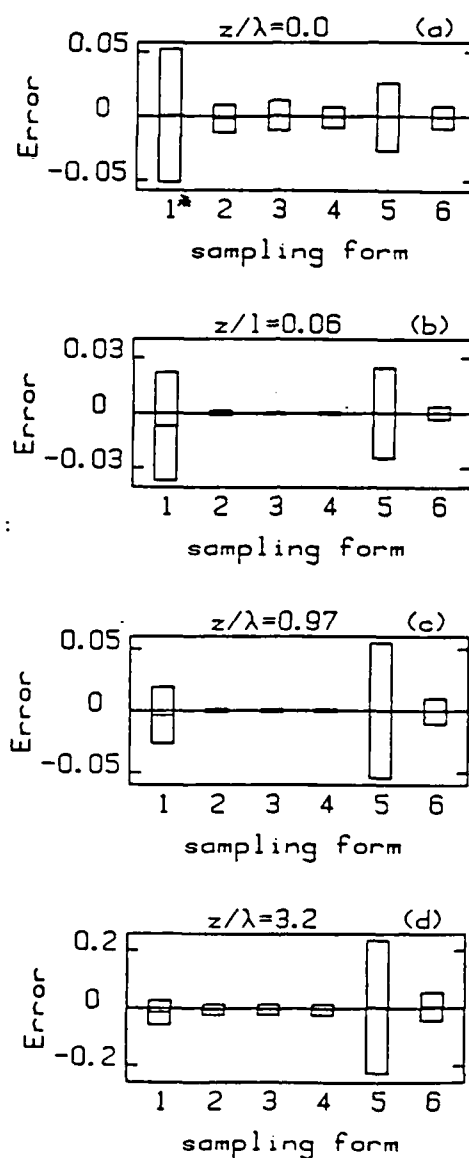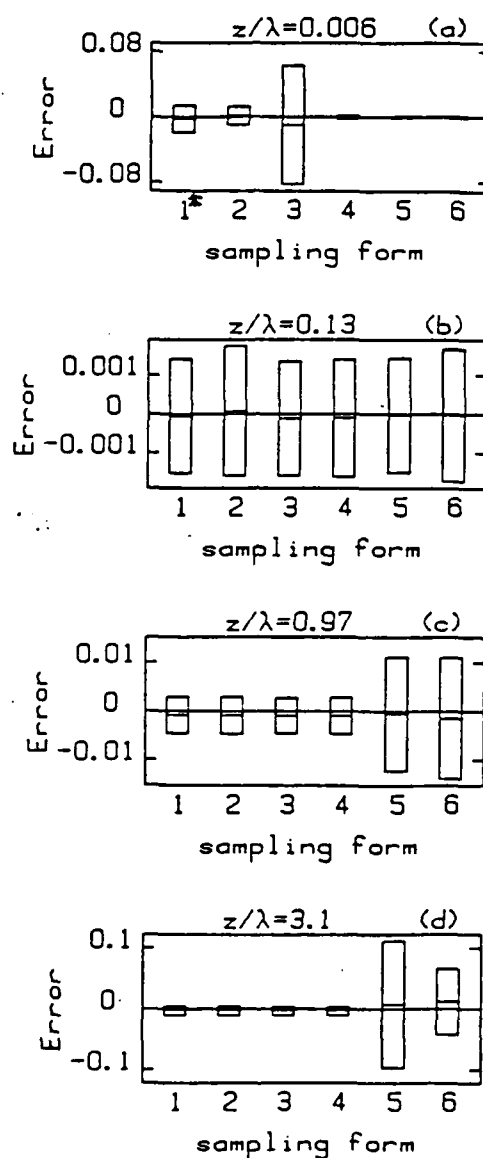
Fig. 3.6   The normalized error produced by each of the six
Green's function sampling methods when used to propagate the
pressure field progressively larger distances, (a), (b),
(c), and (d), from an input theoretical z-component of the
particle velocity boundary field.

$p_{lm}^0(z=0)$. The input field is the normal component of the surface velocity at the theoretical piston source boundary, $v_{lm}^0(z_0=0)$. Functions $g_N^{(4)}(z)$ and $g_N^{(6)}(z)$ yield the best results for this transformation from $v_{lm}^0(z_0=0)$ to $p_{lm}^{(i)}(z=0)$.

Unlike the functions $g_D^{(i)}(z)$, there appears to be no value of $(z-z_0)$ where all $g_N^{(i)}(z)$ produce similar results; this can be seen in figures 3.6a through 3.6d. The function $g_N^{(4)}(z)$ yields as good results as any function over the range of distances $(z-z_0)$ considered. The real-space forms $g_N^{(2)}(z)$ and $g_N^{(3)}(z)$ are only slightly inferior to $g_N^{(4)}(z)$ for use when the distance $(z-z_0)$ is small. The real space form $g_N^{(1)}(z)$ starts out the worst of all six forms and steadily improves with propagation distance while the k-space forms decrease in performance with increasing propagation distance.

Figures 3.7a and 3.7b compare with $p_{lm}^0(z=0)$ the fields $p_{lm}^{(5)}(z=0)$ and $p_{lm}^{(4)}(z=0)$ respectively as produced with $g_N^{(5)}(z=0)$ and $g_N^{(4)}(z=0)$. Against $p_{lm}^0(z=3.2\lambda)$, the fields $p_{lm}^{(5)}(z=3.2\lambda)$ and $p_{lm}^{(4)}(z=3.2\lambda)$, as produced with $g_N^{(5)}(z=3.2\lambda)$ and $g_N^{(4)}(z=3.2\lambda)$, are compared in figures 8a and 8b
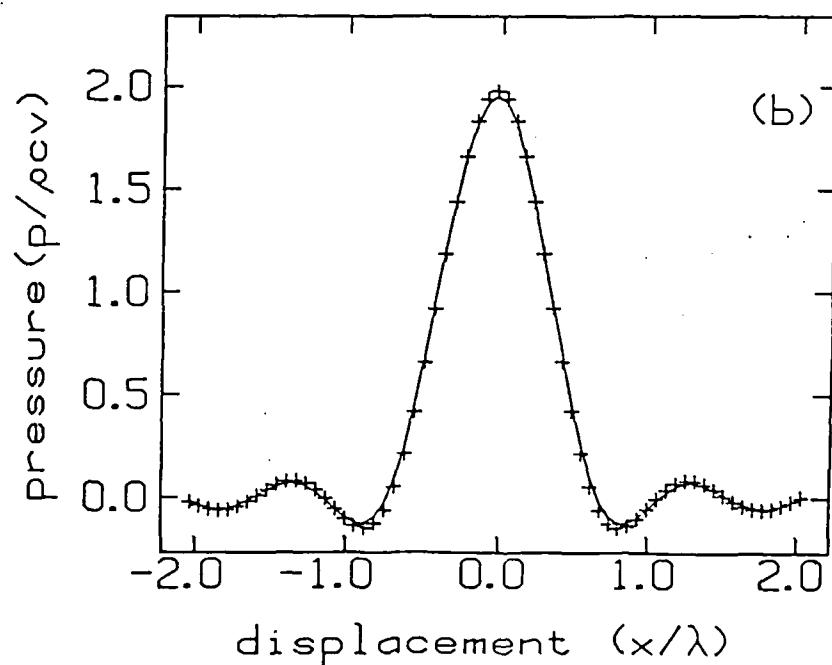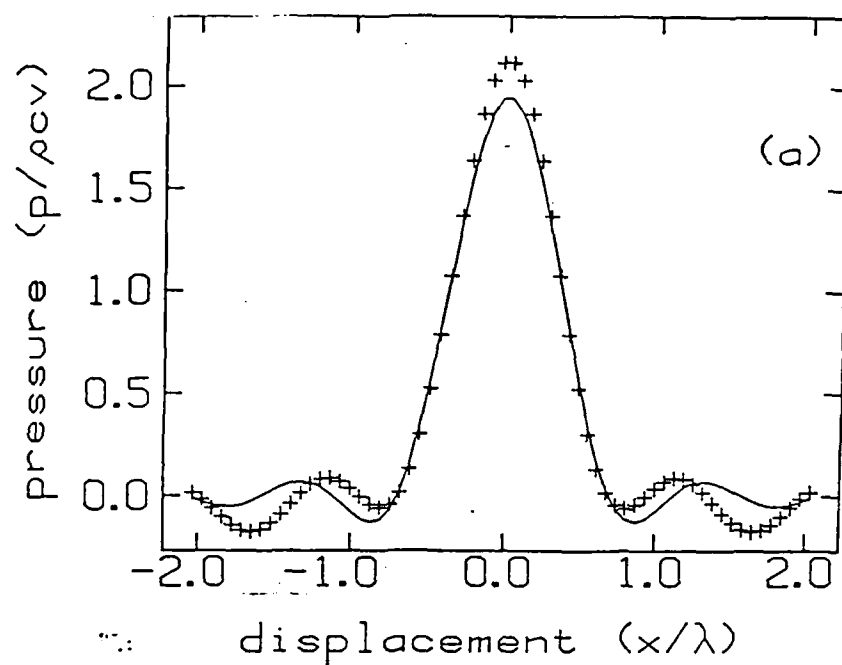
Fig. 3.7   The real part of the pressuce in the plane of a baffled piston source along a center row of the output generated field array produced using (a), plus signs, $g_N^{(5)}(z)$ and (b), plus signs, $g_N^{(4)}(z)$ with the z-component of the particle velocity in the same plane as input to the processing routines. The solid lines represent the theoretical value.
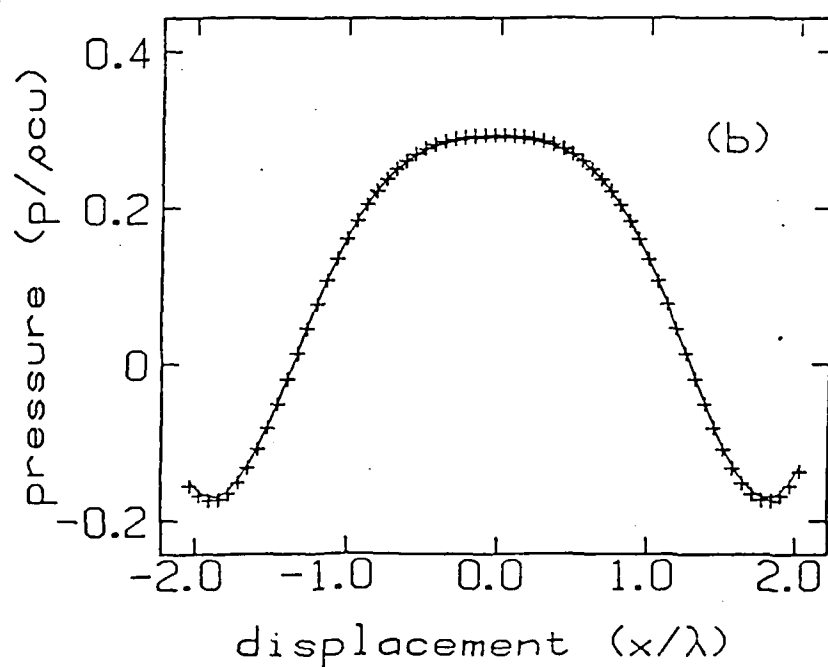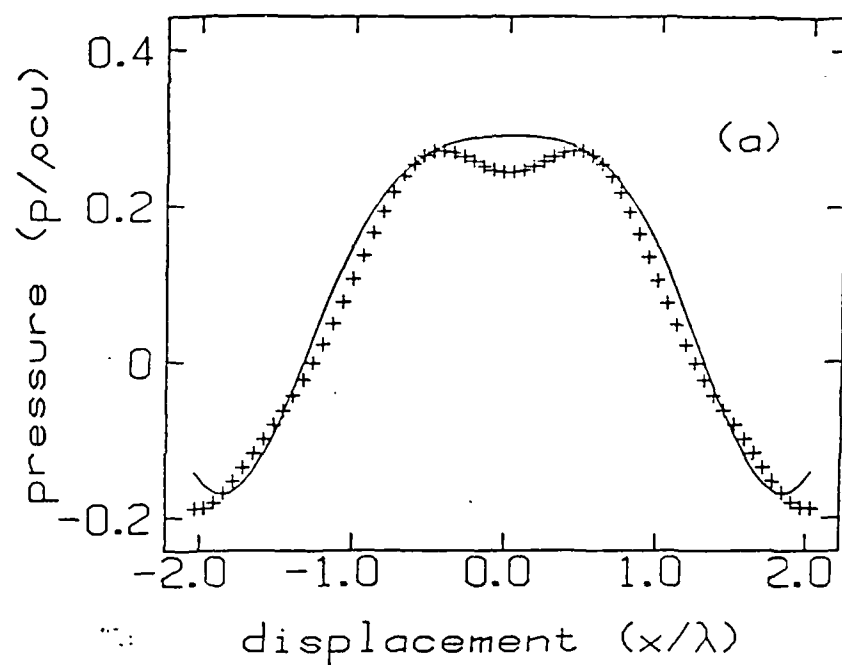
Fig. 3.8   The real part of the pressure field 3.2 λ from the input baffled piston as produced starting with the z-component of velocity at the source plane using (a), plus signs, $g_N^{(5)}(z)$ and (b), plus signs, $g_N^{(4)}(z)$.   The solid lines plot theory.

respectively. In both figures 3.7a and 3.8a, the effects of fictitious images introduced by $g_N^{(5)}(z)$ are seen. By contrast both 3.7b and 3.8b show the good agreement obtained with $g_N^{(4)}(z)$.

D. Conclusion and summary

Over the full range of distances $(z-z_0)$ considered and for both propagation problems and problems of transformation and propagation, the shifted integrated real-space Green's functions $g_{D,N}^{(4)}(z)$ appear to yield consistently good results. This consistency makes this form ideal for computation.

Section III developed the theory for approximating the infinite and continuous integrals with finite and discrete forms. The approximation was based on two main assumptions: First, the boundary field can be neglected outside of a finite region, and second, this field can be adequately represented by a patchwise constant field for reasonably small patches. If these two assumptions are satisfied, it was shown that the problem was to represent the known Green's function in a discrete form, and six methods for accomplishing this were developed. A qualitative examination of the actual form of the Green's functions was given in section IV. This was done to identify the

difficulties in representing the Green's functions and to
identify how these difficulties might be overcome by one or
more of the six methods. The results of testing presented
in section V.E suggest the use of the shifted integrated
real space Green's function, $g_{D,N}^{(4)}(z)$, for acoustic
propagation problems. The results show this form produced a
minimum of error for propagation distances from zero to
several wavelengths.

Chapter IV

SOURCE FIELD RECONSTRUCTION FROM PLANAR HOLOGRAMS

In this chapter, the inverse of the problem considered in the last chapter is examined. Here it is assumed that a known planar hologram $\Psi(p,q,z_H)$ accurately represents the field in the hologram plane, and that the field between the hologram plane and the source plane, z=0, is sought.

In the first section of this chapter, the numerical reconstruction of source fields is developed as a direct approximation to the continuous formulation of equation (2.27). This is essentially the technique suggested in the original Nearfield Acoustic Holography paper[1] with minor improvement.

The second section presents test results illustrating the suitability of the reciprocals of the six Green's function sampling methods, developed in chapter III, as inverse propagators with the method of section A.

An important original contribution of the first section of this chapter the definition of error sources in the numerical method there described. The identification of these errors motivate the search for alternative deconvolution methods, and in the last section, an alternative numerical source field reconstruction method is

presented. This method is based on the theory developed in chapter III . That theory led to equation (3.6) which can be written in matrix form:

$$\Psi(r,z_H) = \sum_{s=0}^{N^2-1} \left[G_{D,N}(z_H) \right]_{rs} \Psi_{D,N}(s) \qquad (4.1),$$

where the N^2 unique index pairs (p,q) and (l,m) of equation (3.6) are themselves indexed respectively by the indicies r and s, and where the elements of the N^2 x N^2 matrix $\left[G_{(D,N)}(z_H) \right]_{rs}$ are $\bar{G}_{D,N}(p-l,q-m,z_H)$. The source field reconstruction problem would be solved by inverting this matrix, but inverting this matrix for large N would require excessive computational capabilities and will preclude easy high speed data processing. The stability of such an inversion is also suspect. However, iterative methods for solving this equation without inverting the matrix are quite feasable. Such a method for solving equation (4.1) is presented in section C.

A. Deconvolution with the Discrete Fourier Transform and Smoothing

For the case of infinite and continuous fields, the convolution theorem provides an exact formula for the deconvolution or reconstruction of $\Psi_{D,N}(x,y)$ from $\Psi(x,y,z_H)$,

as in equation (2.27). It would be tempting to try the same technique with the discrete convolution given in equation (3.10). One could write

$$\Psi'_{D,N}(l,m) = IDFT[DFT\{\Psi(p,q,z_H)\}/g_{D,N}(z_H)] \qquad (4.2).$$

However, equation (3.10) can be derived (without approximations) only if the DFT is defined for a 2N x 2N domain. Equation (3.10) was found by assuming that $\Psi'_{D,N}(l,m)$ was zero at the extra points in the extended domain. In order to evaluate equation (4.2), the (in general non-zero) values of $\Psi(p,q,z_H)$ must be known at the extra points in the extended domain. However, in holography the hologram data is defined to be the N x N array $\Psi(p,q,z_H)$. Although N can be redefined so that the hologram data covers the (2N) x (2N) domain, it is almost certain that the data measured outside the N x N domain do not correspond to the ideal values compatible with the derivation of equation (4.2). Furthermore, one must consider the possibility that for some (μ,ν) the array element $g_{D,N}(z)$ may be zero; in the ideal case $DFT\{\Psi(p,q,z_H)\}_{\mu\nu}$ will also be zero and the quotient in equation (4.1) will be indeterminate. If $\Psi(p,q,z_H)$ is the data measured over the 2N x 2N domain it is very unlikely that $DFT\{\Psi(p,q,z_H)\}_{\mu\nu}$ will be exactly zero, so that its use in equation (4.1) may lead to serious computational errors. Thus for measured hologram data, equation (4.1) cannot be

used directly, and the source field reconstruction problem must be reformulated.

A.1. Restrictions on the input field

Another approach to the inverse scattering problem is to assume that both $\Psi_{D,N}(x,y)$ and $\Psi(x,y,z_H)$ are negligible for sufficiently large x and y. This is especially valid in Nearfield Acoustic Holography, where the hologram data is measured as closely as possible to the sources, which are assumed finite in size. The measured hologram data is assumed to comprise the N x N array $\Psi(p,q,z_H)$, for p,q = 0,1,...N-1. As already mentioned, equation (10) provides an exact deconvolution formula for infinite, continuous fields. This equation can be employed by approximating the infinite continuous Fourier Transform of the hologram field $\Psi(x,y,z_H)$. With the assumed finite extent of $\Psi(x,y,z_H)$ the DFT of the hologram data $\Psi(p,q,z_H)$ is a logical choice for such an approximation, but the DFT of a sampled field will differ from the continuous field transform. The nature of this difference must be considered, and the DFT results must be corrected.

A.2. Deviation of the DFT from the Fourier Transfrom

In appendix C it is shown that the DFT of a piecewise constant field deviates from its continuous transform as

$$\left| \frac{DFT[\Psi(x,y)]_{\mu\nu}}{\hat{\Psi}(k_{x\mu},k_{y\nu})} \right| = \left| \frac{k_{x\mu}\Delta \qquad k_{y\nu}\Delta}{4 \sin\left[k_{x\mu}\Delta/2\right] \sin\left[k_{y\nu}\Delta/2\right]} \right| \quad (4.3).$$

The field $\Psi(x,y,z_H)$, is assumed to be adequately represented by a piecewise constant field with the field value of each piece given by one corresponding hologram datum value. Equation (4.3) is therefore relevant, and it indicates that while the DFT of the hologram data will provide reasonable estimates of the transform field for small $k_{x\mu}$ and $k_{y\nu}$, it will overestimate the higher spatial frequency region.

Compounding any error introduced by the DFT or noise in the input data is the exponential growth of the reconstruction kernel $\hat{G}_{D,N}^{-1}(z)$ in equation (2.27) with spatial frequency and reconstruction distance. This problem suggests two things: First, some form of filtering in k-space will be necessary; and second, deconvolutions or source field reconstructions which include the evanescent wave information must be restricted to small z distances.

Undersamping in k-space is another source of error which may manifest itself if either $\hat{\Psi}(k_x,k_y,z_H)$ or

$\hat{G}^{-1}_{D,N}(k_x,k_y,z)$ varies rapidly over the DFT sampling intervals $\Delta k_{\mu x}$ and $\Delta k_{y\nu}$. Undersampling can be avoided by reducing the k-space sampling intervals. When using the FFT, this sample spacing is most easily reduced by augmenting the hologram data $\Psi(p,q,z_H)$ with zeroes in the same manner as in $\Psi_{D,N}(l,m)$ of equation (3.7) and performing the FFT of the $2N \times 2N$ zero augmented hologram array. This extended array is labeled $\Psi'(p,q,z_H)$ in analogy with $\Psi'_{D,N}(l,m)$.

A.3. A smoothing function

Based on the above considerations, equation (2.27) can be approximated as follows:

$$\Psi_{D,N}(l,m)=IDFT\{W(k_{x\mu},k_{y\nu}) \cdot DFT[\Psi'(p,q,z_H)] \cdot \hat{G}^{-1}_{D,N}(k_{x\mu},k_{y\nu},z_H)\}$$

$$(4.4)$$

where $W(k_{x\mu},k_{y\nu})$ is a suitable filter funtion and $\Psi'(p,q,z_H)$ is the hologram data augmented with zeroes. For the reconstructions presented later in this paper, the following filter function was used:

$$W(k_{x\mu},k_{y\nu})=\begin{cases} 1- \dfrac{e}{2}(k_r/k_c- 1)/\alpha & k_r \leqq k_c \\ \\ \dfrac{e}{2}(1 - k_r/k_c)/\alpha & k_r > k_c \end{cases} \quad (4.5)$$

where $k_r^2 = k_{x\mu}^2 + k_{y\nu}^2$ and k_r and α are adjustable parameters

of the filter. Experience has shown that a value of k_c

equal to 0.6 $(N\pi/L)$ and a value of α equal to 0.2 yield

consistently good results. In a particular experiment it

may be desirable to change these parameters, or possibly the

filter function's form, based on some a priori knowledge of

the source. However, any filtered source field reconstruc-

tions presented or compared in this work have been computed

with equation (4.5) and the filter parameters $k_c=0.6(N\pi/L)$

and $\alpha = 0.2$.

B. Reconstruction and inverse transformation test results

The suitability of the reciprocals of all six Green's

function forms as representatives of $\tilde{G}^{-1}(k_x,k_y,z)$ in

equation (4.4) was tested. The results are shown in the

charts of figures 4.1a and 4.1b for the case of determining

the pressure fields $p_{lm}^{(i)}(z_0=0.065\lambda)$ and z-component of

velocity fields $v_{lm}^{(i)}(z_0=0.065\lambda)$ using $p_{lm}^0(z=0.13\lambda)$ as the

input field. The integrated k-space form $g_{0,N}^{(6)}(z)$ is not

included in these charts as the errors produced using this

form are so large that scaling the figures to accommodate

them obscures any information about the other forms. The
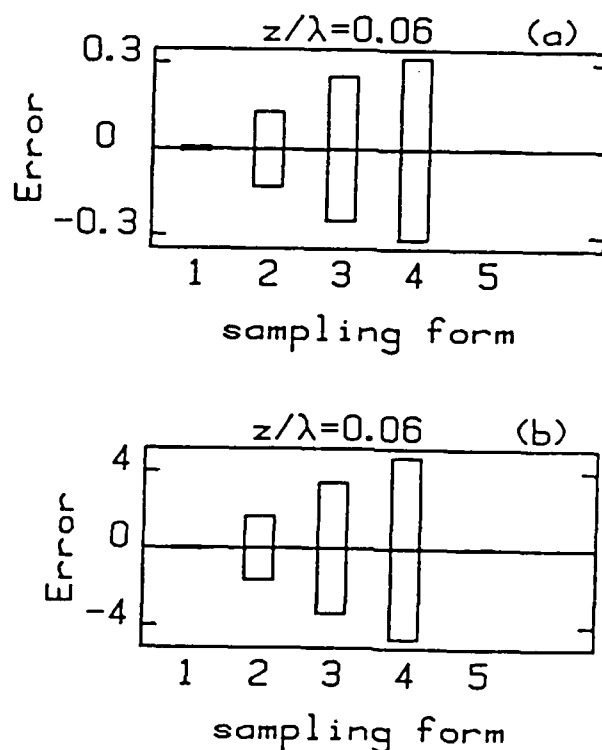
Fig. 4.1   The normalized error encountered with each method
in the source field reconstruction of (a)   the pressure
field 0.065 λ from the source from an input sample array of
the theoretical pressure field 0.13 λ from the source and
(b) the z-component of the particle velocity field 0.065 λ
from the source from the pressure field 0.13 λ from the
source.

sampled k-space Green's function $g_{0,N}^{(5)}(z)$ is the best

representative of $\hat{G}_{0,N}^{-1}(k_x, k_y, z)$ in all reconstruction cases

considered.

As discussed in section A., some form of filtering must
be included in the reconstruction process using DFT's. This
need for filtering, the form of the filter function, and its
effect on a numerical reconstruction are illustrated in
figure 4.2. The error from the high spatial frequency
approximation associated with the DFT and its amplification
by the reconstruction process is apparent if the DFT of an
unfiltered solution, $p_{lm}^{(5)}(z)$, is plotted with the DFT of

$p_{lm}^{0}(z)$. In figure 4.2a the crosses indicate the amplitude

of an unfiltered DFT of the pressure field $p_{lm}^{(5)}(z_0=0.065\lambda)$

as processed from the input pressure field $p_{lm}^{0}(z=0.13\lambda)$.

The solid line plots the DFT of $p_{lm}^{0}(z_0=0.065\lambda)$. The

difference between the two plots clearly grows for larger
magnitudes of spatial frequency. In real-space, this high
frequency error shows up as large oscillations of the
numerical solution about the actual solution. This behavior
is evident in in figure 4.2b which compares the unfiltered
$p_{lm}^{(5)}(z_0=0.065\lambda)$ with $p_{lm}^{0}(z_0=0.065\lambda)$. The numerical solution
is vastly improved by a multiplication with the filter
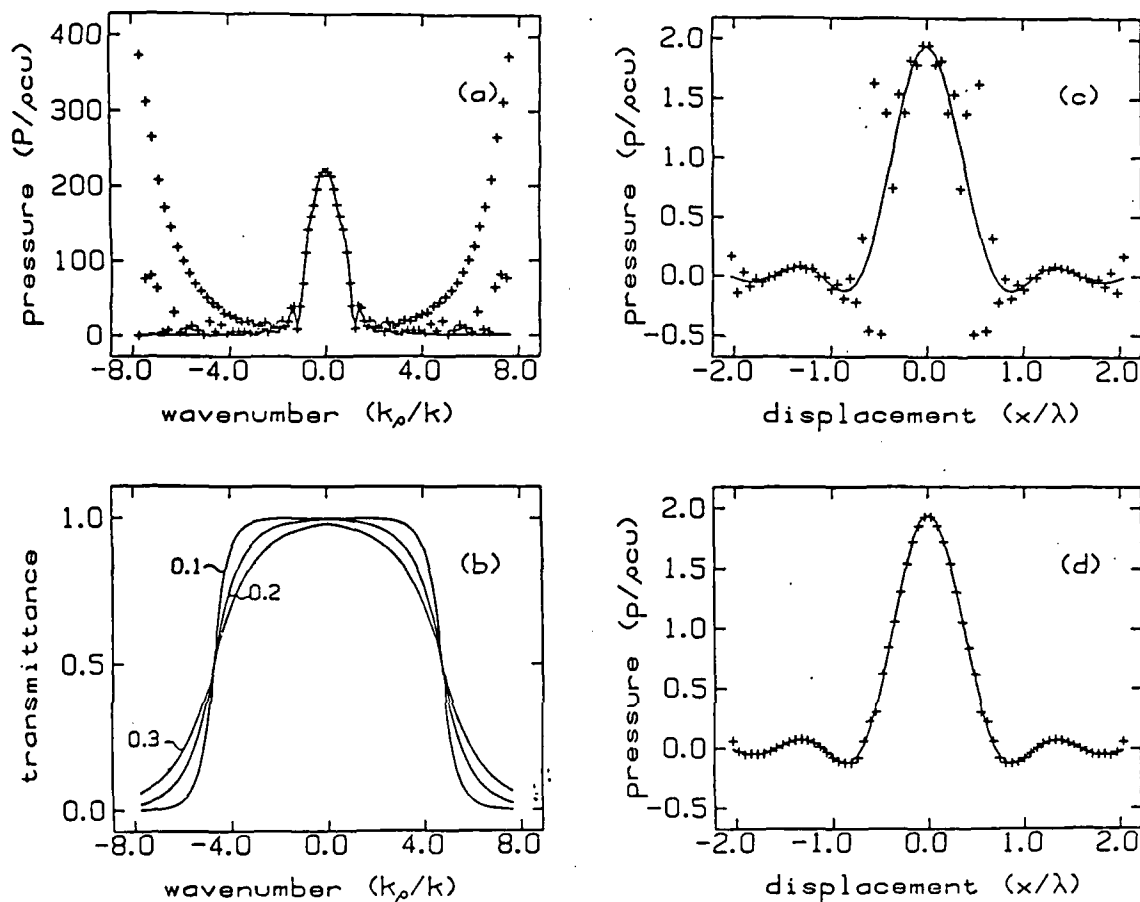
Fig. 4.2 (a) plus signs, amplitude of the DFT of a sample of the theoretical pressure field 0.13 λ from the source multiplied by the $[g_D^{(5)}(z)]^{-1}$ to reconstruct the pressure at the source. The solid line plots the theoretical values. (b) The unfiltered field against theory, (c) the filter function for three values of α, (d) the filtered output using the $\alpha = 0.2$ filter.

function, equation (4.5). This function is plotted in figure 4.2c for $k_c = 0.6\ N\pi/L$ and for three different values of α. Values of $k_c = 0.6\ N\pi/L$ and $\alpha = 0.2$ have been found empirically to give good results. These values are used in all filtered reconstructions in this study including those which provide data for figures 4.1a and 4.1b. Figure 4.2d shows the excellent fit of the filtered and actual solutions.

As further illustration of the capabilities of the sampled k-space Green's function with filtering, figure 4.3a shows a comparison plot of the real part of $v_{lm}^{(5)}(z_0 = 0.065\lambda)$, where the input field is $p_{lm}^0(z = 0.13\lambda)$, with $v_{lm}^0(z_0 = 0.065\lambda)$ plotted as the solid line; figure 4.3b shows the real part of $v_{lm}^{(5)}(z_0 = 0)$, where the input field is $p_{lm}^0(z = 0)$, against $v_{lm}^0(z_0 = 0)$. Both figures show good agreement between the numerical and actual solutions. These plots along with figures 4.1 and 4.2 indicate that accurate solutions to reconstruction and inverse transformation problems are attainable using the sampled k-space Green's function, $g_{D,N}^{(5)}(z)$, and the filter function of equation (4.5).

For reconstructions, the discussion of section A. and the test results presented in this section indicate that the reciprocal of the sampled k-space Green's function $g_{D,N}^{(5)}(z)$
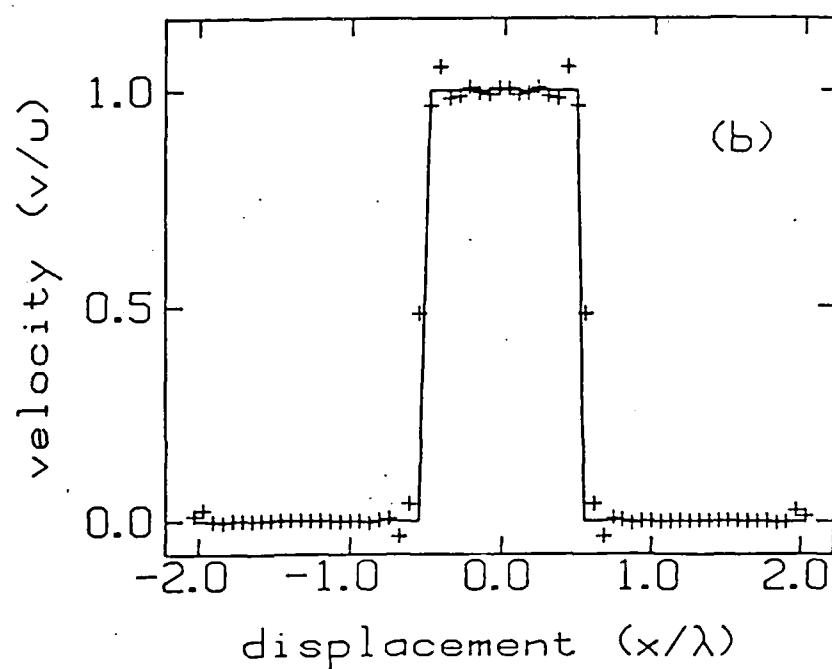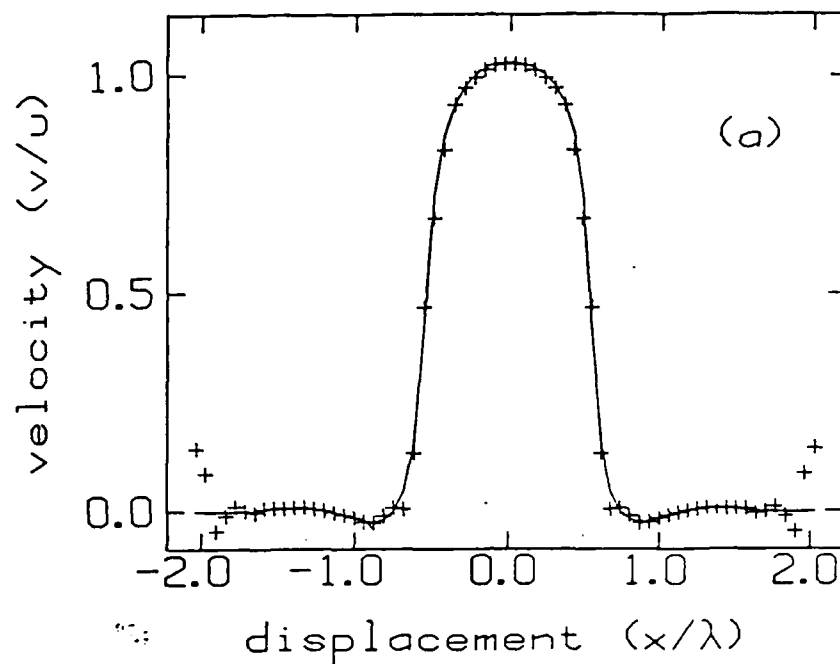
Fig. 4.3 (a) Real part of the reconstructed z-component of the particle velocity field at 0.06 λ from the source starting from the pressure 0.13 λ from the source. (b) Real part of the z-component of the particle velocity as reconstructed in the source plane from the input source plane pressure. The reciprocal of $g_N^{(5)}(z)$ with filtering was used in both, and in both, the solid line is theory.

with a spatial frequency filter is the best inverse propagator. The new sampling forms are of little use with this numerical source field reconstruction method.

C. Iterative deconvolution

For practical purposes, it is not likely that a direct inversion of equation (4.1) would ever be useful due to the typical size of the matrix involved, 4096x4096 in this work, and due to its nearly singular nature. The nearly singular nature of this matrix follows from the evanescent decay of high spatial frequency input fields $\Psi_{D,N}$ and the exponential enhancement of input fields Ψ_N with spatial frequencies near the propagating wavenumber; the matrix must display this decay and enhancement if it is to model wavefront propagation accurately. However, the fact that the matrix multiplication of equation (4.1) can be carried out quickly with the FFT suggests the search for an iterative deconvolution method requiring matrix multiplications and no matrix inversions.

C.1. Conjugate gradient descent method

The conjugate gradient descent method is an iterative method which may prove very useful for source field

reconstructions. The advantages of this method are its objective nature, no filter parameters, and its relative stability in comparison with the filtered solutions presented above. Luenberger[37] describes this method in terms of minimizing the functional

$$f(\vec{x}) = (\vec{x}|Q\vec{x}) - 2(\vec{b}|\vec{x}) \qquad (4.6),$$

where Q is a positive definite operator, and an inner product is represented by $(\vec{x}|\vec{y})$. The solution vector $\vec{x}_0 = Q^{-1}\vec{b}$ uniquely minimizes this functional. Before describing the iterative solution of this problem, the correspondence is indicated between $\vec{x}$, Q, and $\vec{b}$ and the acoustic items $\psi_{D,N}$, the Green's function matrix $[G_{D,N}(z_H)]$ of equation (4.1), and the hologram field $\psi(z_H)$.

The solution vector $\vec{x}_0$ is identified directly as the collection of values $\psi_{D,N}(l,m)$ representing the sought-after boundary condition. The positve definite operator Q can be identified as the Green's function matrix premultiplied by its conjugate transpose. The vector $\vec{b}$ can then be identified as the result of premultiplying the collection of values $\psi(p,q,z_H)$ by the conjugate transpose (indicated by the superscript dagger,†) of the Green's function matrix. The positive definite quality of this choice for the operator Q follows from the observations that the inner

product $(\vec{x}|Q\vec{x})=\vec{x}^{\dagger}Q\vec{x}$ is then the norm of a sample of values representing a radiating wavefront and is therefore positive, and the only bounded field which can be zero over a plane above the boundary is zero everywhere including the boundary. With the equation (4.30)'s components thus identified, it is clear that performing a source field reconstruction is equivalent to minimizing equation (4.6).

The basic idea of the conjugate gradient descent method is to move from each successive approximation, given by $\vec{x}_n$, of $\vec{x}_0$ in a direction which lies near to the negative gradient of equation (4.6), but which is also perpendicular to all previous changes. In terms of these successive approxima- tions $\vec{x}_n$ and mutually perpendicluar directions of change $\vec{p}_n$, equation (4.6) can be written as

$$f(\vec{x}_n) = f(\vec{x}_{n-1}+\gamma_n\vec{p}_n) \qquad (4.7).$$

The γ_n's are readily chosen to minimize the functional at each step, and it can be shown that the direction vectors $\vec{p}_n$ can be calculated recurrsively.[37] An efficient algorithm exists where $\vec{x}_n$ in theory converges to $\vec{x}_0$ in a finite number of steps, and the algorithm requires only one evaluation of the operator at each step.[38] The unique aspect of the application of this technique to source field reconstruc-
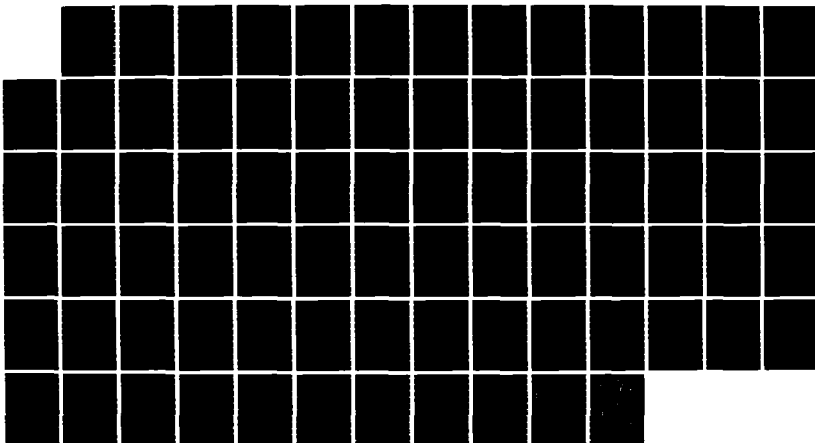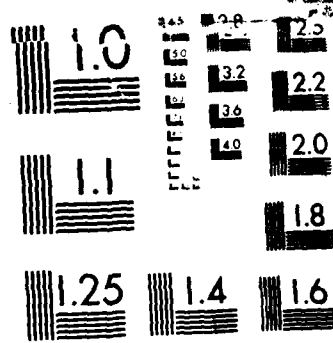
MICROCOPY RESOLUTION TEST CHART

tions, or deconvolution, is that the $N^2 \times N^2$ matrix Q needed never be formed. All matrix multiplications by Q can be carried out exactly by the discrete convolution algorithm presented in chapter III with the Green's functions $g_{D,N}^{(2)}$ or $g_{D,N}^{(4)}$.

C.2. Results from the implementation of this method

Although the conjugate gradient method converges in theory to the unique solution $\vec{x}_0$, it will not do so numerically due to roundoff error. However, it is reasonable to assume that only the highest non-radiating spatial frequency modes are missing from the non-unique numerical solution after a finite number of steps, and, therefore, it is not necessary to obtain the exact unique solution for most purposes. A practical solution is obtained by stopping the iterative process whenever the magnitude of the remainder $|Q\vec{x}_n - \vec{b}|$ falls below a chosen level.

The hidden-line plot in figure 4.4 is the smoothed reconstruction, by the method of section IV.A., of the real part of the normal component of velocity at the baffled piston source, $v_{lm}^{(5)}(z_0 = 0)$, from the pressure field 0.13λ

away, $p_{lm}^0(z=0.13\lambda)$. Figure 4.5 shows the reconstruction

obtained after 43 iterations by the techniques of this

section starting with the same input field $p_{lm}^0(z=0.13\lambda)$.

The standard deviation of the smoothed reconstruction from

the actual boundary field is more than five times that of

the iterative solution, and the average difference is nine

times that of the iterative solution.

Figure 4.6 shows the solution after 192 iterations.

The standard deviation of this solution from the actual

field has increased by 15% over that obtained after 43

iterations inspite of the fact that the magnitude of the

remainder $|Q\vec{x}_n-\vec{b}|$ has decreased by a factor of 10 from

$0.001|\vec{b}|$ to $0.0001|\vec{b}|$. The important point here is that

the first 40 iterations reduced the remainder by a factor

of 1000, while nearly five times as many iterations yielded

only a tenfold reduction and did not improve the solution.

This suggests that the iteration process may be objectively

stopped when it is observed that the magnitude of the

remainder is no longer decreasing rapdily.

The major disadvantage to this technique is the amount

of time required; nearly ten times as much total job time is

required to compute a solution by 40 iterations as is

required for a smoothed solution. The independence from
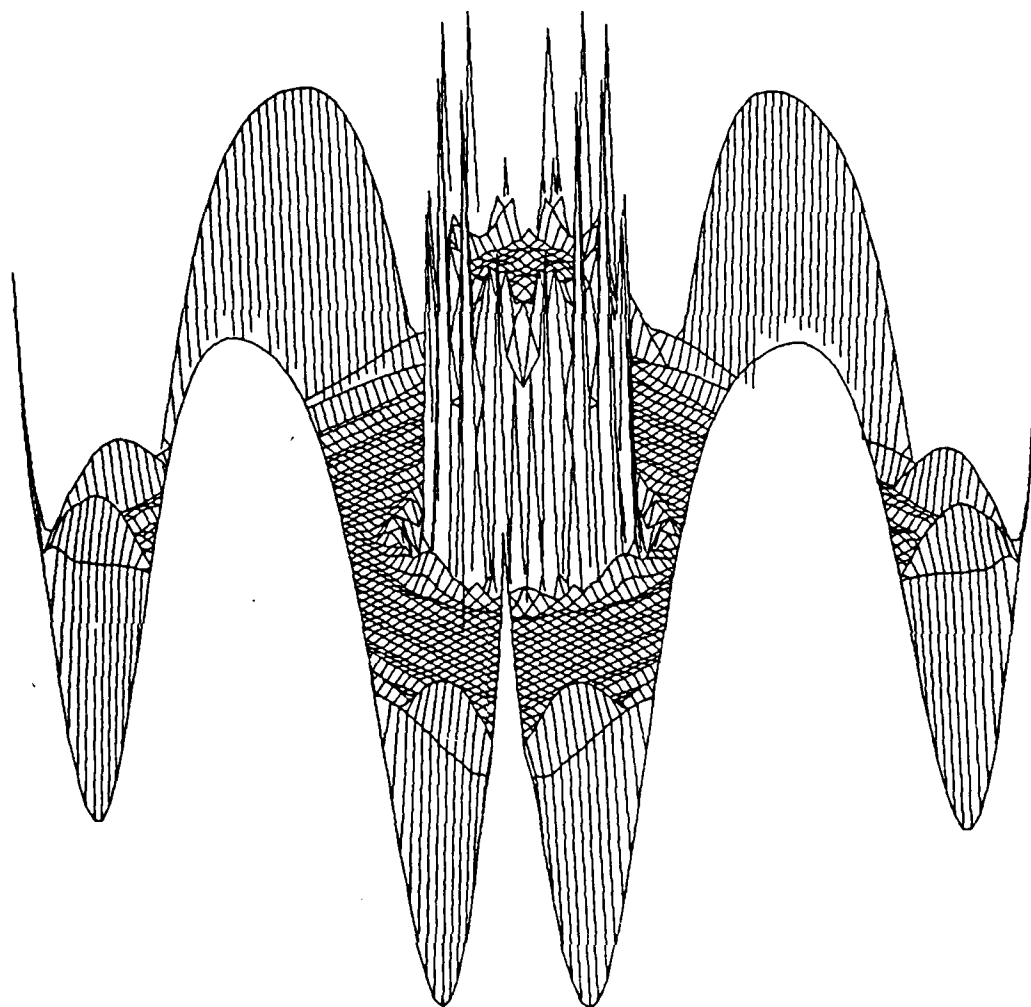
Fig. 4.4   A hidden-line plot of the smoothed reconstruction, by the method of section IV.A., of the real part of the normal component of velocity at the baffled piston source, $v_{\ell m}^{(5)}(z_0=0)$, from the pressure field 0.13λ away.
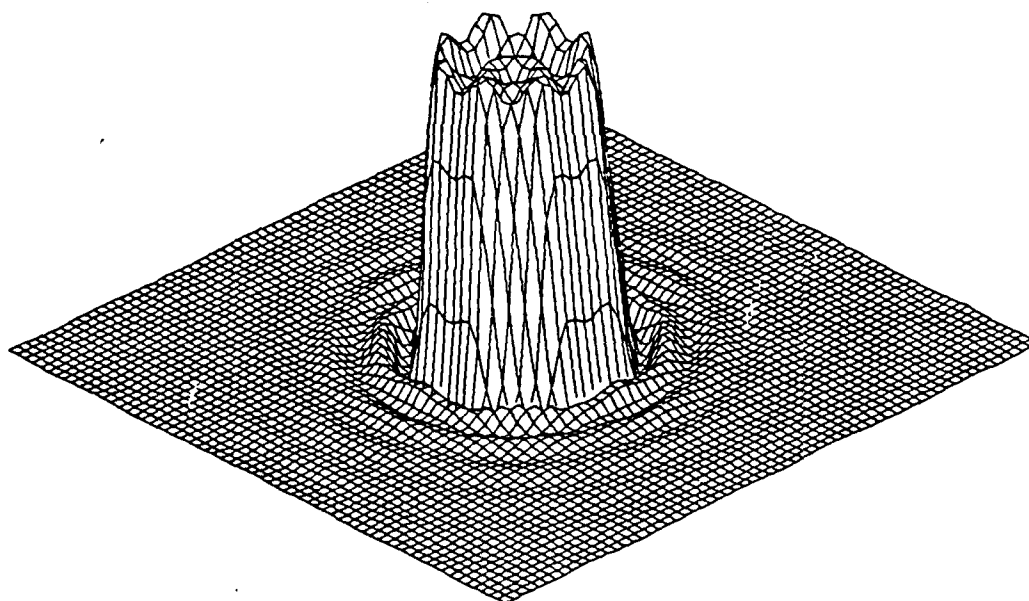
Fig. 4.5 The reconstruction obtained of the real part of
the normal velocity component at the baffled piston source,
$v_{lm}^{(5)}(z_0=0)$, from the pressure field 0.13λ away after 43
iterations by the techniques of section IV.C.
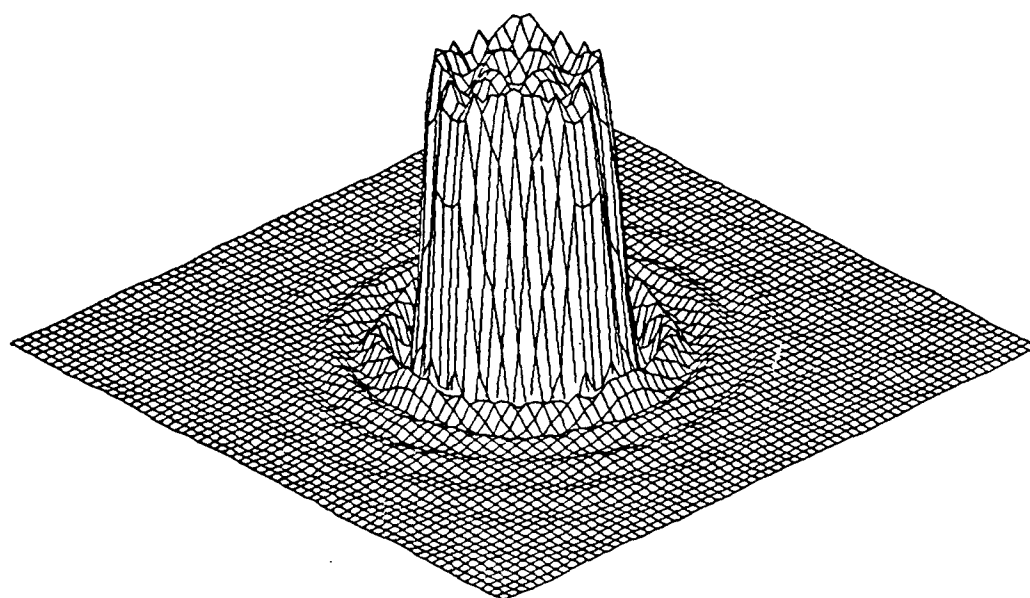
Fig. 4.6 The reconstruction obtained of the real part of the normal velocity component at the baffled piston source, $v_{\ell m}^{(5)}(z_0=0)$, from the pressure field 0.13λ away after 192 iterations by the techniques of section IV.C.

adjustable filter factors and the possibility of increased accuracy may warrant such an increase in computation time. Further, the actual computation time may be reduced by performing the calculations on an array processor and by improving the algorithm itself. The execution time of the iterative solution is likely to improve much more than the smoothed solution with the use of an array oriented machine since those sections which are least ammenable to array manipulation, intialization and input/output, are virtually identical in both cases and constitue the bulk of the latter. The basic algorithm[38] can be generalized so that each step requires only one matrix multiplication by $[G_{D,N}]$ and not the two matrix multiplications, $[G_{D,N}^{\dagger}]$ and $[G_{D,N}]$, represented by Q; this would cut the iteration time in half. The conjugate gradient descent method using the FFT to carry out discrete convolutions with the Green's functions $g_{D,N}^{(2)}$ and $g_{D,N}^{(4)}$, as described in chapter III, deserves further study in actual Nearfield Acoustic Holography experiments.

Chapter V.

SOLUTION OF THE SURFACE PROBLEM FOR ODD-SHAPED RADIATORS

In many practical acoustic problems with odd-shaped
radiating surfaces, the normal derivative of the field in
the form of the normal component of the surface velocity is
specified, and the pressure field over the surface is
sought. Forming a numerical solution to this problem is
also the first step in the reconstruction process covered in
chapter VI. Sections A and B of this chapter develop a
numerical solution for this problem and present the theory
behind this method. In section C, the non-trivial but
theoreticaly tractable spherical source boundary is
presented as a suitable test case for the techniques of this
chapter and the next.

A. Relating the surface velocity and pressure

For a radiating surface which does not correspond to a
level surface in a separable coordinate system of the
Helmholtz equation, there is no simple integral which yields
the field ψ in terms of either the Dirichlet boundary
condition ψ_s or the Neumann boundary condition $-i\frac{\partial \psi}{\partial n}$ alone
specified over the surface . With the requirement that the
field satisfy radiation conditions, the specification of

either Dirichlet or Neumann boundary conditions is

sufficient to determine ψ uniquely for any closed surface[39].

The Surface Helmholtz Integral Equation and the Interior

Helmholtz Integral Equation relate the two boundary

conditions accordingly. The use of these equations in

continuous form and in discrete approximation are discussed

in this section while their actual reduction to discrete

form is discussed in the next section. The last section of

this chapter will present test results for this method.

A.1. The Surface Helmholtz Integral Equation

In chapter II, the Surface Helmholtz Integral, equation

(2.19), was derived as a limiting case of the Helmholtz

Integral for the general field ψ. Written in terms of the

acoustic pressure field $p(\vec{r}_s)$ and the surface normal

component of particle velocity $v_n(\vec{r}_s)$, this equation is

$$\frac{p(\vec{r}_s)}{2} = \oint_{S-\epsilon^2} p(\vec{r}_s') \frac{\partial G}{\partial n}_f(\vec{r}_s-\vec{r}_s')dS - i\rho ck \oint_S v_n(\vec{r}_s') \; G_f(\vec{r}_s-\vec{r}_s')dS$$

$$(5.1).$$

The integrations in this equation must be replaced by

appropriate numerical integration approximations to solve

the general problem of odd-shaped radiators. At some point

in their application, most numerical integration schemes

reduce to matrix operations on a set of coefficients representing the known and unknown fields $v_n(\vec{r}_s)$ and $p(\vec{r}_s)$. Denoting these coefficient sets as $v_n(\vec{r}_s)_i$ and $p(\vec{r})_i$, the matrix approximation to equation (5.1) is

$$\frac{p(\vec{r}_s)}{2}_q = DS_{qj} \; p(\vec{r}_s)_j - MS_{qj} \; v_n(\vec{r}_s)_j \qquad (5.2),$$

with the Einstein summation convention in force. Equation (5.2) can be written as

$$\overline{DS}_{qj} \; p(\vec{r}_s)_j = MS_{qj} \; v_n(\vec{r})_j \qquad (5.3)$$

where $\overline{DS}_{qj} = \overline{DS}_{qj} - \frac{1}{2}I_{qj}$ and the matrices [D] and [M] are appropriate to the chosen numerical integration scheme.

At certain characteristic frequencies, equation (5.1) is not sufficient to determine a unique solution to the radiation problem.[30,39,40] The problem is that, at these frequencies, interior eigenmodes exist which are homogenous solutions over the surface under study . To any particular solution of the problem, it is then possible to add one or more homogeneous solution. This problem manifests itself as nearly singular matrices $[\overline{DS}]$ and [MS] in the approximation of equation (5.3).

A.2. The Interior Helmholtz Integral Equation

The homogeneous solutions of the Helmholtz equation are not radiating solutions, and it is necessary to incorporate the Interior Helmholtz Integral Equation, equation (2.18), with the surface equation to eliminate these solutions[30]. Written in terms of the acoustic pressure field $p(\vec{r}_s)$ and the surface normal component of particle velocity $v_n(\vec{r}_s)$, the Interior Helmholtz Integral Equation is

$$0 = \oint_S p(\vec{r}_s') \; \frac{\partial G}{\partial n} f(\vec{r}_I - \vec{r}_s') dS - i\rho ck \oint_S v_n(\vec{r}_s') \; G_f(\vec{r}_I - \vec{r}_s') dS \quad (5.4)$$

where the point $\vec{r}_I$ is interior to the surface. Equation (5.4) can be approximated by

$$DI_{qj} \; p(\vec{r}_s)_j \; = MI_{qj} \; v_n(\vec{r})_j \quad (5.5)$$

where the subscript q's refer to a number of points $\vec{r}_I$ in the interior. Equations (5.3) and (5.5) can be treated as an overdetermined system of equations and solved accordingly. In the literature,[30,40] a largely unanswered question is how to choose the interior points, as points which have nearly zero field with an interior eigenmode boundary solution must be avoided. The next section details the reduction of equation (5.1) to equation (5.2) and also introduces a

method for detecting characteristic frequencies and for
choosing interior points to avoid the problems caused by
these solutions.

B. Reduction to finite and discrete operations

The reduction of the surface problem to the matrix form
of equations (5.3) and (5.5) and their solution is presented
in three parts in this section.   The geometric represen-
tation of the surface as an assembly of flat triangular
plates along with the corresponding scheme for performing
the numerical integrations is presented first.   The
detection of characteristic frequencies for odd-shaped
radiators is covered next.   The formation of a surface
solution matrix is considered last.

B.1. Finite elements

The continuous surface of an odd-shaped radiator must
be represented by a generally simpler geometric surface
which can be specified by a finite number of parameters.
The method of representing the surface presented here is
essentially the method most recently described by Koopmann
and Benner.[40] The actual surface is replaced by a number
of interconnected flat triangular plates whose vertices lie

on the actual surface. The acoustic pressure and normal
component of particle velocity are considered constant over
each triangular element and equal to their respective values
at the center of each element. Since the elements are
flat, their normal directions are easily determined by
transforming the global set of coordinates in which the
problem is originally specified into new sets of coordinates
for each element. These local sets of coordinates are
defined by the three element vertices in such a way that the
local z-axis points in the local normal direction.

By approximating the surface and surface field with
these triangular elements, equation (5.1) can be
approximated as

$$\frac{p(\vec{r}_q)}{2} = \sum_{j \neq q} p(\vec{r}_j) \int_{\Delta_j} \frac{\partial G}{\partial z} f(\vec{r}_q - \vec{r}') \, dx' dy'$$

$$- i\rho ck \sum_j v_n(\vec{r}_j) \int_{\Delta_j} G_f(\vec{r}_q - \vec{r}') \, dx' dy' \quad (5.6)$$

where x, y, and z are the local coordinates for each
trianglular element j and the vectors $\vec{r}_q$ locate the center
of each triangle globally. The integrands are simply half
the Green's functions G_D and G_N encountered in chapters II,
III, and IV. The first integral for j=q yields zero
because the element is flat and the entire integral of

equation (5.1) omits a small region around the point $\vec{r}_q$; thus, integration of G_D over element q is omitted in equation (5.6).

By multiplying equation (5.6) by two, substituting G_D and G_N for the integrands, noting that integrating G_D over the entire element q yields one, and finally rearranging the integrals with respect to the equals sign, equation (5.6) can be written as

$$\sum_j p(\vec{r}_j) \int_{\Delta_j} G_D(\vec{r}_q - \vec{r}') dx'dy'$$

$$= i\rho ck \sum_j v_n(\vec{r}_j) \int_{\Delta_j} G_N(\vec{r}_q - \vec{r}') dx'dy' \quad (5.7).$$

The integrals are the same type as in equation (3.5) differing only in that the integration areas here are triangles as opposed to squares. The integrations may be approximated by expanding the Green's functions as is done in chapter III. The details of this expansion and the resulting quadrature formulae are presented in Appendix B. The matrix coefficients of equation (5.2) can then be identified as

$$\overline{DS}_{qj} = \int_{\Delta_j} G_D(x_q-x', y_q-y', z_q-z')dx'dy' \quad (5.8)$$

$$\text{and } MS_{qj} = \rho c k \int_{\Delta_j} G_N(x_q-x', y_q-y', z_q-z')dx'dy' \quad (5.9).$$

B.2. Characteristic frequencies

There is an inherent ambiguity when using the Surface
Helmholtz Integral Equation as to wether an interior or
exterior field is under consideration. For the interior
region, all of the boundaries are located at finite
distances; hence, the restriction to radiative solutions is
physically unnecessary. At characteristic frequencies,
radiating and non-radiating solutions exist. The Surface
Helmholtz Integral Equation is still valid at these
frequencies; however, since this equation must allow for
more than one solution, its numerical approximation with a
linear system of equations will be unstable under inversion.
An invertible system of equations is obtained by restricting
the solution to the single radiating solution by evaluating
the Interior Helmholtz Integral Equation at a number of
points in the interior. The difficulties that remain for an
odd-shaped surface are determining its characteristic
frequencies and choosing an appropriate set of interior

points if solutions at these frequencies are needed. In this section, a method for detecting these frequencies is presented and a suggestion on choosing the interior points is developed.

It is assumed that the surface equations can be adequately represented by a set of linear equations, as in equation (5.3), throughout the frequency region of interest. Therefore, if the continuous equation admits non-radiating homogeneous solutions, its numerical representation as a linear system of equations should admit these solutions as well. Exactly how these non-radiating interior solutions find their way into an exterior approximation formulation is intuiatively clear if the interior problem for the same surface is considered.

The monopole matrix [MS] of equation (5.3) for the interior problem differs from that for the exterior problem only by a minus sign for each element, while the dipole matrices [$\overline{DS}$] are identical. At characteristic frequencies, velocity eigenmodes exists for the interior which yield zero surface pressure by definition. The left-hand side of equation (5.3) is zero for such a mode and so reduces to

$$MS_{qj}^I \ v_n^0(\vec{r}_s) = -MS_{qj}^E \ v_n^0(\vec{r}_s) = 0, \ v_n^0(\vec{r}_s) \neq 0 \qquad (5.10),$$

where the superscripts I and E indicate the matrices of the interior and exterior problems and where the superscript 0 identifies the vector as representative of an eigenmode. If

equation (5.10) has a solution, then the equation

$$\overline{DS}_{qj}^{I} \, p^0(\vec{r}_s) = \overline{DS}_{qj}^{E} \, p^0(\vec{r}_s) = 0, \; p^0(\vec{r}_s) \neq 0 \qquad (5.11)$$

must have a solution $p^0(\vec{r}_s)$, which is the radiating solution

corresponding to $-v_n^0(\vec{r}_s)$. Equations (5.10) and (5.11) can

only be satisfied if the matrices [MS] and [$\overline{DS}$] are

singular[41]; that is,their determinants are zero. The

problem of determining the characteristic frequencies of an

odd-shaped surface is therefore equivalent to measuring the

relative singularity of the matrices as a function of

frequency.

According to Stewart,[41] the difficulty in determining

numerical singularities is that the matrices involved are

only approximations to the actual problem under study and so

may only be close to singular matrices when the real problem

is singular. Furthermore, many methods for decomposing a

matrix may transform a nearly singular matrix to a form

which is not nearly singular. However, the Singular Value

Decomposition yields a nearly singular matrix if and only if

the original matrix is nearly singular.[41] Therefore, this

decomposition is ideally suited for determining the

characteristic frequencies of an odd-shaped surface and the

eigenmodes as well. To show how this is possible, the

Singular Value Decompostion is examined.

By premultiplying and postmultiplying a general matrix by a set of unitary transformations, the Singular Value Decomposition reduces the matrix to diagonal form. By gathering these transfromations into the matrices [U] and [V†] (the dagger indicates the conjugate transpose), the general mxn matrix [X], where m$\geq$n, can be written as

$$[X] = [U]\begin{bmatrix}\Sigma\\0\end{bmatrix}[V^\dagger] \qquad (5.12),$$

where [U][U†]=[I], [V][V†]=[I], and [Σ] is an nxn diagonal matrix with diagonal elements δ_k, the so-called singular values.[43] It can be readily shown that the singular values measure the relative output vector magnitude for each of a complete set of input vectors, namely the columns of [V]. (For a hermitian matrix, the singular values are the eigenvalues, and the columns of [V] are the eigenvectors.)

In decomposing either [MS] or [$\overline{DS}$], this set covers all possible surface velocity or pressure distribution approximations. It is the low frequency, long wavelength regime which is of main interest in this work, and it is assumed that, if interior eigenmodes exist, they must be few in number relative to the number of degrees of freedom of the approximation scheme. Since all of the columns of [V] are orthogonal, eigenmodes, if they exist, must be represented by a distinct set of columns in [V] possessing correspondingly small singular values in comparison with the

singular values of the majority of other modes. Therefore, the presence of a very small singular value, relative to the remainder of values for a given matrix, indicates the existence of an interior eigenmode, at least in a numerical sense.

The lower characteristic frequencies of an odd-shaped surface enclosed volume can be found by forming and decomposing the matrices [MS] and [$\overline{DS}$] over a range of frequencies. In a plot of the calculated minimum singular value ratio as a function of frequency, these frequencies should be characterized by a pronounced dip in the plot. An example of this is presented in the last section of this chapter. Notice that only the singular values need be calculated for this process, and this can be done in much less time then is required for the complete decomposition as in the form of equation (5.12).

When a solution is required at an identified characteristic frequency, the formation of the matrix [V] of equation (5.12) is useful. Since a column q of [V] which is associated with a relatively small singular value δ_q is an eigenmode approximating vector, the suitability of a set of interior points, to be used in forming equation (5.5), can then be expected if the following conditions are met:

$$DI_{mn} \; p_q^0(\vec{r}_s)_n \gg 0 \quad \text{and} \quad MI_{mn} \; v_{nq}^0(\vec{r}_s)_n \gg 0 \quad (5.13),$$

where p_q^0 and v_{nq}^0 are all the qth columns of the [V] matrices

obtained in decomposing respectively $[\overline{DS}]$ and $[MS]$ such that

δ_q is very small. Equation (5.13) insures that the set of

chosen interior points, along with the Interior Helmholtz

Integral Equation, yield a system of equations which are not

satisfied by the non-radiating boundary conditions.

B.3. Formation of the surface solution matrix

The goal of this chapter is to form an invertible

matrix which relates the surface pressure and normal

component of surface velocity as follows:

$$p(\vec{r}_s)_q = GS_{qj} \, v_n(\vec{r}_s)_j \qquad (5.14).$$

At non-characteristic frequencies, the matrices of equation

(5.3) should be non-singular, and the matrix [GS] may be

formed directly as

$$GS_{qj} = \overline{DS}_{qn}^{-1} \, MS_{nj} \qquad (5.15).$$

At characteristic frequencies, the matrix must be

generated from the overdetermined system of equation (5.3)

and equation (5.5). The overdetermined system may be

written in the form of a single matrix equation as

$$\begin{bmatrix} \overline{DS} \\ -DI \end{bmatrix} [\, p(\vec{r}_s) \,] = \begin{bmatrix} MS \\ MI \end{bmatrix} [\, v_n(\vec{r}_s) \,] \qquad (5.16).$$

An equation with a single nxn matrix, where n is the number of degrees of freedom of the surface model, as in equation (5.14) may be obtained from equation (5.16) by utilizing the Singular Value Decomposition to form a generalized inverse of the left-hand side matrix in equation (5.16).[44] The decomposition has the following form:

$$\begin{bmatrix} \overline{DS} \\ -DI \end{bmatrix} = \begin{bmatrix} U_{11} & U_{12} \\ U_{21} & U_{22} \end{bmatrix} \begin{bmatrix} \Sigma \\ 0 \end{bmatrix} \begin{bmatrix} V^\dagger \end{bmatrix} \qquad (5.17).$$

The generalized inverse of this matrix is given by:

$$\begin{bmatrix} \overline{DS} \\ -DI \end{bmatrix}^{\sim 1} = \begin{bmatrix} V \end{bmatrix} \begin{bmatrix} \Sigma^{-1} & 0 \end{bmatrix} \begin{bmatrix} U_{11}^\dagger & U_{21}^\dagger \\ U_{12}^\dagger & U_{22}^\dagger \end{bmatrix} \qquad (5.18).$$

This equation reduces to the following form:

$$\begin{bmatrix} \overline{DS} \\ -DI \end{bmatrix}^{\sim 1} = \begin{bmatrix} V \end{bmatrix} \begin{bmatrix} \Sigma^{-1} \end{bmatrix} \begin{bmatrix} U_{11}^\dagger & U_{21}^\dagger \end{bmatrix} \qquad (5.19).$$

A similar decomposition and reduction can be performed on the right-hand side matrix in equation (5.16) yielding the following equation

$$\begin{bmatrix} MS \\ MI \end{bmatrix} = \begin{bmatrix} W_{11} \\ W_{21} \end{bmatrix} \begin{bmatrix} \Gamma \end{bmatrix} \begin{bmatrix} Z^\dagger \end{bmatrix} \qquad (5.20)$$

where $[\ \Gamma\ ]$ is a diagonal matrix and $\begin{bmatrix} W_{11} & W_{12} \\ W_{21} & W_{22} \end{bmatrix}$ and $[\ Z\ ]$

are unitary matrices. The matrix [GS] is then given by the expression

$$[\text{ GS }] = [\text{ V }][\text{ } \Sigma^{-1}][\text{ } U_{11}^{\dagger} \text{ } U_{21}^{\dagger} \text{ }] \begin{bmatrix} W_{11} \\ W_{21} \end{bmatrix} [\text{ } \Gamma \text{ }][\text{ } Z^{\dagger} \text{ }] \qquad (5.21).$$

C. Testing the techninque

To test the suitability of the techniques described in this chapter, and those to be described in the next chapter, a closed boundary for which non-trivial but theoretically tractable fields exists is desirable. As in so many problems in physics, the sphere is an ideal test case. Although the spherical coordinate system is one of the separable coordinate systems of the Helmholtz Equation, no advantage is taken of this symmetry in the techniques of this chapter or the next; thus, in this sense, the surface of a sphere may be taken as an odd-shaped surface. In this section the approximation of the surface is presented, and the characteristic frequencies predicted with this approximation by the technique of section V.B.2. are compared with those of a true spherical surface.

C.1. Approximating the spherical surface

The surface of the sphere is approximated in this work by a 60-faced polyhedron. Each of the faces are triangular, and the entire set is described by 32 vertex or nodal points which lie on a circumscribed sphere. These 32 nodal points are the 20 vertices of a dodecahedron plus 12 additional points obtained by radially projecting the center of each face of the dodecahedron onto the circumscribing sphere. Field values are calculated at the center point of each triangular face. These sixty points all lie on an inscribed sphere whose radius is 0.923 times that of the circumscribing sphere. This discrepancy must be accounted for in any comparison with theory for the sphere. The author was spared the task of calculating the cartesian coordinates of these nodal points and of determining which points describe each triangle through the efforts of an industrious undergraduate, Ray Sova, who researched this particular problem.[45] The polyhedron is pictured in figure 5.1. The edges of each adjacent triangle are separated for graphical purposes only.
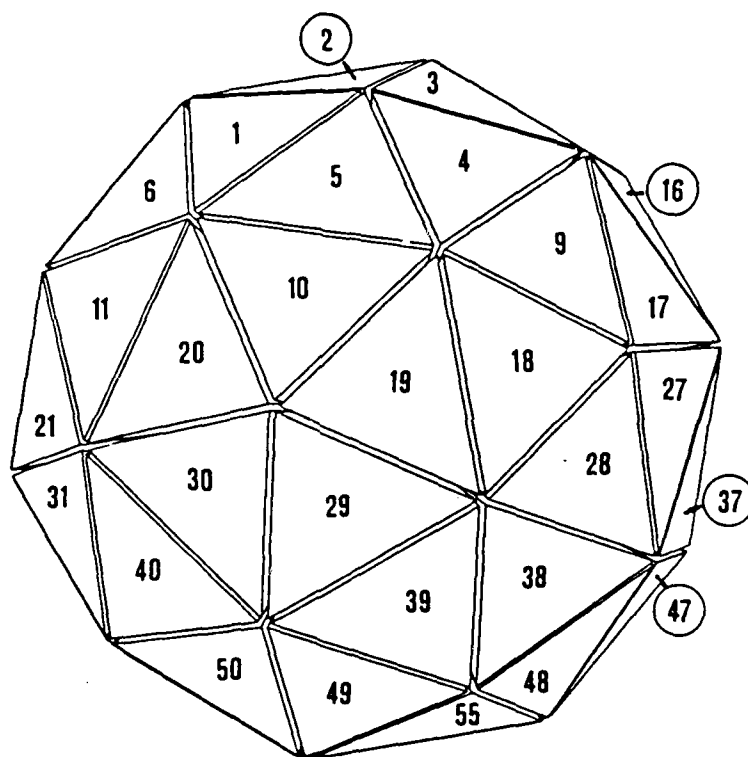
Fig. 5.1   The 60-sided polyhedron model of the sphere.

C.2. A comparison of theoretical and experimental values

for the characteristic frequencies of a sphere

The monopole and dipole surface matrices of equation

(5.3) where calculated for the polyhedral representation of

the sphere over a range of wavenumbers from near zero up to

twelve. In all cases the radius of the circumscribing sphere

was fixed at unity. The minimum singular value ratio of the

monopole matrix as a function of wavenumber is plotted in

figure 5.2.

The spherical Bessel functions are the solution to the

radial part of the Helmholtz Equation in spherical

coordinates for the interior problem.[46] Therefore,

eigenmodes or resonances occur whenever the frequency

normalized radius, ka, equals a zero[47] of a spherical bessel

function. The theoretical resonances or characteristic

frequencies for a sphere with radius equal to that of the

inscribed sphere of the polyhedron are indicated by the plot

border's outer tick marks.

The same type of plot is presented in figure (5.3) for

the minimum singular value ratio of the dipole matrix of

equation (5.3). Both plots show excellent agreement between

theory and calculation. As the frequency or wavenumber

increases, this agreement should break down as more complex
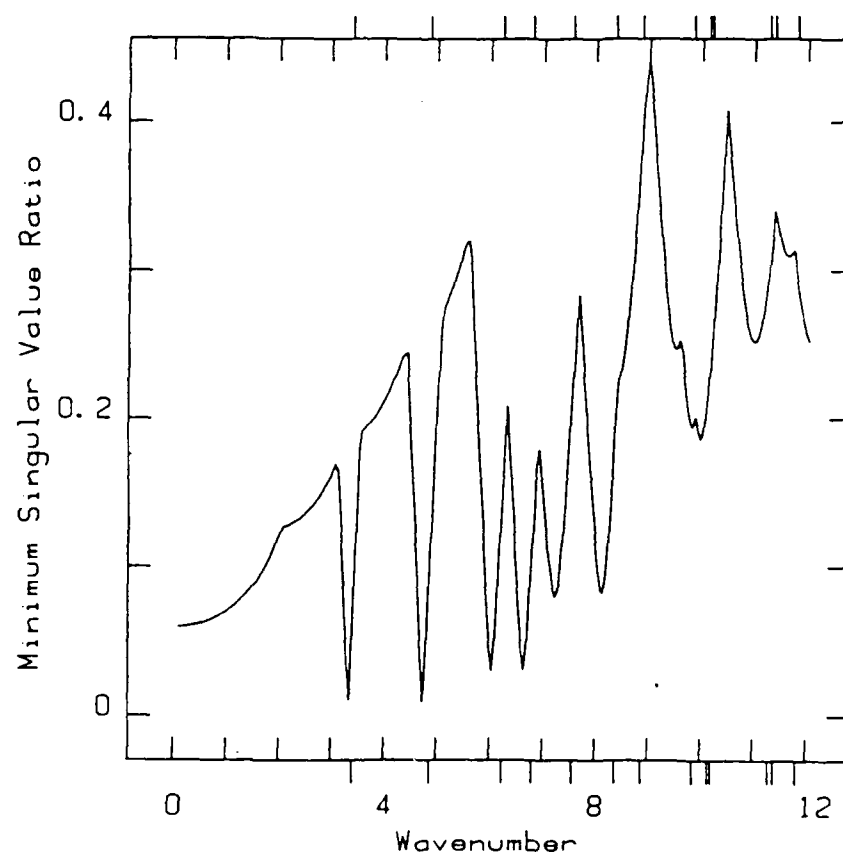
Fig. 5.2   Monopole matrix characteristic frequency curve
for the polyhedron model.
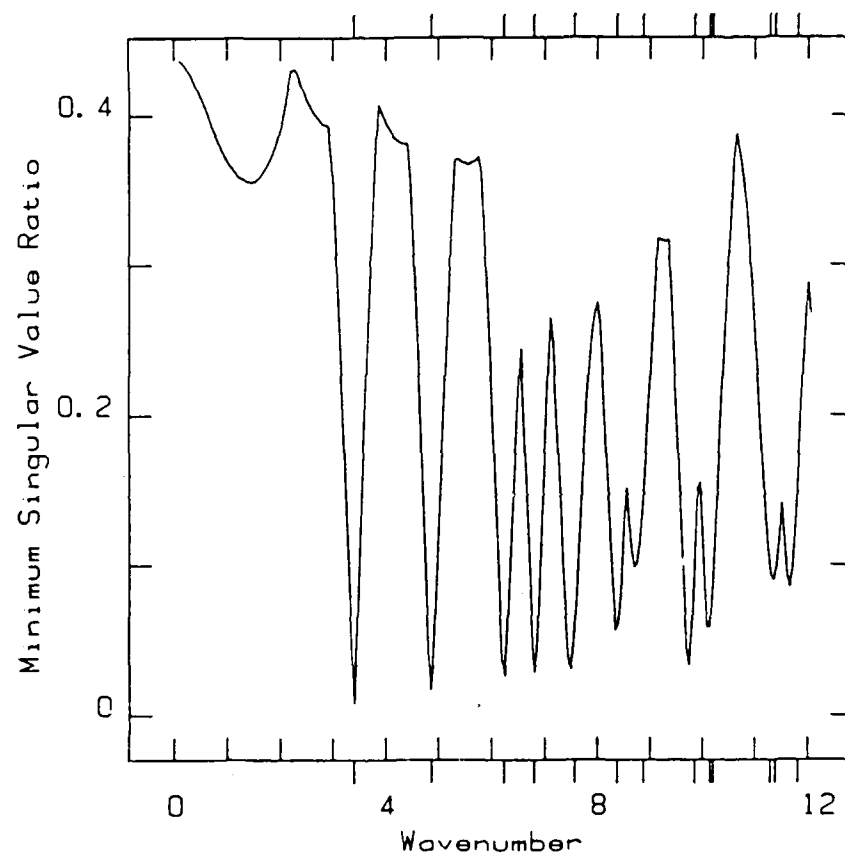
Fig. 5.3   Dipole matrix characteristic frequency curve
for the polyhedron model.

eigenmodes are possible. A conservative estimate of the useful range of the 60-sided polyhedron for representing the sphere is obtained by equating the shortest distance between two triangular element's centers with one half the minimum valid wavelength. This cutoff falls around a wavenumber of five.

To produce the data for the plots of figures (5.4) and (5.5), a number of interior points were used to eliminate the interior eigenmodes as possible solutions to the numerical formulation of the exterior problem. The singular values are those of the overdetermined system of equation (5.18). This correction was performed over the range between the dashed lines. The elimination of the numerical singularity is clear in these plots.
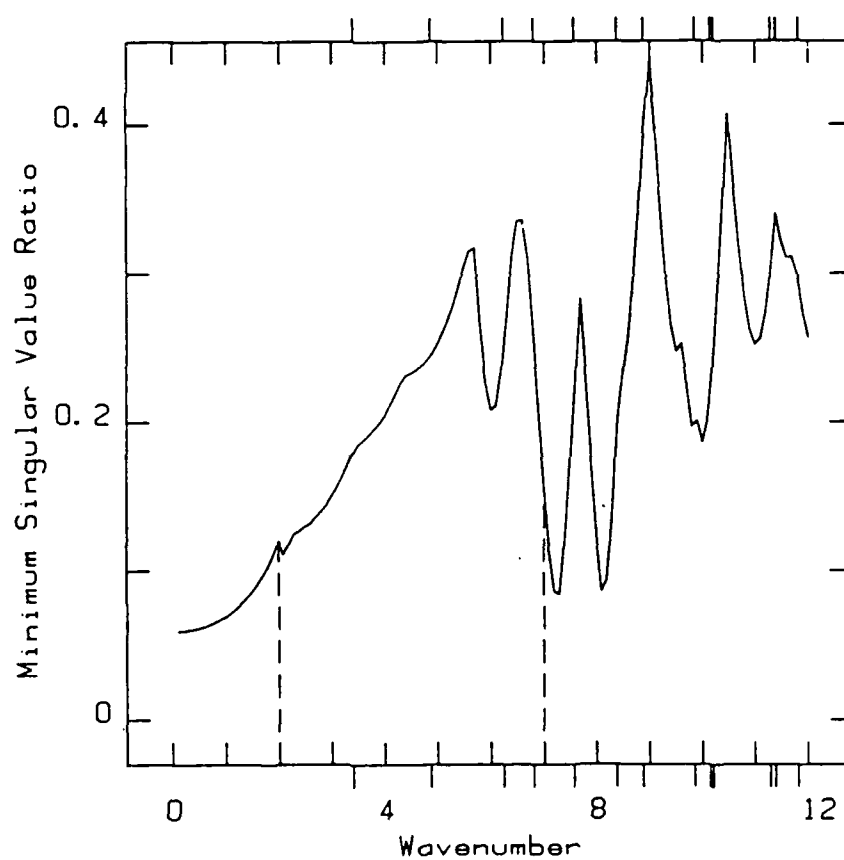
Fig. 5.4   Monopole matrix characteristic frequency curve for the augmented polyhedron model. (Augmented between dashed lines.)
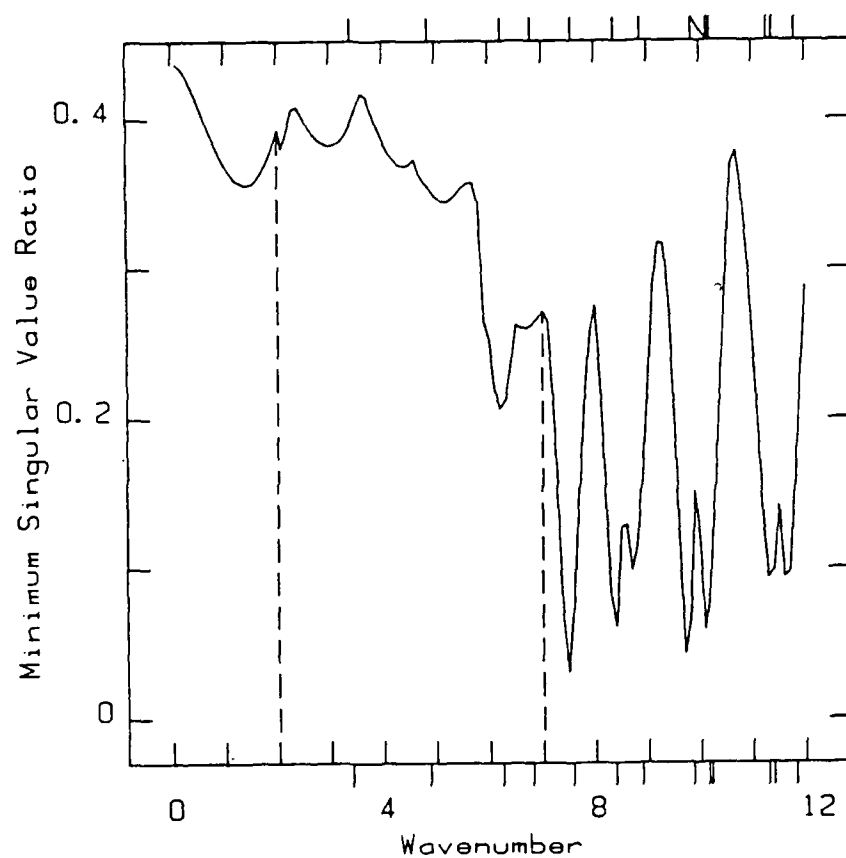
Fig. 5.5   Dipole matrix characteristic frequency curve for the augmented polyhedron model. (Augmented between dashed lines.)

Chapter VI.

RECONSTRUCTION OF ODD-SHAPED SOURCES

The extension of the techniques of Nearfield Acoustic
Holography to include the reconstruction of odd-shaped
sources is highly desireable for both theoretical and
practical applications. It is the aim of this chapter to
propose a numerical method for accomplishing this extension
and to present the results of simulation experiments which
support this proposal.

Generalized Holography in any separable coordinate
system of the Helmholtz Equation is based on the analytic
transformation of fields to and from an appropriate eigen-
space wherein wave propagation is performed by a simple
multiplication operator.[9] As is shown earlier, in the case
of planar holography, source field reconstruction is
accomplished by Fourier transforming the measured field and
then dividing the transformed field by the appropriate
Green's function of equation (2.25 or 2.26). In chapter IV
it was shown how this type of transformation approach is
highly desireable in reconstruction problems as experimental
or computational noise tends to be transformed to the high
order modes of the eigenspace and not to the lower modes.

Being an inversion process, source field reconstruction amplifies any data noise. By relagating the noise to higher order modes with an appropriate eigenspace transformation, a reconstruction of the lower order modes is possible.

An analytic transformation is not possible in the more general case of odd-shaped source boundaries. However, it is possible to generate and perform the appropriate trans-formations numerically. The Singular Value Decomposition plays a central role in this general reconstruction process much as the Fast Fourier Transform does in the case of planar holography. Since the Singular Value Decompostion operates on a matrix, its application requires the explicit development of the linear relationship between the normal component of surface velocity and the radiated field pressure and a reduction of this relationship to a finite matrix form.

A. Relating the surface velocity to the field pressure

For an odd-shaped radiator, reconstruction is defined as the determination of the normal component of the surface velocity at the source from a measurement of the radiated pressure field at a number of points above its surface. Experimentally, these measurements may be obtained with a planar array of microphones, or they may be obtained with a

more flexible microphone system at a number of points surrounding the surface. A general method for forming a matrix relating the surface velocity to the radiated pressure measured at these microphones is a fundamental requirement of the reconstruction process. To lay the groundwork for such a method, the continuous integral relationships between the normal component of surface velocity and the radiated pressure in the field are examined in this section.

A.1 The Helmholz Integral

The Helmholz Integral, equation (2.17), can be written in terms of the acoustic pressure field and the particle velocity field as:

$$p(\vec{r}_f)=\oint_S p(\vec{r}_s') \; \frac{\partial G_f}{\partial n}(\vec{r}_f-\vec{r}_s')dS \; - \; i\rho ck\oint_S v_n(\vec{r}_s') \; G_f(\vec{r}_f-\vec{r}_s')dS \tag{6.1}$$

This expression relates the acoustic pressure at a point $\vec{r}_f$ in the field above the surface S to the surface pressure and the sought-after normal component of surface velocity. The Surface Helmholz Integral Equation (5.1) and the Interior Helmholtz Integral Equation (5.4) provide the link between the surface pressure and velocity as discussed in the previous chapter. Together, equations (5.1), (5.4), and

(6.1) uniquely determine the pressure in the field in terms of the normal component of surface velocity.

A.2 Experimental uniqueness problems

In the last chapter, a fundemental uniqueness problem was encountered with the use of the Surface Helmholtz Integral Equation due to the presence of homogeneous solutions of an interior problem closely related to the exterior radiation problem under study. It is assumed that the techniques of the last chapter are sufficient to overcome this problem. With the use of equation (6.1) in this chapter however, a different source of non-uniqueness is encountered; this non-uniqueness can be viewed as more experimental in nature than the unavoidable problem with charateristic frequencies encountered in the last chapter.

Given the normal component of surface velocity for the odd-shaped source and the Surface and Interior Helmholtz Integral Equations, a unique surface pressure field is determined. These two surface fields in turn define a unique pressure field above the surface by way of equation (6.1). However, this radiated pressure field can only be observed experimentally over a limited region and with finite resolution. In analogy with the theory of planar holography, it is intuitive that spatial frequency modes of

an odd-shaped surface must generate evanescent fields when
their wavenumber exceeds that of the propagating wavenumber.
The information about these modes is diminished at the field
measurement loci relative to the information from lower
frequency radiating modes. If the evanescent field of one
mode falls below the dynamic range of the measuring system
relative to a second mode, surface modes with or without
this evanescent mode will appear experimentally identical.
Numerically this problem manifests itself as a singular
system of linear equations. A reconstruction solution to
this problem is possible, but it requires special treatment
of all information about these modes.

B. Finite and discrete operations

The numerical reconstruction problem can be broken down
into two parts. First, a single matrix is formed relating
the finite set of numbers $v_n(\vec{r}_s)_j$, which represent the
normal component of surface velocity, to a measured set of
field pressure values $p(\vec{r}_f)_q$. And second, a minimal solution
to this matrix problem is determined. These two problems are
considered in this section.

B.1 Formation of the field matrix

In order to reduce the size of the numerical odd-shaped surface reconstruction problem, it is desireable to form a single matrix which directly relates the normal component of surface velocity to the pressure at a number of points in the field above the surface. This matrix is refered to as the field matrix [GF], and with it the following equation can be written:

$$p(\vec{r}_f)_q = GF_{qj} \; v_n(\vec{r}_s)_j \qquad (6.2).$$

As already discussed above, there is no single integral relating the surface velocity and field pressure, although the pressure is uniquely determined by the system of equations (5.1), (5.4), and (6.1). The reduction of equation (5.1) and (5.4) to finite form was covered in the last chapter, and the same methods used there can be applied to the reduction of equation (6.1) to a finite and discrete form. By treating the odd-shaped surface as constructed of a number of edge-connected flat triangular elements, each with constant surface pressure and velocity, as in chapter V, equation (6.1) can be approximated by the following equation:

$$p(\vec{r}_f)_q = DF_{qj} \; p(\vec{r}_s)_j + MF_{qj} \; v_n(\vec{r}_s)_j \qquad (6.3),$$

where the matrix coefficients can be identified as

$$DF_{qj} = \frac{1}{2} \int_{\Delta_j} G_D(x_q-x',y_q-y',z_q-z')dx'dy' \qquad (6.4)$$

and $\qquad MF_{qj} = \frac{-\rho ck}{2} \int_{\Delta_j} G_N(x_q-x',y_q-y',z_q-z')dx'dy' \qquad (6.5).$

These integrals differ by the simple constant factors of plus and minus one-half from the integrals of equations (5.8) and (5.9) respectively. Their numerical evaluation is presented in appendix B.

By using the surface solution matrix [GS] of equation (5.21), the surface pressure vector $p(\vec{r}_s)_j$ can be written in terms of the surface velocity. With this replacement, equation (6.3) can be written as

$$p(\vec{r}_f)_q = (DF_{qn} GS_{nj} + MF_{qj}) v_n(\vec{r}_s)_j \qquad (6.6),$$

and the elements of [GF] can be identified as

$$GF_{qj} = (DF_{qn} GS_{nj} + MF_{qj}) \qquad (6.7).$$

Equation (6.7) provides the formula for constructing the elements of [GF] from a set of readily calculated coefficients for any odd-shaped geometry.

B.2 Solution with the Singular Value Decomposition

The generalized inverse of a matrix is defined in equation (5.18) of chapter V in terms of the matrix's

Singular Value Decomposition. The generalized concept of an inverse is needed in chapter V inorder to obtain a single nxn matrix relating the surface velocity and surface pressure from the mxn, m>n, overdetermined system of equations (5.3) and (5.5), where n is the number of degrees of freedom for the surface model, and m-n is the number of interior points. In this chapter, the Singular Value Decomposition is used in a similar way, but it is not necessary to actually form the generalized inverse of the field matrix [GF] as is necessary for [GS] in chapter V. It is interesting and instructive to clarify these ideas by comparing the numerical process of wavefront propagation and source field reconstruction for an odd-shaped source with the analytic process for a source with a level surface in a separable coordinate system.

For the odd-shaped source problem, the surface is represented by a model with n degrees of freedom and the field above the surface is sampled at m points where m is generally larger than n. The mxn matrix [GF] then has a decomposition with the same form as equation (5.17), that is

$$[\ GF \ ] = \begin{bmatrix} U_{11} & U_{12} \\ U_{21} & U_{22} \end{bmatrix} \begin{bmatrix} \Sigma \\ 0 \end{bmatrix} [\ V^{\dagger} \ ] \qquad (6.8).$$

The matrix [GF] is the operator which produces the pressure at a number of field points when it acts on a sample of the

odd-shaped surface's normal component of velocity. For comparison, the corresponding operator G for the case of an infinite, continuous planar source can be written as

$$G = \mathcal{F}^{-1}(\hat{G}_N \cdot \mathcal{F}) \qquad (6.9)$$

where $\mathcal{F}$ is the 2-D Fourier transform and $\hat{G}_N$ is the Fourier transformed Green's function for planar Neumann boundary conditions as discussed previously. The analogy between the continuous and numerical processes can be seen readily: The matrix $[V^{\dagger}]$ corresponds to the Fourier transform, the diagonal matrix $[\Sigma]$ takes the place of the multiplication by the Green's function, and the matrix $[U]$ corresponds to the Inverse Fourier transform. Notice that since there are only n degrees of freedom in the odd-shaped surface model, there can only be n unique ouput fields from equation (6.8), and these fields are spanned by the first n columns of the unitary matrix $[U]$. A similar situation could arise in the continuous case if the boundary condition was known only up to a certain cutoff spatial frequency. The propagated field would then be limited to the same spatial frequency range.

The reconstruction of a source plane field in the continuous case requires the application of the inverse of the operator G. This operation consists of performing the Fourier transform of the pressure in a plane above the source, dividing the transformed field by the Green's

function, and performing the inverse Fourier transfrom on
the resulting field. If information about the source is
needed only up to a finite spatial frequency, then the
components of higher spatial frequencies produced by the
forward transform are ignored. Numerical reconstruction of
an odd-shaped source as given by the generalized inverse
of the matrix [GF] follows the same pattern. The pressure
field sample vector is decomposed into a superposition of
the columns of the unitary matrix [U] by multiplication with
the conjugate transpose of [U]. The first n components are
divided by the corresponding singular values of [Σ] while
the remaining m-n components are discarded, and the
resulting superposition of the columns of [V] is calculated.

B.3 Calculating the solution in the presence of noise

The preceding discusion considers reconstruction when
all quantities are known exactly in contrast with the noisy
data present in experiment. This noise results from the
limitations on experimental measurement and from the
discrete approximation of continuous operations used to
process the data. Planar source fields are reconstructed
using the DFT of a finite sample of the field above the
source as explained in chapter IV. In this case it was shown
that the as the spatial frequency approximated by the DFT

grows higher, the noise level grows higher, and the reciprocal of the Green's function needed in the reconstruction process also grows. Both these factors enhance the noise in the reconstruction. The same type of problem can be expected in any reconstruction problem, and methods for avoiding the problems with noise and an understanding of the effects of any reduction method on the solution are necessities.

The general approach to producing a reasonable solution in the presence of noise is to eliminate or reduce the contribution to the solution from the calculated components of higher spatial frequency modes. The relative magnitude of the Green's function or singular values provides a guide in the noise reduction process. The use of a filter function was discussed in chapter VI for planar reconstructions and a similar approach is suggested in the Geophysics literature for inversion problems using the Singular Value Decomposition, but no clear guidelines are provided.[48] A simple cutoff of any components associated with a singular value below a chosen minimum value is another approach, and a scheme for determining where to set the cutoff based on the relative size of the singular values and the calculated component size is presented in the Numerical Mathematics literature.[49] The users guide[43] to the Singular Value Decomposition program used in this work maintains that, just

how to handle these small singular values, is still a problem open to investigation, and future research in this area would be valuable to a number of disciplines. Due to the relatively small size of the problem studied here (i.e. sixty degrees of freedom) a much simpler approach is practical.

The approach used to generate the reconstructions in this work is to watch the reconstructions develop as higher and higher order reconstructed surfaces modes are super-imposed. The process is halted and reversed one step when the solution takes on a noisy appearance. Research into reducing the subjectivity of this step would be desireable. However, notice that the same cutoff (or no cutoff at all) is used in the reconstructions presented in the final section of this chapter. This suggests some level of consistency from experiment to experiment. Furthermore, notice that the lower order modes are not effected by this method, and these are the modes which radiate most efficiently. In many applications, these lower order modes will be of primary interest, and the neglect of tenuous information about the highest order modes will be inconsequential.

C. Calculating the theoretical field of a test-case

The techniques of this chapter were tested in a number of simulated odd-shaped source reconstructions. A spherical source boundary is represented in these simulations by the sixty-sided polyhedron described in the last chapter. A simulation experiment consists of generating the theoretical pressure at a number of points above the odd-shaped surface, thus forming a theoretical hologram, and then reconstructing the surface field from this hologram using the techniques described above. In this section an appropriate boundary condition and a method of calculating the field produced by this boundary are presented.

C.1. A small piston set in a rigid sphere

A small piston set in an otherwise rigid sphere was chosen as the test case boundary condition, because it provides a good test of the resolving capabilities of the reconstruction technique, and the field produced by such a boundary is relatively easily calculated. The actual boundary condition used for a sphere with radius a expressed in spherical coordinates is

$$v_n(a,\theta,\phi) = \begin{cases} u_0 & \text{when } 0 \leq \theta \leq \theta_0 \\ 0 & \text{otherwise} \end{cases} \qquad (6.10).$$

The coordinate system is chosen to eliminate any dependence on the angle ϕ.

The angle θ_0 is chosen so that the active area of the boundary is equal to the area of one triangular element in the surface approximation model. This area is one-sixtieth of the total sphere's surface. Simple calculation shows that angle θ_0 satisfies the following equation:

$$\cos(\theta_0) = 1 - 1/30 \qquad (6.11).$$

For this small angle, the enclosed surface deviates very little from a flat surface, and it is thus reasonable to refer to this boundary section as a small piston.

C.2 Calculating the field

The pressure at any point outside the rigid sphere with a small piston is given by the infinite summation:[50]

$$p(\vec{r}_f) = p(r_f, \theta, \phi) =$$

$$\frac{i\rho c u_0}{2} \sum_{m=0}^{\infty} \{P_{m-1}[\cos(\theta_0)] - P_{m+1}[\cos(\theta_0)]\} \, P_m[\cos(\theta)] \, \frac{h_m(kr)}{h_m'(ka)}$$

$$(6.12)$$

where the P_m's are the Legendre polynomials, the h_m's are the spherical Hankel functions, and the prime indicates the derivative with respect to argument. The recurrence relations for these polynomials make them fast and easy to

tabulate numerically. The series also converges rapidly and is approximated in this work by the first ten terms.

D. Results from the test case

In this section the results of simulated reconstruc-tions of the piston set in a rigid sphere are presented. The wavenumber in these simulations is 4.85 corresponding to a characteristic frequency of the sixty-sided polyhedron model, and therefore, the techniques of chapter V are required to form a surface solution matrix from the over-determined system of equations (5.3) and (5.5). A set of sixty interior points radially aligned with the surface element centers but half the distance from the sphere's center were used to generate an overdetermined system of equations using the Interior Helmholtz Equation.

Two different hologram geometries were simulated: measurements taken on a planar grid of 25x25 microphones spaced symmetrically 0.4λ apart in a plane 0.23λ above the sphere; and measurements taken at 60 microphones each located 0.23λ radially above the center of a surface model element. Note that, due to the numerical integration scheme for determining the field matrix coefficients, it is best not to bring the field points too close to the surface elements. A separation from any element to any microphone

of half the smallest distance between element centers should
be adequate; the distance between surface element centers is
0.48λ in the simulations presented below.

D.1 Displaying the reconstructed odd-shaped surface fields

Holographic reconstructions generate large quantities
of information which must be displayed graphically to be
useful. Planar reconstruction field quantities are readily
displayed by conventional 3-D hidden-line plots of the field
variable over the 2-D plane, whereas odd-shaped source
reconstructions present a more general graphic display
problem. Novel graphics routines were developed to handle
this problem.

The technique for diplaying the reconstructed
odd-shaped surface fields is carried out in two steps.
First, enough imaginary cuts are made in the triangle-faced
polyhedron model of the odd-shaped surface so that it can be
flattened out into a plane figure. The shape of each surface
element triangle can be preserved in this process provided
the original surface is convex. With this process, some
elements of a surface which is not strictly convex would
have to be distorted, and, to avoid this distortion, it
might be preferable to process and display sections of such
surfaces separately. A flattened projection of the sixty

sided polyhedron used in this study is presented in figure 6.1. The element numbering scheme is the same as used in figure 5.1 for the unprojected surface.

Once a projection of this type has been achieved, a field variable can be displayed by constructing a five-faced prism over each triangle where the base and top of the prism are identical triangles and the height of each prism is determined by the field variable. A 2-D projection of the resulting set of prisms can then be generated.[51] This projection will display the field variables over all the elements in a single figure which conveys some idea about their spatial distribution as well. The remaining figures of this chapter serve as examples of this projection scheme.

D.2 Reconstruction from a planar hologram surface

Reconstructing an odd-shaped source from field pressure measurements over a planar array of microphones is of special interest as the Nearfield Acoustic Holography Group at the Pennsylvania State University possesses such a measurement system. More generally, reconstructions of this type would be experimentally advantageous because a fixed microphone array allows for very high speed data acquisition as compared with a scanning microphone system.[13]
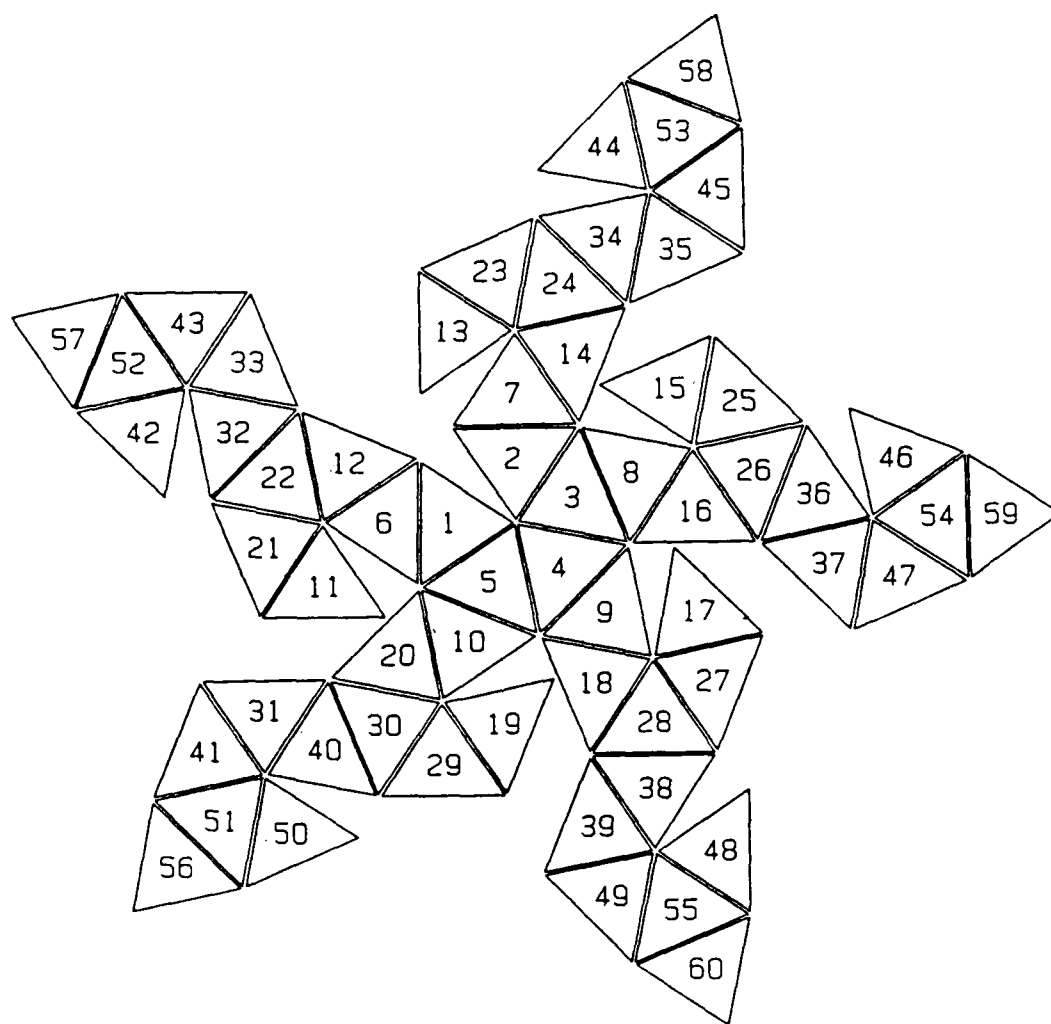
Fig. 6.1   A flat projection of the 60-faced polyhedron.

The normal component of intensity is an ideal quantity to display, as it incorporates the normal component of velocity and the pressure, and it requires the proper determination of phase between the pressure and velocity. Note that, for comparison purposes, the normal component of intensity of a small piston in a rigid sphere is zero everywhere off the piston and nearly constant over the piston.

The sixty sided polyhedron is too coarse of a model to supply detailed quanitative information about the small piston source, but the following figures demonstrate that it can be used to determine the location of the source quite well, and the intensity values produced are all within 3dB of the theoretical value at the piston's center.

It is to be expected that reconstructions of small features will be more difficult the further these features are from the measuring system. To address this expectation, a series of normal component of intensity reconstructions is presented in which the theoretical piston is located progressively further from the hologram plane.

Figure 6.2 is a 3-D projection of the normal component of intensity reconstruction from the theoretical pressure field of a single piston centered on surface element number 1 [see figure 6.1 or 5.1]. The location of the piston source is clearly indicated. A small false

source appears at element 59 which is on the opposite side of the sphere from the true source, however this source falls below 7% the strength of the true source. The actual intensity value reconstructed at element 1 is 11% below the theoretical central value. For this reconstruction, out of the sixty surface modes representable by the surface model, the modes associated with the fifty largest singular values in the decomposition of the field matrix, equation (6.8), were used. This holds true for the next three reconstructions presented as well.

Figure 6.3 displays the reconstructed normal component of intensity for a piston source centered on surface element 20. A false source appears at element 53 which is adjacent to the diametrically opposite element of element 20. This source is 11% the strength of the maximum reconstructed source strength. The reconstructed source at element 20 is 20% below the theoretical central value.

Figure 6.4 displays the reconstructed normal component of intensity for a piston centered on on surface element 56 which is one of the furthest elements from the hologram plane, and it faces away from the array. There are several small false sources in the 10% strength range, and the reconstruction of the true source is 46% the central theoretical value. However, the existence of a small localized source at this position is still quite clear.
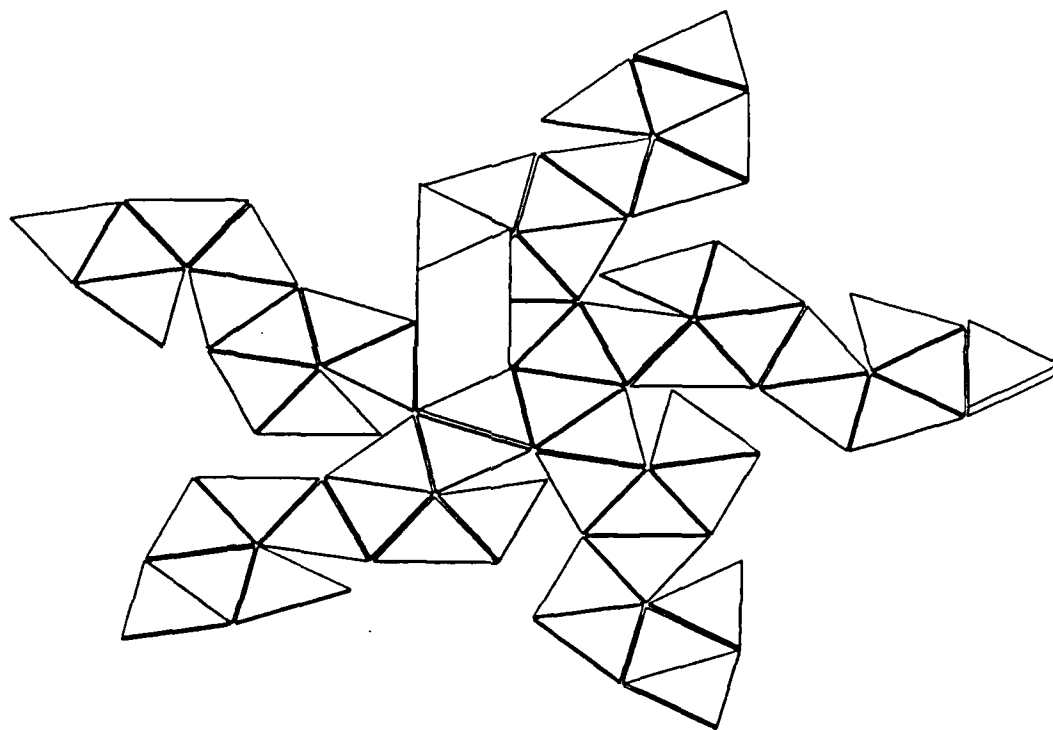
Fig. 6.2   3-D projection of the normal intensity component
over a sphere for a single piston centered on surface
element number 1 as reconstructed from a planar hologram.
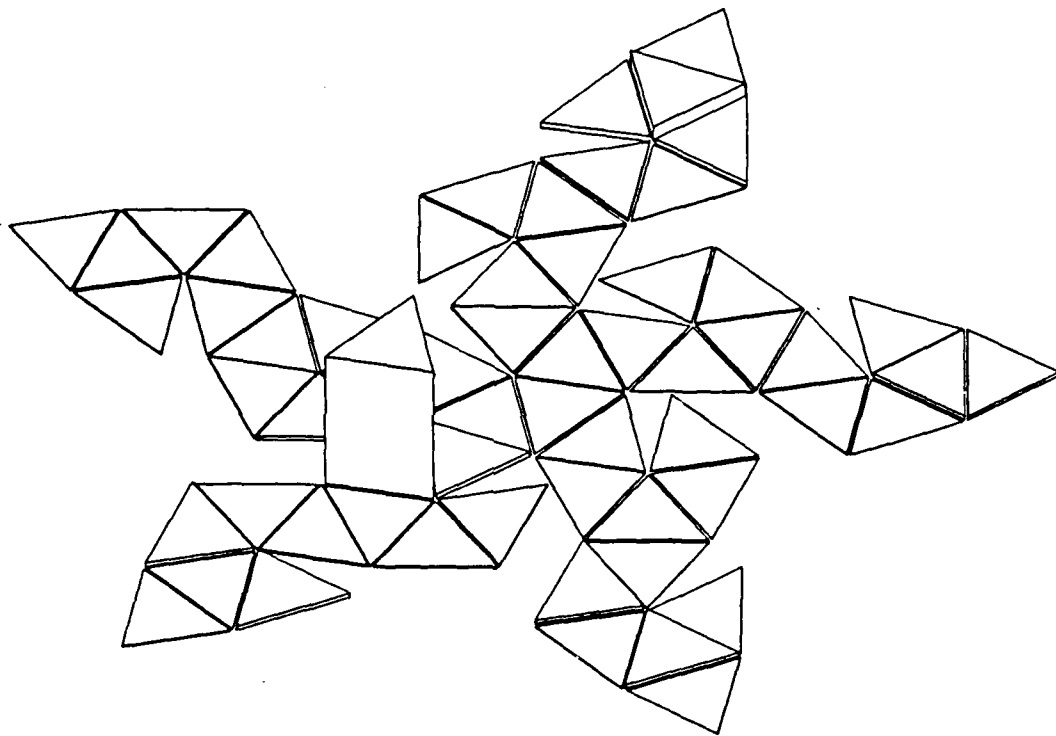
Fig. 6.3   The reconstructed normal component of intensity for a piston source centered on surface element 20.
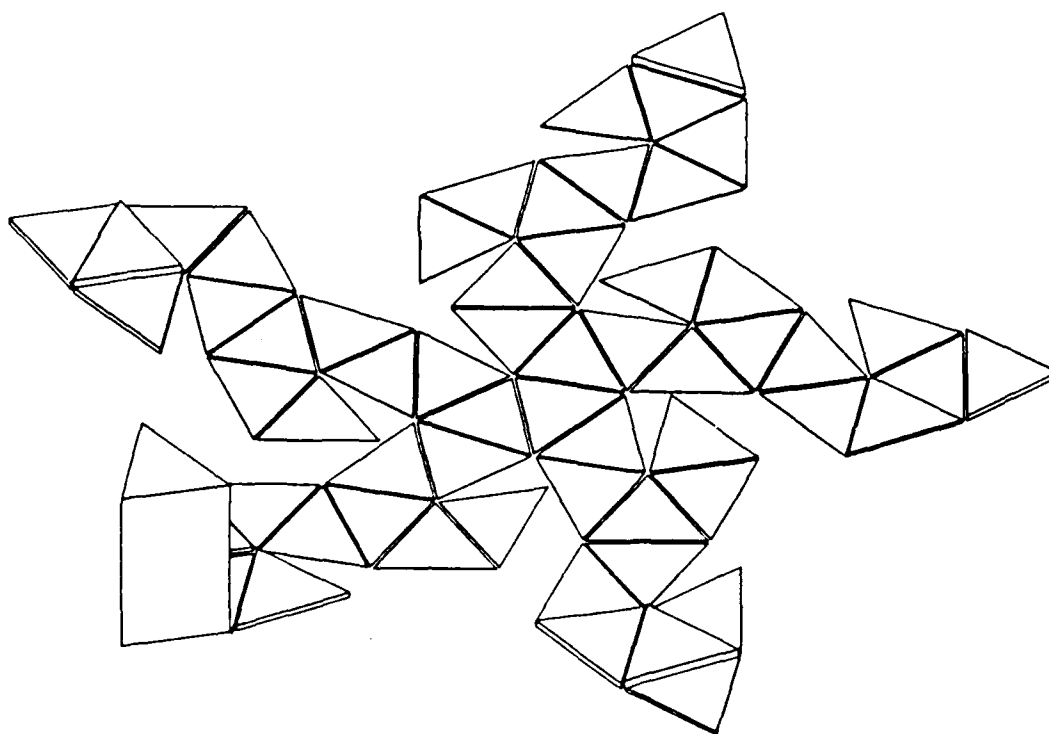
Fig. 6.4   The reconstructed normal component of intensity
for a piston source centered on surface element 56.
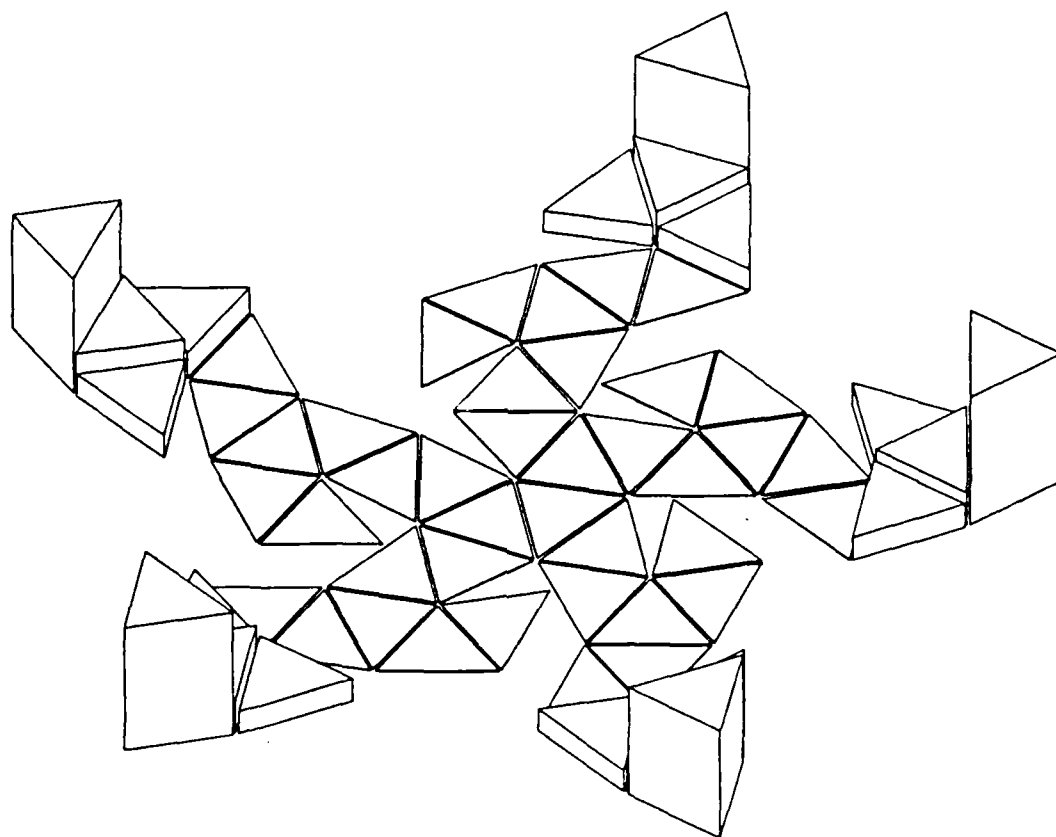
Fig. 6.5   The reconstructed normal component of intensity
for a piston source which faces directly away from the
hologram plane.

To see what happens when an actual source is poorly fit by the surface model, a reconstruction of a piston source which faces directly away from the hologram plane is presented in figure 6.5. The orientation of the theoretical piston is such that it is centered on a vertex of the five bottom-most elements and not on any single element. The reconstructed source strength at each of these five elements is approximately 20% that of the theoretical value at the source's center. Again the location of the source is clear, and it is reasonable to claim that only with a more complex surface approximation could any more detail about the source be obtained.

The sample reconstructions presented demonstrate the resolution possible in reconstructing a high aspect ratio object, the sphere, from measurements over a planar array. An actual physical experiment using these techniques, and with more sophisticated surface approximation elements,[52] is planned in the work of another graduate student.[53]

D.3 Reconstruction from a conforming hologram surface

The reconstructions from a planar hologram presented above required a large number of field measurements to achieve their resolution. Similar resolution can be achieved with far fewer field measurement points if all the points

fall on a surface which is nearby and surrounds the odd-shaped surface. As an example of this, the surface field of the small piston in a sphere is presented as reconstructed from 60 field measurements taken over a concentric sphere 0.23λ away.

Figure 6.6 displays the reconstructed amplitude of the normal component of surface velocity for a piston source centered on element 1. All sixty modes of the decomposition were used in this reconstruction and those presented below; these solutions can be considered free of any subjective filtering. The reconstructed maximum source velocity is 80% of the theoretical value. The noise in this display could be decreased by filtering out those modes corresponding to the smallest singular value, but it was retained to illustrate that this noise is not carried through the pressure field reconstruction process.

The amplitude of the reconstructed surface pressure field is displayed in figure 6.7a. This surface field was calculated from the velocity field displayed in figure 6.6 and the surface solution matrix. The amplitude of the theoretical field is shown in figure 6.7b below the experimental field. Both plots have the same scale and the agreement between the two is quite clear. The apparently good agreement between these two plots suggests that the surface velocity field of figure 6.6 differs from the

theoretical field mostly by a contribution

from noisy but non-radiating modes.

The reconstructed normal component of itensity for this source is displayed in figure 6.8. This plot clearly shows the existence of a small localized source and so illustrates the accurate reconstruction of phase information as well as amplitude information.

Fig. 6.6   The reconstructed amplitude of the normal
component of surface velocity for a piston source centered
on element 1 from a conforming hologram.
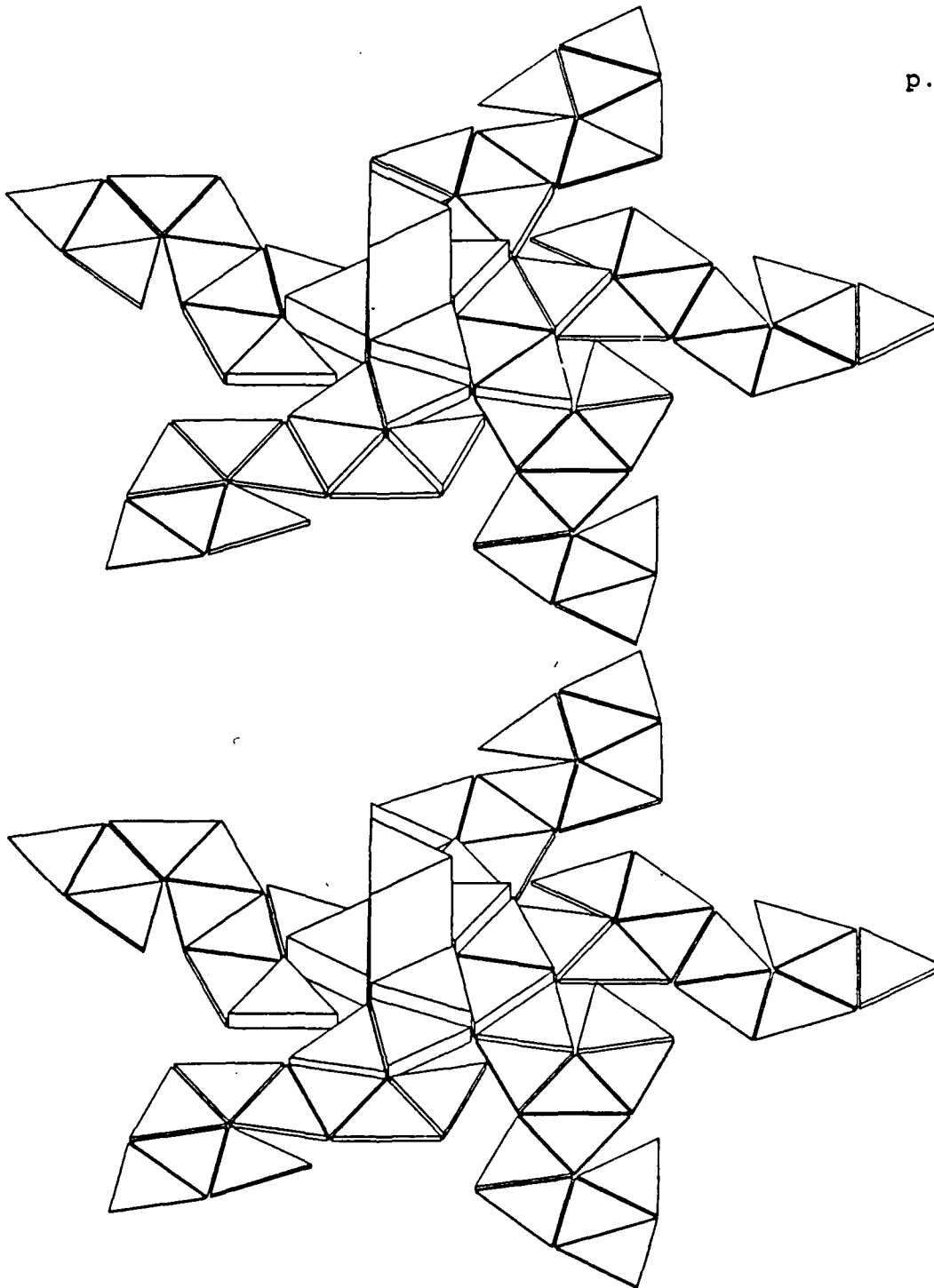
Fig. 6.7   a) The reconstructed amplitude of the surface
pressure for a piston source centered on element 1 from a
conforming hologram; b) theoretical amplitude.
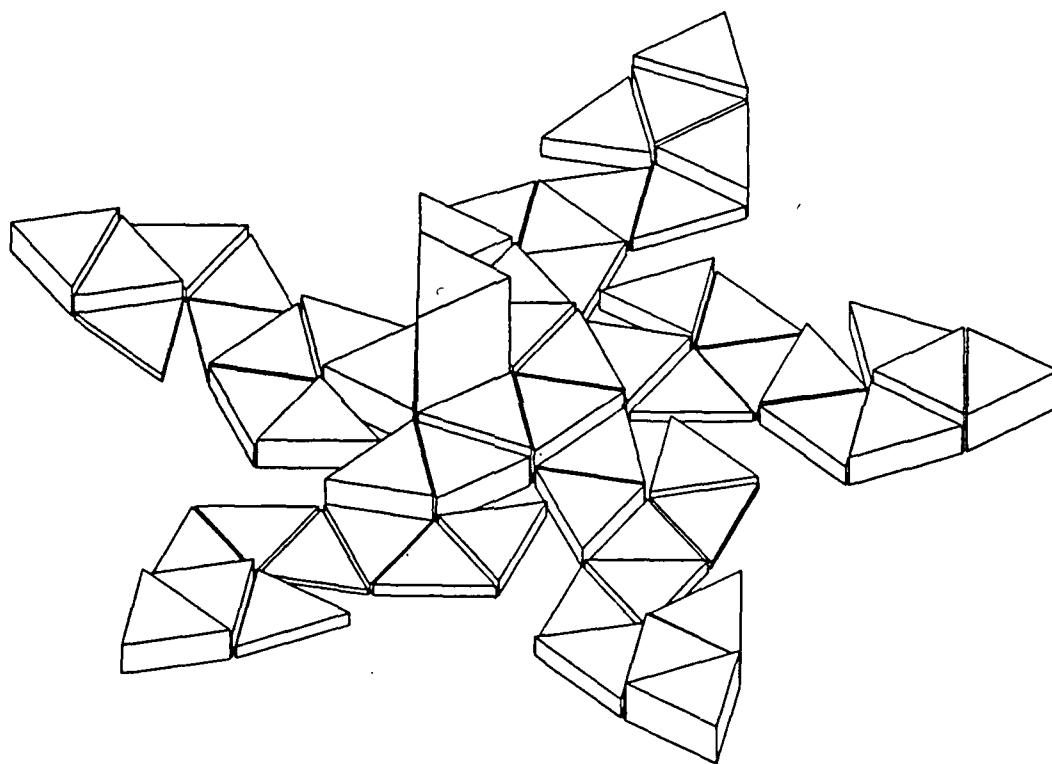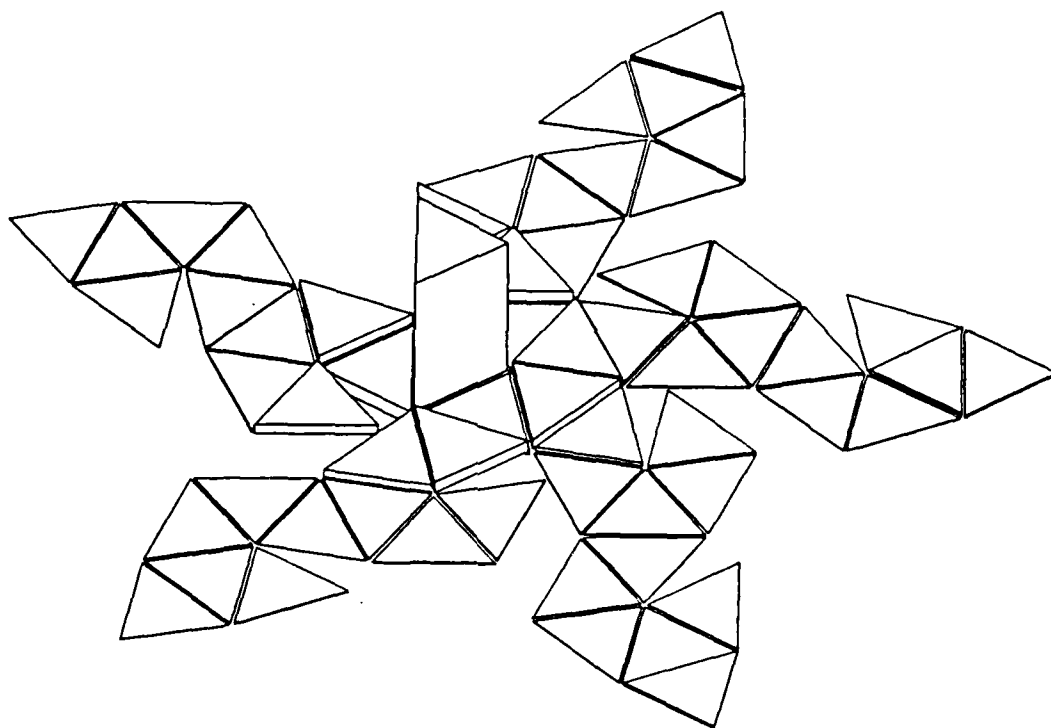
Fig. 6.8   The reconstructed normal component of intensity
for a piston source centered on element 1 from a conforming
hologram.

References

1. E.G. Williams and J.D. Maynard, Phys. Rev. Lett. <u>45</u>, 554 (1980).

2. J.D. Maynard and E.G. Williams, <u>Proceedings NOISE-CON 81</u>, edited by L.H. Royster, F.D. Hart, and N.D. Stewart (Noise Control Foundation, New York, 1981), pp. 19-24.

3. <u>The New Merriam-Webster Pocket Dictionary</u>, G.&C. Merriam Co.,1970(pub. Pocket Books, New York, 1970).

4. D. Gabor,Proc. Roy. Soc. A.,<u>197</u>, 454 (1949).

5. J.W. Goodman,"Holography", <u>Encyclopedia of Science and Technology</u>(McGraw-Hill,Inc.,New York,1982),Vol.6,p.635.

6. E. Hecht and A. Zajac, <u>Optics</u>,(Addison-Wesley Pub. Co., Reading, Mass., 1974), p. 501.

7. B.B. Brenden, <u>Optical and Acoustical Holography</u>, Proceedings of the NATO Advanced Study Institue on Optical and Acoustical Holography, edited by E. Camatini (Plenum Press, New York-London,1972),pp. 347-402.

8. For a discussion of subwavelength resolution in optical holography and a discussion of evanescent waves see, H.G. Schmidt-Weinmar, <u>Inverse Source Problems in Optics</u>, <u>Topics in Current Physics</u>, edited by H.P. Baltes(Springer Verlag, Berlin, 1978) Vol.9, p.83-118.

9. J.D. Maynard, E. G. Williams and Y. Lee,J. Acoust. Soc. Am. <u>78</u>, 1395 (1985).

10. A.V. Oppenheim and R.W. Schafer, <u>Digital Signal Processing</u> (Prentice-Hall,Inc. Englewood Cliffs,New Jersey, 1975),p.29.

11. T. Mizutani,"Experimental Analysis of a Hi-Fi Loud-speaker Using Near Field Acoustical Holography,"M.S. thesis,The Pennsylvania State University (1983) p.14-18.

12. W.Y. Strong Jr.,"Experimental Method to Measure Low Frequency Sound Radiation - Nearfield Acoustical Holography,"M.S. thesis, The Pennsylvania State University (1982) p.26-32.

13. D.J. Bowen and J.D. Maynard, J. Acoust. Soc. Am. Suppl. 1 75,S71 (1984).

14. M.L. Meade, Lockin Amplifiers, Principles and Applications, IEE Electrical Measurement Series 1 (Peter Perigrinus, London, 1983).

15. Scanning NAH systems have been developed by W. Strong at Steinway Pianos, CBS Technology Center, by T. Mitzutani at Technics Division of Matsushita, and by E.G. Williams at the Naval Research Lab.

16. Another scanning system, developed independently is described by, G. Weinrich and E.B. Arnold, J. Acous. Soc. Am. 68, 404-411 (1980).

17. T.B. Beyer,"Test of the Nearfield Acoustical Holography Technique Using an Unbaffled, Uniformly Oscillating Disk," M.S. thesis, The Pennsylvania State University (1984) pp.12-42.

18. J.D. Maynard, J. Acoust. Soc. Am. Suppl. 1, 76 S86 (1985).

19. Two-microphone intensity measuring techniques are discussed, for example, in F.J. Fahy, J. Acoust. Soc. Am. 62, 1057-1059 (1977) and G. Pavic, J. Sound Vib. 51, 535-545 (1977).

20. A four-microphone intensity probe is discussed in G.W. Elko,"Frequency Domain Estimation of the complex Acoustic Intensity and Energy Density," Ph.D. thesis, The Pennsylvania State University (1984).

21. W.Y. Strong, T.B. Beyer, D.J. Bowen, E.G. Williams, and J.D. Maynard, Journal of Guitar Acoustics, 6 50-59 (1982).

22. Anderson localization in a one-dimensional acoustic system is described in C.H. Hodges and J. Woodhouse, J. Acoust. Soc. Am. 74, 894-905 (1983).

23. Private communication, J.D. Maynard

24. E.G. Williams, H.D. Dardy, and R.G. Fink,"A technique for measurement of structure-borne intensity in plates," submitted to J. Acoust. Soc. Am.

25. A.L. Fetter and J.D. Walecka, Theoretical Mechanics of Particles and Continua (Mc Graw-Hill, New York, 1980), p.305.

26. F.W. Byron Jr. and R.W. Fuller, Mathematics of Classical and Quantum Physics (Addison-Wesley Pub. Co.,Reading, Mass. 1970), Vol. II, p.388.

27. J.D. Jackson, Classical Electrodynamics, Second Edition (John Wiley & Sons, New York, 1975), p.40.

28. M.C. Junger and D. Feit, Sound, Structures, and their Interaction, (MIT Press, Cambridge, 1972).

29. B.B. Baker and E.T. Copson, The Mathematical Theory of Huygens' Principle, Second Edition (The Claredon Press, Oxford, 1950),p.24.

30. H.A. Schenck, J. Acous. Soc. Am.,44,41 (1968).

31. Lord Rayleigh, Philos. Mag. $\underline{43}$, 259 (1897).

32. E.O. Brigham, The Fast Fourier Transform
    (Prentice-Hall, Engelwood Cliffs, NJ, 1974).

33. J.W. Goodman, Introduction to Fourier Optics,
    (McGraw-Hill, New York, 1968). p. 10.

34. I.S. Gradshteyn and I. M. Ryzhik, Table of Integrals,
    Series, and Products, (Academic press, 1980) p.736.

35. E. G. Williams and J. D. Maynard, J. Acoust. Soc. Am.
    $\underline{72}$, 2020 (1982).

36. J. A. Archer-Hall, A. I. Bashter and A. J. Hazelwood,
    J. Acoust. Soc. Am. $\underline{65}$, 1568 (1979).

37. D.G. Luenberger, Optimization by Vector Space Methods
    (John Wiley & Sons, New York, 1969), pp.294-297.

38. G.H. Golub and C.F. Van Loan, Matrix Computations (The
    John Hopkins University Press, 1983), p.370.

39. F. Ursell, Proc. Camb. Phil. Soc., $\underline{74}$, 117 (1973).

40. G.H. Koopmann and H Benner, J. Acoust. Soc. Am., $\underline{71}$, 78
    (1982).

41. H. Anton, Elementary Linear Algebra, Third Edition
    (John Wiley & Sons, New York, 1981), p.162.

42. G.W. Stewart, Introduction to Matrix Computations,
    (Academic Press, New York, 1973), p.318.

43. J.J. Dongarra, J.R. Bunch, C.B. Moler, and G.W.
    Stewart, LINPACK User's Guide (SIAM, Philadelphia,
    1979), pp.11.1-11.23.

44. reference 42, p.325.

45. coordinates of the polyhedron's vertices are given in
     J.C. Bohlen, Information Report VP-X-121 (Department
     of the Environment, Canadian Forestry Service, Western
     Forests Products Laboratory, Vancouver, British
     Columbia, 1974).

46. P.M. Morse and H. Feshbach, Methods of Theoretical
     Physics, (McGraw-Hill, New York, 1978) Vol. II,
     p.1465.

47. zeroes of the spherical Bessel functions are given in
     M. Abramowitz and I.A. Stegun, Handbook of Mathematical
     Functions (Dover Publications, New York, 1972), p.467.

48. R.S. Grosson, J. Geoph. Res., 81(17),3036-3046 (1976).

49. J.M. Varah, SIAM J. Numer. Anal., 10(2),257-267 (1973).

50. P.M. Morse and K.U. Ingard, Theoertical Acoustics,
     (McGraw-Hill, New York, 1968), pp.338-343.

51. P. Loutrel,"A Solution to the Hidden-Line Problem for
     Computer Drawn Polyhedra," Ph.D. thesis, New York
     University (1967).

52. A.F. Seybert, B. Soenarko, F.J. Rizzo, and D.J. Shippy,
     J. Acoust. Soc. Am., 77, 362-368 (1985)

53. Y. Huang, private communication

54. O.C. Zienkiewicz, The Finite Element Method
     [McGraw-Hill Book Co. (UK) Limited, London, 1982],p.767

Appendix A.

Discrete Convolution with the DFT

Discrete convolutions such as equation (3.6) of chapter III, can be performed exactly and quickly with the aid of the FFT to perform DFT operations.

To introduce the DFT and IDFT into equation (3.6), equation (3.6) is rewritten with the aid of the Kronecker Delta function,

$$\delta_{mn} = \begin{cases} 1; & m = n \\ 0; & m \neq n \end{cases} .$$

The result is

$$\Psi(p,q,z) = \sum_{l=0}^{N-1} \sum_{m=0}^{N-1} \sum_{r=-N}^{N-1} \sum_{s=-N}^{N-1} \Psi_{D,N}(l,m) \bar{G}_{D,N}(r,s,z) \delta_{r,p-l} \delta_{s,q-m}$$

$$(A.1).$$

The Delta function can be written in terms of the Fourier coefficients as

$$\delta_{mn} = \frac{1}{M} \sum_{\mu=0}^{M-1} e^{-i\frac{\pi}{N}\mu(m-n)} \quad \text{where } M=2N.$$

Substituting this expansion for the Delta functions in equation (A.1) and rearranging the summations leaves

$$\Psi(p,q,z) =$$

$$\frac{1}{M^2} \sum_{\mu=0}^{M-1} \sum_{\nu=0}^{M-1} e^{-i\frac{\pi}{N}(\mu p + \nu q)} \left[\sum_{l=0}^{N-1} \sum_{m=0}^{N-1} \Psi_{D,N}(l,m) e^{-i\frac{\pi}{N}(l\mu + m\nu)} \right] \times$$

$$\left[\sum_{r=-N}^{N-1} \sum_{s=-N}^{N-1} \bar{G}_{D,N}(r,s,z) e^{-i\frac{\pi}{N}(r\mu + s\nu)} \right]$$

$$(A.2).$$

Using the functions $\Psi'_{D,N}$ and $\bar{G}'_{D,N}$ as defined in equations

(3.7) and (3.12), the bracketed double sums in (A2) can be rewritten as DFT's. By making use of the identity $exp[i\pi r\mu/N] = exp[i\pi(r-2N)\mu/N]$ to arrange the second bracketed sum, equation (A2) becomes

$$\Psi(p,q,z)=$$
$$\frac{1}{M^2} \sum_{\mu=0}^{M-1} \sum_{\nu=0}^{M-1} e^{-i\frac{\pi}{N}(\mu p+\nu q)} \left[\sum_{l=0}^{M-1} \sum_{m=0}^{M-1} \Psi'_{D,N}(l,m) e^{-i\frac{\pi}{N}(l\mu+m\nu)} \right] X$$
$$\left[\sum_{r=0}^{M-1} \sum_{s=0}^{M-1} \bar{G}'_{D,N}(r,s,z) e^{-i\frac{\pi}{N}(r\mu+s\nu)} \right]$$

$$(A.3).$$

The summations in equation (A3) can now be replaced by the DFT and IDFT operations as defined in equations (3.8) and (3.9). The final form with these substitutions is given by equations (3.10) and (3.11).

Appendix B.

Quadratic expansion and Integration of the Green's Functions

Real-space Green's functions

Rectangular Elements

Integrations, over rectangular patches, of the real space Green's function are approximated by a truncated Taylor series expansion of the function about each patch's center (x_0, y_0):

$G(x_0 + x, y_0 + y, z - z_0) \approx f(x,y)$, with $z - z_0$ constant, where

$$f(x,y) = \alpha_0 + \alpha_1 x + \alpha_2 y + \alpha_3 xy + \alpha_4 x^2 + \alpha_5 y^2 + \alpha_6 x^2 y + \alpha_7 xy^2 + \alpha_8 x^2 y^2$$

and where the α_i are given below.

Integration of this form over the patch yields

$$\int_{-\frac{\Delta x}{2}}^{\frac{\Delta x}{2}} \int_{-\frac{\Delta y}{2}}^{\frac{\Delta y}{2}} f(x,y) \, dx \, dy$$

$$= \alpha_0 \Delta x \Delta y + \alpha_4 \frac{(\Delta x)^3 \Delta y}{12} + \alpha_5 \frac{\Delta x (\Delta y)^3}{12} + \alpha_8 \frac{(\Delta x)^2 (\Delta y)^2}{144} \quad (B.1).$$

Along the z-axis $x_0 = y_0 = 0$, a different approach is used: The exact integral over a circular region of radius r around the axis is performed, and the integration over the remaining region, to complete a square, is approximated by

expanding about the square's corner. In terms of the
expansion coefficients, α_i, a single corner integration
yields

$$\int_0^r \int_0^r \frac{f(x',y')}{(r^2-x'^2)^{1/2}} \, dx'dy' =$$
$$\alpha_0 \beta_0 r^2 + (\alpha_1+\alpha_2)\beta_1 r^3 + \alpha_3\beta_3 r^4 + (\alpha_4+\alpha_5)\beta_4 r^4 + (\alpha_6+\alpha_7)\beta_6 r^5 + \alpha_3\beta_8 r^6$$

$$(B.2)$$

where x,y, are from the center of the square, while x',y'
are from one of its corners. The coefficients β_i are:

$$\beta_0 = 2.1460184 \times 10^{-1}$$

$$\beta_1 = 4.793517 \times 10^{-2}$$

$$\beta_3 = 6.2685032 \times 10^{-3}$$

$$\beta_4 = 1.8252296 \times 10^{-2}$$

$$\beta_6 = 1.5856291 \times 10^{-3}$$

$$\beta_8 = 2.889426 \times 10^{-4} \qquad .$$

The exact integration over the central circular region for
Neumann boundary conditions is

$$\int_0^{2\pi} \int_0^r G_N(r',z) \, r'dr'd\theta = \rho c \left[e^{ikz} - e^{ik(r^2+z^2)^{1/2}} \right] \qquad (B.3),$$

and for Dirichlet boundary conditions it is

$$\int_0^{2\pi} \int_0^r G_D(r',z) \, r'dr'd\theta = \left[e^{ikz} - \frac{ze^{ik(r^2+z^2)^{1/2}}}{(r^2+z^2)^{1/2}} \right] \qquad (B.4).$$

To calculate $g_{D,N}^{(2)}(z)$ or $g_{D,N}^{(4)}(z)$ from equation (3.11),

$\bar{G}_{D,N}^{!}(l,m,z)$ is approximated by a polynomial expansion as

given in equation (B.1) except when the point (x=0,y=0) is

included in the integration patch indicated by l and m.

Appropriate values for x_0 and y_0 are given by x_l and y_m of

equation (3.3) and (3.4) for $g_{D,N}^{(2)}(z)$, and by $x_l^{!} = x_l + \Delta/2$

and $y_l^{!} = y_l + \Delta/2$ for $g_{D,N}^{(4)}(z)$.

The point (x=0,y=0) is centered in the integration

patch of $\bar{G}_{D,N}(l=0,m=0,z)$ for $g_{D,N}^{(2)}(z)$. In this case, the

approximation for $\bar{G}_{D,N}(l=0,m=0,z)$ is the sum of the

appropriate integral from equations (B.3) and (B.4) with

$r=\Delta/2$ plus four times (once for each corner of the patch)

equation (B.2), with $r=\Delta/2$ and with $x_0 = y_0 = \Delta/2$ [to determine

the coefficients $\alpha_i(x_0,y_0)$].

When calculating $g_{D,N}^{(4)}(z)$ based on equation (3.11) and

the shifted sampling coordinates $x_l^{!}$ and $y_m^{!}$, the four

integrations, which yield $\bar{G}_{D,N}(l,m,z)$ for $(l,m) = (0,0)$,

$(-1,0),(0,-1),(-1,-1)$, have the point (x=0,y=0) at one

corner of their integration patches. $\bar{G}_{D,N}(l,m,z)$ for each

of these four index pairs is given by one-fourth the

appropriate integral from equations (B.3) and (B.4) Plus the

corner integration, equation (B.2), with $r=\Delta$ and with $x_0=y_0=\Delta$.

The form $g_{D,N}^{(1)}(z)$ is calculated from equation (3.13) as described except when $l = m = 0$. For $l = m = 0$, the appropriate integral, Dirichlet or Neumann, from equations (B.2) and (B.4) is used with $r= (\Delta^2/\pi)^{1/2}$.

The Expansion Polynomial Coefficients $\alpha_i(x_0, y_0)$, where

$a = kR_0$, $b = kx_0$, $d = ky_0$, $k = \omega/c$, and $R_0^2 = x_0^2 + y_0^2 + z^2$

are for Neumann Boundary conditions (normal velocity to pressure):

$$\alpha_0 = -i\frac{\rho c k^2}{2\pi}\frac{e^{ia}}{a}$$

$$\alpha_1 = -i\frac{\rho c k^3}{2\pi}b(ia^{-2}-a^{-3})e^{ia}$$

$$\alpha_2 = -i\frac{\rho c k^3}{2\pi}d(ia^{-2}-a^{-3})e^{ia}$$

$$\alpha_3 = -i\frac{\rho c k^4}{2\pi}bd(-a^{-3}-3ia^{-4}+3a^{-5})e^{ia}$$

$$\alpha_4 = -i\frac{\rho c k^4}{4\pi}[ia^{-2}-a^{-3}+b^2(-a^{-3}-3ia^{-4}+3a^{-5})]e^{ia}$$

$$\alpha_5 = -i\frac{\rho c k^4}{4\pi}[ia^{-2}-a^{-3}+d^2(-a^{-3}-3ia^{-4}+3a^{-5})]e^{ia}$$

$$\alpha_6 = -i\frac{\rho c k^5}{4\pi}d[-a^{-3}-3ia^{-4}+3a^{-5}+b^2(-ia^{-4}+6a^{-5}+15ia^{-6}-15a^{-7})]e^{ia}$$

$$\alpha_7 = -i\frac{\rho c k^5}{4\pi}b[-a^{-3}-3ia^{-4}+3a^{-5}+d^2(-ia^{-4}+6a^{-5}+15ia^{-6}-15a^{-7})]e^{ia}$$

$$\begin{aligned}
\alpha_8 = -i\frac{\rho c k^6}{8\pi}[&(-a^{-3}-3ia^{-4}+3a^{-5})\\
&+(b^2+d^2)(-ia^{-4}+6a^{-5}+15ia^{-6}-15a^{-7})\\
&+b^2d^2(a^{-5}+10ia^{-6}-45a^{-7}-105ia^{-3}+105a^{-3})]e^{ia} \;;
\end{aligned}$$

and for Dirichlet boundary conditions (pressure to pressure):

$$\alpha_0 = \frac{k^3 z}{2\pi}(a^{-3} - ia^{-2})e^{ia}$$

$$\alpha_1 = \frac{k^4 z}{2\pi}b(a^{-3} + 3ia^{-4} - 3a^{-5})e^{ia}$$

$$\alpha_2 = \frac{k^4 z}{2\pi}d(a^{-3} + 3ia^{-4} - 3a^{-5})e^{ia}$$

$$\alpha_3 = \frac{k^5 z}{2\pi}bd(ia^{-4} - 6a^{-5} - 15ia^{-6} + 15a^{-7})e^{ia}$$

$$\alpha_4 = \frac{k^5 z}{4\pi}[(a^{-3} + 3ia^{-4} - 3a^{-5}) + b^2(ia^{-4} - 6a^{-5} - 15ia^{-6} + 15a^{-7})]e^{ia}$$

$$\alpha_5 = \frac{k^5 z}{4\pi}[(a^{-3} + 3ia^{-4} - 3a^{-5}) + d^2(ia^{-4} - 6a^{-5} - 15ia^{-6} + 15a^{-7})]e^{ia}$$

$$\alpha_6 = \frac{k^6 z}{4\pi}[d(ia^{-4} - 6a^{-5} - 15ia^{-6} + 15a^{-7}) + b^2 d(-a^{-5} - 10ia^{-6} + 45a^{-7} + 105ia^{-8} - 105a^{-9})]e^{ia}$$

$$\alpha_7 = \frac{k^6 z}{4\pi}[b(ia^{-4} - 6a^{-5} - 15ia^{-6} + 15a^{-7}) + bd^2(-a^{-5} - 10ia^{-6} + 45a^{-7} + 105ia^{-8} - 105a^{-9})]e^{ia}$$

$$\alpha_8 = \frac{k^7 z}{8\pi}[(i\ a^{-4} - 6a^{-5} - 15ia^{-6} + 15a^{-7}) + 2bd(-a^{-5} - 10ia^{-6} + 45a^{-7} + 105ia^{-8} - 105a^{-9}) + b^2 d^2(-ia^{-6} + 15a^{-7} + 105ia^{-8} - 420a^{-9} - 945ia^{-10} + 945a^{-11}]e^{ia}$$

Triangular elements

Integrations of the Green's functions are done in the same manner as is done for rectangular elements, although only the first six expansion terms are considered. In the

local coordinate system of each triangle, the vertices have coordinates (x_1, y_1), (x_2, y_2), and (x_3, y_3). The result of integrating the Taylor series expansion, in terms of the local vertex coordinates and total triangle area Δ,[54] is

$$\int_\Delta f(x', y') \, dx'dy' =$$
$$\alpha_0 \Delta + \alpha_3 \frac{\Delta}{12}(x_1 y_1 + x_2 y_2 + x_3 y_3) + \alpha_4 \frac{\Delta}{12}(x_1^2 + x_2^2 + x_3^2) + \alpha_5 \frac{\Delta}{12}(y_1^2 + y_2^2 + y_3^2) \ .$$

When calculating the diagonal monopole coefficient, equation (B.3) is evaluated with $r = (\Delta/\pi)^{1/2}$, and no expansion terms are considered.

Integrated k-space Green's functions

The integrated k-space Green's functions are obtained by performing an integration averaging of the analytic Green's function in the area between k_{r_1} and k_{r_2} where $k_{r_1} = (k_x^2 + k_y^2)^{1/2} - \Delta k_r$ and $k_{r_2} = (k_x^2 + k_y^2)^{1/2} + \Delta k_r$. In this study, $\Delta k_r = \sqrt{2} \Delta k_x$ is used. The resulting integrated averages for Neumann boundary conditions are:

Radiation region

$$g_N^{(6)}(k_x, k_y, z) = - \frac{2i\rho ckz(e^{ik_1 z} - e^{ik_2 z})}{(k_1^2 z^2 - k_2^2 z^2)} \quad ; \quad \begin{array}{l} k_1^2 = k^2 - k_{r_1}^2 \\ k_2^2 = k^2 - k_{r_2}^2 \end{array}$$

$$= \frac{2\rho ck}{(k_1 + k_2)} \quad \text{when } z=0$$

Mixed evanescent and propagating region

$$g_N^{(6)}(k_x, k_y, z) = - \frac{2i\rho ckz(e^{ik_1 z} - e^{-k_2 z})}{(k_1^2 z^2 + k_2^2 z^2)} \quad ; \quad \begin{array}{l} k_1^2 = k^2 - k_{r_1}^2 \\ k_2^2 = k_{r_2}^2 - k^2 \end{array}$$

$$= \frac{2\rho ck(k_1 - ik_2)}{(k_1^2 + k_2^2)} \quad \text{when } z=0$$

Evanescent region

$$g_N^{(6)}(k_x, k_y, z) = + \frac{2i\rho ckz(e^{-k_1 z} - e^{-k_2 z})}{(k_1^2 z^2 - k_2^2 z^2)} \quad ; \quad \begin{array}{l} k_1^2 = k_{r_1}^2 - k^2 \\ k_2^2 = k_{r_2}^2 - k^2 \end{array}$$

$$= \frac{-2i\rho ck}{(k_1 + k_2)} \quad \text{when } z=0$$

The resulting integrated averages for Dirichlet boundary conditions are:

Radiation region

$$g_0^{(6)}(k_x, k_y, z) = 2\frac{[(1-ik_1 z)e^{ik_1 z} - (1-ik_2 z)e^{ik_2 z}]}{(k_1^2 z^2 - k_2^2 z^2)} \quad ; \quad \begin{array}{l} k_1^2 = k^2 - k_{r1}^2 \\ k_2^2 = k^2 - k_{r2}^2 \end{array}$$

Mixed evanescent and propagating region

$$g_0^{(6)}(k_x, k_y, z) = 2\frac{[(1-ik_1 z)e^{ik_1 z} - (1+k_2 z)e^{-k_2 z}]}{(k_1^2 z^2 + k_2^2 z^2)} \quad ; \quad \begin{array}{l} k_1^2 = k^2 - k_{r1}^2 \\ k_2^2 = k_{r2}^2 - k^2 \end{array}$$

Evanscent region

$$g_0^{(6)}(k_x, k_y, z) = -2\frac{[(1+k_1 z)e^{-k_1 z} - (1+k_2 z)e^{-k_2 z}]}{(k_1^2 z^2 - k_2^2 z^2)} \quad ; \quad \begin{array}{l} k_1^2 = k_{r1}^2 - k^2 \\ k_2^2 = k_{r2}^2 - k^2 \end{array}$$

Appendix C.

DFT Error in Approximating the Continuous Fourier Transform

The 2-D Fourier transform of a function $f(x,y)$ is given explicitly by

$$\tilde{F}(k_x,k_y) = \int_{-\infty}^{+\infty}\int_{-\infty}^{+\infty} f(x,y)e^{-i(k_x x + k_y y)}dxdy \qquad (C.1).$$

It is assumed that the function $f(x,y)$ is reasonably smooth and is known at a sufficiently large number of points (x_r,y_s) so that one can write $f(x,y) = f(x_r,y_s)$ if $|x-x_r| \leqq \Delta/2$ and $|y-y_s| \leqq \Delta/2$ where $x_r = r\Delta$ and $y_s = s\Delta$ for $r,s = 0,\pm1,\pm2,\ldots$

Equation (C.1) can then be written:

$$\tilde{\Psi}(k_x,k_y) = \sum_r \sum_s f(x_r,y_s)\int_{x_r-\Delta/2}^{x_r+\Delta/2}\int_{y_s-\Delta/2}^{y_s+\Delta/2} e^{-i(k_x x + k_y y)}dxdy \quad (C.2).$$

The integral in equation (C.2) is readily evaluated yielding:

$$\tilde{F}(k_x,k_y) = \sum_r \sum_s f(x_r,y_s)e^{-i(k_x x_r + k_y y_s)}\left[\frac{4\,\sin(k_x\Delta/2)\,\sin(k_y\Delta/2)}{k_x\,k_y}\right] \quad (C.3).$$

The discrete Fourier Transform of $f(x_r,y_s)$ can be written explicitly as:

$$\tilde{F}'(k_x,k_y) = \Delta^2\sum_r \sum_s f(x_r,y_s)e^{-i(k_x x_r + k_y y_s)} \qquad (C.4).$$

By dividing equation (C.4) by equation (C.3), an estimate is obtained for the error in approximating the continuous

Fourier transform of an approximately piecewise constant function $f(x,y)$ by the Discrete Fourier transform. The result is:

$$\frac{\tilde{F}'(k_x,k_y)}{\tilde{F}(k_x,k_y)} = \left[\frac{k_x\Delta \ k_y\Delta}{4 \ \sin(k_x\Delta/2) \ \sin(k_y\Delta/2)}\right] \qquad (C.5).$$

Unclassified
SECURITY CLASSIFICATION OF THIS PAGE (When Data Entered)

REPORT DOCUMENTATION PAGE	READ INSTRUCTIONS BEFORE COMPLETING FORM

1. REPORT NUMBER	2. GOVT ACCESSION NO.	3. RECIPIENT'S CATALOG NUMBER
	AD-A168064	

4. TITLE (and Subtitle)	5. TYPE OF REPORT & PERIOD COVERED
RESEARCH WITH NEARFIELD ACOUSTIC HOLOGRAPHY	Final Report 32 Aug. 01 - 35 Sept. 30
	6. PERFORMING ORG. REPORT NUMBER
	NA

7. AUTHOR(s)	8. CONTRACT OR GRANT NUMBER(s)
Julian D. Maynard	N00014-82-K-0610

9. PERFORMING ORGANIZATION NAME AND ADDRESS	10. PROGRAM ELEMENT, PROJECT, TASK AREA & WORK UNIT NUMBERS
The Pennsylvania State University University Park, PA 16802	61153N 11 NR384-937

11. CONTROLLING OFFICE NAME AND ADDRESS	12. REPORT DATE
Office of Naval Research Physics Division - Code 1112 Arlington, VA 22217	March 1986
	13. NUMBER OF PAGES
	16 + APPENDIX

14. MONITORING AGENCY NAME & ADDRESS(If different from Controlling Office)	15. SECURITY CLASS. (of this report)
	Unclassified
	15a. DECLASSIFICATION/DOWNGRADING SCHEDULE

16. DISTRIBUTION STATEMENT (of this Report)

Approved for public release; distribution unlimited.

17. DISTRIBUTION STATEMENT (of the abstract entered in Block 20, if different from Report)

18. SUPPLEMENTARY NOTES

19. KEY WORDS (Continue on reverse side if necessary and identify by block number)

final report, nearfield acoustic holography, sound measurement acoustic intensity

20. ABSTRACT (Continue on reverse side if necessary and identify by block number)

See reverse side

DD FORM 1473
1 JAN 73   EDITION OF 1 NOV 65 IS OBSOLETE
S/N 0102-014-6601

Unclassified
SECURITY CLASSIFICATION OF THIS PAGE (When Data Entered)

END

DTIC

7—86